Alma Mater Studiorum · Università di Bologna

FACOLTÀ DI SCIENZE MATEMATICHE, FISICHE E NATURALI
Corso di Laurea Magistrale in Fisica del Sistema Terra

Characterization of the co-seismic slip field for large earthquakes

Relatore:
Prof. Stefano Tinti

Correlatore:
Prof. Alberto Armigliato

Presentata da:
Enrico Baglione

Sessione autunnale
Anno Accademico 2015/2016

Abstract

Focused studies on large earthquakes have highlighted that ruptures on generating faults are strongly heterogeneous. The main aim of this thesis is to explore characteristic patterns of the slip distribution of large earthquakes, by using the finite-fault models (FFM) obtained in the last 25 years.

A result of this thesis is the computation of regression laws linking focal parameters with magnitude. Particular attention was devoted to the aspect ratio (A.R.), defined as the ratio between fault length and width. FFMs have been partitioned in 3 A.R. classes and for each class, the position of the hypocentre, of the maximum slip and their mutual relation were investigated.

To favour inter-comparison, normalised images of on-fault seismic slip were produced on geometries typical of each A.R. class with the goal of finding possible regularities of the slip distribution shapes. In this thesis, the shape of the single-asperity FFMs has been fitted by means of 2D Gaussian distributions. To the knowledge of the author, this thesis is the first example of a systematic study of finite-fault solutions to identify the main pattern of the on-fault co-seismic slip of large earthquakes.

One of the foreseen applications is related to tsunamigenesis. It is known that tsunamis are mainly determined by the vertical displacement of the seafloor induced by large submarine earthquakes. In this thesis, the near-source vertical-displacement fields produced by the FFM (assumed as the real one), by a homogeneous fault model, by a depth-heterogeneous fault model and by two distinct 2D Gaussian distribution fault models were computed and compared for all single-asperity earthquakes. The main finding is that 2D Gaussian distributions give the least misfit fields and are therefore the most adequate for tsunami generation modelling.

Table of contents

Introduction

Large earthquakes (i.e. earthquakes with significant values of magnitude, typically larger than 6) are known to have distribution of slip on the fault plane that is not homogeneous, though in several applications and contexts (for instance for modelling of earthquake-induced tsunamis) a uniform distribution is assumed as a reasonably good approximation. How the co-seismic slip distributes on the fault is the main topic of this thesis, and the data used for this study are mostly the finite-fault models (FFM) of the SRCMOD database that can be accessed online. These slip models were obtained by using different data sources (geodetic, strong motion, teleseismic, local P waves, inSAR, and, in the best cases, a combination of two or more of them), and different crustal models, and by different inversion techniques and stabilization methods, and different spatial sampling (Manighetti et al., 2005).

Regression laws between the geometrical properties of the fault and the magnitude are obtained and compared to some of the laws of previous studies and published in the literature. Among the studied parameters, the fault area and length result the ones showing the highest correlation with magnitude. The aspect ratio, that is the length to width ratio, has been also regressed against the earthquake magnitude, which is a novelty of this study never examined before: as will be described in detail later, we found that the aspect-ratio vs. magnitude correlation is good mainly for the strike-slip events. The aspect ratio has been used in the present work to create three classes of earthquakes or, which is equivalent in our context, of FFMs. The original FFM have been rescaled to the typical dimension of each class and the rescaled FFM have been analysed to investigate the position of the hypocentre with respect to the regions of significant slip (and of the maximum) slip. Thanks to the FFM representation, through a qualitative analysis, it is shown that the hypocentre rarely lies close to the fault centre or to the peak of slip, but that more often it is found at the margin of an asperity, that is a region of significantly high slip. This result agrees with that obtained by Mai et al. (2005), for whom hypocentres are located either within or close to regions of large slip. The number of asperities, furthermore, tend to increase with the increasing of the aspect ratio. For smaller magnitudes, the position of the slip peak is often close to the centre of the fault. Its distance from the fault centre tends to increase in parallel with the magnitude.

The generation of standardized images of the rescaled FFM allowed us to analyse the distribution of the slip and compare different models by means of properly introduced similarity indexes. The property of most FFM to exhibit a single and clear region of high slip (i.e. a single asperity) has suggested us to best-fit the slip model by means of a 2D Gaussian distribution. We have used two different methods (least-square and highest-similarity) for such fitting hence obtaining two distinct 2D Gaussian distributions for each FFM. Since the main interest of the line of research started with this thesis is the generation of tsunamis by earthquakes, we have calculated the vertical displacements induced by the earthquake at the Earth surface in the near field. We have computed such fields with the FFM slip (assumed to be the real one), with an equivalent uniform-slip model, with a depth-dependent slip model, and with the two "best" Gaussian slip models. Results show that using uniform slip sources one can get discrepancies in the surface fields larger than 50% on average, which is slightly reduced with depth-dependent sources. The best results are the ones obtained with 2D Gaussian distributions based on similarity index fitting.

The study of this thesis sets the basis for a following research project to be carried out by the author during the PhD work where the aim is to explore the feasibility of a real-time assessment of the co-seismic slip of large earthquakes having high tsunamigenic potential. And, among these, the shallow events with potential consequences in the near field will assume more importance, because the near field is known to be more susceptible to the heterogeneous distribution of the slip.

1.1 The on-fault slip distribution: an overview

The distribution of the slip over the fault has already been object of numerous studies, especially in the last decades, thanks to the source-inversion methods and the growth of the available amount of data.

Though it is out of the scope of this thesis to make a detailed, but painstaking, review of all the related literature, it is however worth mentioning some of the most relevant studies.

Beroza (1991), analysing data from the 1989 Loma Prieta earthquake, analyses the slip distribution by using a tomographic back-projection technique. He finds a correlation between areas of high slip and areas of low aftershock activity, explaining this by

stating areas of high slip are also areas of high strength, that rupture completely only during infrequent large mainshocks.

Mai and Beroza (2000) develop a stochastic characterization of earthquake slip complexity: they model the slip as a spatial random field, more precisely as a von Karman autocorrelation function (ACF) model, with parameters depending on the source dimension.

Milliner et al. (2016) find a spatial correlation between fluctuations of the slip distribution and geometrical fault structure. Studying the 1992 Landers and 1999 Hector Mine earthquakes, they discover that the spatial frequency content of the fault structure can be observed within the slip distribution, which is suggestive that rougher faults systems produce rougher co-seismic slip at all scales.

1.2 Source slip distribution and tsunami

Most tsunami models assume that the initial sea surface displacement is equal to the vertical displacement of the sea floor induced by the earthquake that is computed by means of standard analytical models based on Volterra's theory of elastic dislocations. Further common assumption is that the slip over the fault plane is uniform. However, modern teleseismic and geodetic inversion techniques have confirmed that the assumption of a uniform slip over the entire rupture plane is invalid.

The way the slip is distributed has direct influence on the possible generated tsunami. Many numerical simulations have highlighted that the same scenarios show very different results depending on whether one considers or not a uniform slip model.

An example of these investigations is the work by Geist (2002), who studied the effect of rupture complexity on the local tsunami wave field. Geist noticed that in the far-field tsunami amplitudes are well predicted only on the basis of the seismic moment, but that this is not true for local tsunami amplitudes. Looking at a global catalogue of tsunami runup observations, he noticed that discrepancy is larger for the most frequently occurring tsunamigenic earthquakes in the magnitude range of $7 < Mw < 8.5$, which is actually included in the range of interest for our study. Variability in local tsunami runup scaling can be ascribed to tsunami source parameters that are independent of seismic moment such as: variations in the sea depth in the source region, the combination of higher slip and lower shear modulus at shallow depth, and rupture

complexity in the form of heterogeneous slip distribution patterns. Geist showed that, for shallow subduction zone earthquakes, self-affine irregularities of the slip distribution result in significant variations in local tsunami amplitude and that the effects of rupture complexity are less pronounced for earthquakes at greater depth or along faults with steep dip angles.

The influence of fault parameters on the maximum runup has been, among others, pointed out by Løvholt et al. (2012). They analysed how heterogeneous coseismic slip affects the initial water surface elevation and consequently the tsunami runup on the coast for a high number of stochastic slip realizations. These different realizations result in a range of initial seabed responses. They explored the relevance on the simulated maximum runup of different parameters. Among them, the most important were shown to be the scaled seabed volume displaced per unit length and the maximum peak-to-peak vertical seabed displacement.

Relevance to this subject has also the abundant literature published on the two greatest and most destroying earthquakes of the last 25 years: i.e. the 26 December 2004 Sumatra–Andaman earthquake and the 11 March 2011 Tohoku earthquake.

The 2004 earthquake was the first event with $M_W > 9$ to be recorded by a global network of broadband seismic stations and regional GPS networks, and plays a role of historical importance in the field of tsunami hazard and forecasting. Geist et al. (2007) observed that empirical forecast relationships based only on seismic moment underestimate the mean regional tsunami heights at azimuths in line with the tsunami beaming pattern (e.g., Sri Lanka and Thailand), and that dislocation theory provides acceptable results as regards tsunami generation and propagation. In a previous study Geist et al. (2006) noticed that the March 2005 local tsunami, which occurred on a fault that was the southward continuation of the 2004 earthquake source, was deficient relative to its earthquake magnitude. The study highlighted that a significant factor affecting tsunami generation not considered in the scaling laws is the location of regions of seafloor displacement relative to the overlying sea depth. The deficiency of the March 2005 tsunami seems to be related to the concentration of slip in the down-dip part of the rupture zone that was underneath a region of shallow water and of land. Hence, the information on the distribution of slip over the fault plane, and,

consequently, the position of the region of high slip, is of great importance for the evaluation of local tsunami runup. Results from these studies indicate the difficulty in rapidly assessing local tsunami runup from magnitude and epicentre location information alone (Geist et al. 2006).

Sobolev et al. (2007) demonstrated that the presence of islands between the trench and the Sumatran coast makes earthquake-induced tsunamis especially sensitive to the slip distribution on the rupture plane. Indeed, wave heights in coastal towns such as Padang may differ by more than a factor of 5 for earthquakes having the same seismic moment (magnitude) and rupture zone geometry but different slip distribution. They concluded that, in presence of massive islands close to the trench, reliable prediction of tsunami wave heights cannot be provided by using traditional, earthquake-magnitude-based methods. This is also valid for the local tsunami in general, since the near-field tsunami height is controlled by the slip variability rather than by the seismic moment.

The other great and most studied case is the 11 March 2011, Tohoku, Japan, tsunamigenic earthquake.

Differently from the Sumatra's case, this earthquake presents a small rupture area compared to the magnitude of the event, while the estimated slip peak reached extremely high values (about 50 metres). Løhvolt et al. (2012) claimed that a heterogeneous source model is essential to simulate the observed distribution of the run-up correctly. Iinuma et al. (2012) confirmed that the very shallow portion of the plate interface played an important role in producing such a large earthquake and tsunami in Tohoku. Goda et al. (2014) conducted a rigorous sensitivity analysis of tsunami hazards in relation to the uncertainty of earthquake slip and fault geometry. Considering eleven inversion-based slip distributions, their results highlighted strong sensitivity of tsunami wave heights to site location and slip characteristics, and also to variations in dip.

2 Chapter 1

In this chapter we show the process of data collection and give a brief description of the resources and databases we used in the analyses described in the following chapters.
In particular, we illustrate the procedure adopted to build a unique and homogeneous database of earthquake events, and show some simple statistics on the earthquakes with magnitude larger than 6 occurred over the last 25 years. Special attention is paid to those events for which Finite-Fault Models (FFMs) are available, which turns out to be a rather small, but still significant, percentage of the total number of worldwide earthquakes.

2.1 Data collection

The first step of the present thesis consisted in the collection of available finite-fault models (FFM). FFM can be found in papers published in the literature or in specific databases, the latter alternative being preferable for a master thesis work since the former requires a long time for finding and homogenizing a sufficient amount of data. The FFMs considered here were taken from the following databases, that will be briefly described in section 1.3 later on:

- SRCMOD (http://equake-rc.info/SRCMOD/)
- USGS (http://earthquake.usgs.gov)
- Caltech (http://www.tectonics.caltech.edu/slip_history/index.html)
- UCSB (http://www.geol.ucsb.edu/faculty/ji/big_earthquakes/home.html)

We have restricted the data to FFM of earthquakes with magnitude larger than 6 and that occurred starting from 1990.

2.2 Earthquake Catalogues

In order to evaluate how representative the available FFMs are of the global seismicity, we have also considered the most important earthquake catalogues. For the first statistical considerations, a list of earthquakes was derived from the ISC-GEM Global Instrumental Earthquake Catalogue (https://www.globalquakemodel.org/what/seismic-hazard/instrumental-catalogue/) covering the time interval from 1990 to 2012. To

extend it until the end of 2015, the events of 2013, 2014 and 2015 were added from the "Reviewed" ISC Bulletin Catalogue (http://www.isc.ac.uk/iscbulletin/). The search criteria were such that only events with moment magnitude Mw and GCMT as author were selected, based on a suggestion from a personal communication with James Harris and Domenico Di Giacomo of the International Seismological Centre, who are graciously acknowledged.

Hence, a global catalogue with events of magnitude larger than 6 from 1990 to 2015 was obtained.

2.2.1 ISC-GEM

The ISC-GEM Global Instrumental Earthquake Catalogue is composed of earthquakes with homogeneous locations and magnitude estimates, determined using the same tools and techniques to the maximum possible extent. The catalogue covers 110 years of seismic events in the world, bringing together over 20,000 events (of magnitude ≥ 5.5) in a homogeneous way, with the main earthquake parameters calculated by means of the same procedure.

Each event has an M_W value, the magnitude type currently most commonly used by seismologists as well as in the engineering seismology community. Where possible, M_W is based on seismic moment (mainly earthquakes in the period 1976-2009). In other cases, new empirical relations are used to obtain proxy values of the moment magnitude (https://www.globalquakemodel.org/what/seismic-hazard/instrumental-catalogue/).

2.2.2 ISC Bulletin

The Bulletin of the International Seismological Centre is the primary output of the ISC and is regarded as the definitive record of the Earth's seismicity.

The ISC Bulletin contains data from 1900 to the present day (last accessed 2016-08-29). The ISC Bulletin relies on data contributed by seismological agencies from around the world. These data may include hypocentres, phase arrival-times, focal mechanism solutions, etc. and are automatically grouped into events, which form the basis of the ISC Bulletin (from http://www.isc.ac.uk/iscbulletin/).

2.2.3 Reading of the catalogues

The reading of the catalogue was realized with a program written in Python language. The program allows one to:

- divide all the events in classes of magnitude and count how many of them fall in every class;
- count how many events have hypocentre depth included between two assigned values;
- divide the events in different geographical significant areas;
- count how many events have FFMs;
- generate the gmt file, per every year, that will be used for the realization of the map through GMT software.

All the values of magnitude, depth and geographical coordinates analysed by this program are the ones provided by the ISC-GEM and ISC catalogues, which may slightly differ from the values provided by the authors of the FFMs we will consider afterwards.

Figure 2.1 shows the geographical distribution of the earthquakes in our global catalogue. Each event is represented by a circle with diameter growing with the magnitude and whose colour is an index of depth. As expected, earthquakes are mostly concentrated along the boundaries of the main tectonic plates in which the Earth's lithosphere is fragmented (see *Figure 2.2*).

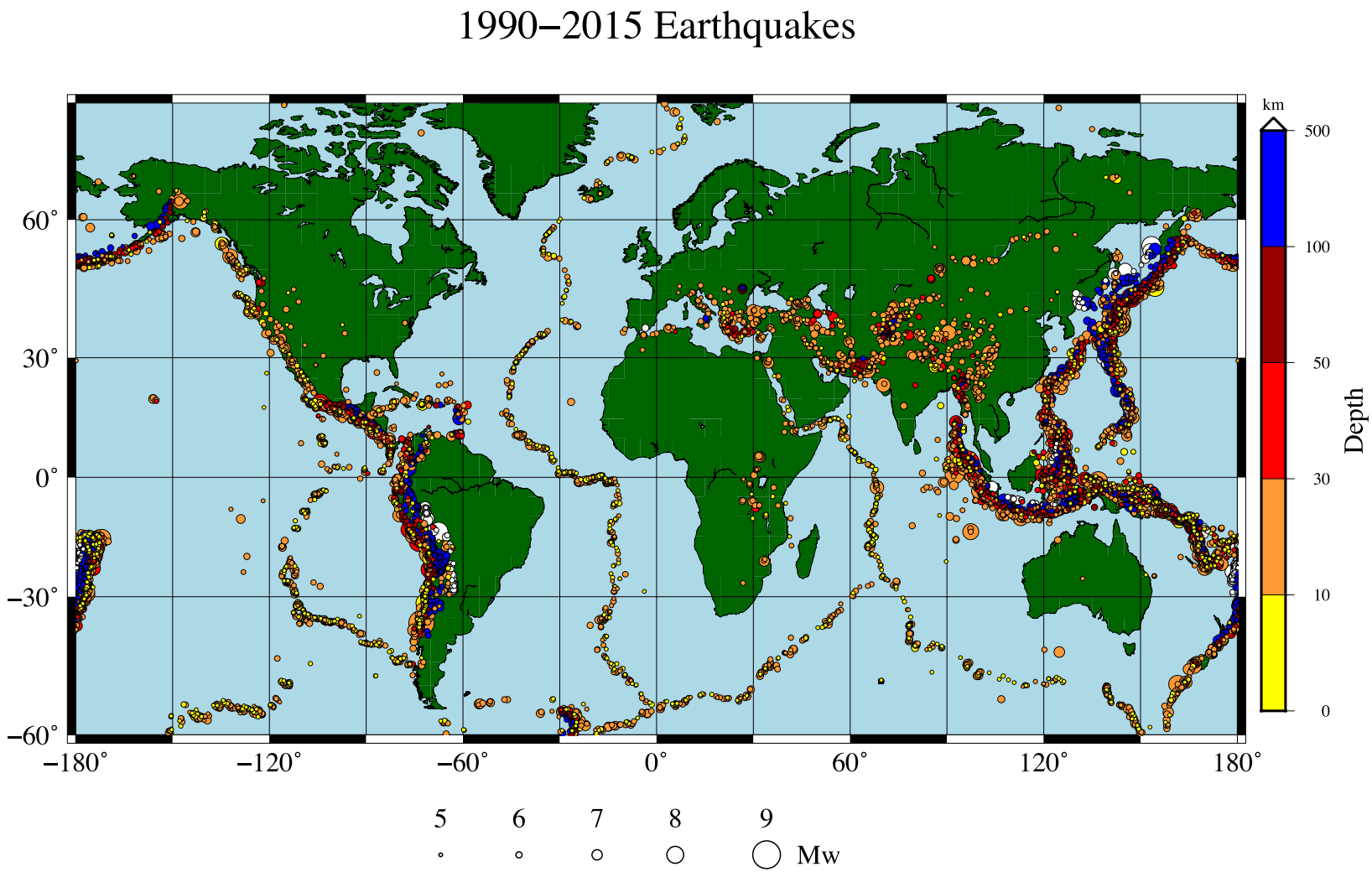

Figure 2.1: Geographical distribution of the earthquakes from the catalogue used in this first statistical analysis

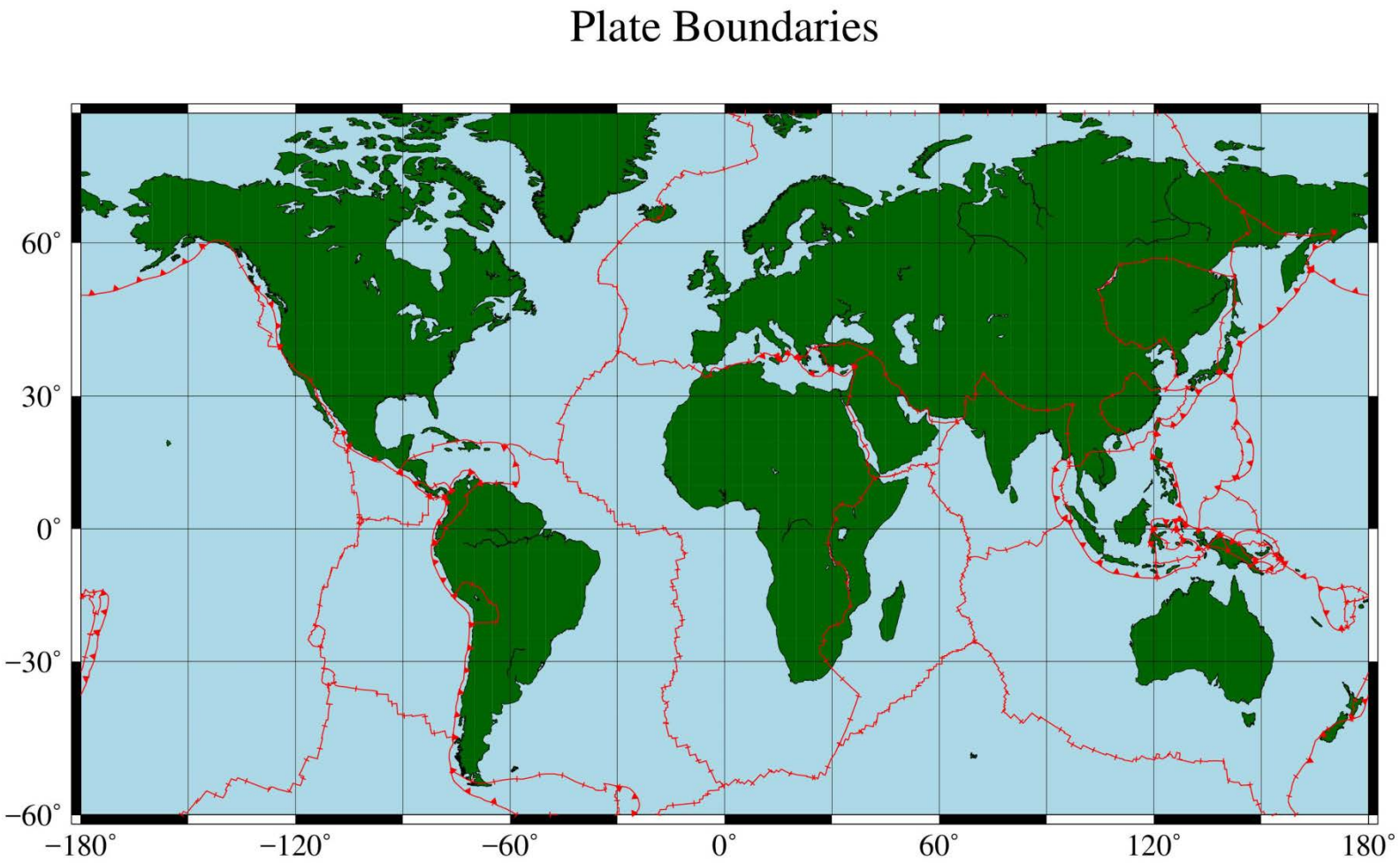

Figure 2.2: Boundaries of the main tectonic plates, as proposed by Bird (2003).

Table 2.1 shows the number of total events and the number of available FFMs from 1990 to 2015 per range of magnitude. Considering all the events with magnitude larger than 6, the percentage of FFMs we found is only 4.40%, which is quite small. It is to be noticed, however, that the percentage changes very much with the earthquake size. Indeed, for the events in the interval $6 \leq M_W < 7$ the percentage is just 0.98%, while for the ranges $7 \leq M_W < 8$ and $Mw \geq 8$, the percentage increases respectively to 30.65% and to 87.5%. These figures highlight very well that the objects of the finite-fault inversion studies are mostly the large earthquakes: this can find a reason in the fact that large earthquakes are recorded by a larger number of stations and hence documented by a larger amount of instrumental data and observations.

Table 2.1: Frequency of FFMs and of earthquakes per magnitude classes

	Finite-Fault Models	Number of Events
$M_W \geq 6$	155	3521
$6 \leq M_W < 7$	31	3161
$7 \leq M_W < 8$	103	336
$Mw \geq 8$	21	24

Table 2.2 shows the frequency of FFMs and earthquakes per hypocentre depth ranges. For both categories, the frequency decreases with the increase of depth. The highest percentage of FFMs is 5.69% and refers to shallow events with depth ≤ 20 km.

Table 2.2: Frequency of FFMs and all earthquakes per hypocentre depth classes

	Finite-Fault Models	Total Events
depth ≤ 20 km	83	1459
20 ≤ depth (km) < 100	66	1456
100 ≤ depth (km) < 500	10	441
depth ≥ 500 km	3	165

Table 2.3 gives the number of earthquakes that occurred in some selected regions, i.e. the Andean domain, the Japanese region, the Mediterranean, and the Indonesian region. The choice of these areas derives from their high seismic potential, with the exception of the Mediterranean domain, which has been selected since it is our region where we aspire to apply some of the outcomes resulting from this work.

The majority of the FFMs collected referred to the Indonesian region (12.76%), and second, really close, one finds the Mediterranean (12.50%).

The boundaries of these areas have been drawn in a rough way, i.e. by means of simple rectangular polygonal lines specified by assigning latitude and longitude of the vertices.

Table 2.3: Frequency of earthquakes in selected areas

	Finite-Fault Models	Total Events
Andean domain	14	244
Japan	21	398
Mediterranean	5	40
Indonesia	25	196

In the next pages some graphs are given that show what has been partly summarized in the previous tables, and add some new statistics.

Figure 2.3, expanding the magnitude distribution given in *Table 2.1*, shows the number of events per magnitude classes, from 1990 to 2015. Starting from $M_W = 6$, magnitudes are partitioned in bins of $M_W = 0.2$. It is evident the decrease of the number of earthquakes with the increasing of the magnitude, according to the Gutenberg-Richter law. The top-histogram in in *Figure 2.3* simply shows the number of events with the increase of magnitude. The bottom graph, instead, presents the number of events on the vertical axe in logarithmic scale: the red dots plotted are the values of the above histogram, making them correspond to the central value of the membership magnitude step.

It is evident the correlation between Log(N) and M_W (N is the number of the event for that particular magnitude value). On the graph the values of the regression laws are also reported. The trend is in agreement with the Gutenberg-Richter law:

$$N = 10^{a-bM}$$

In our case, b = 1.15.

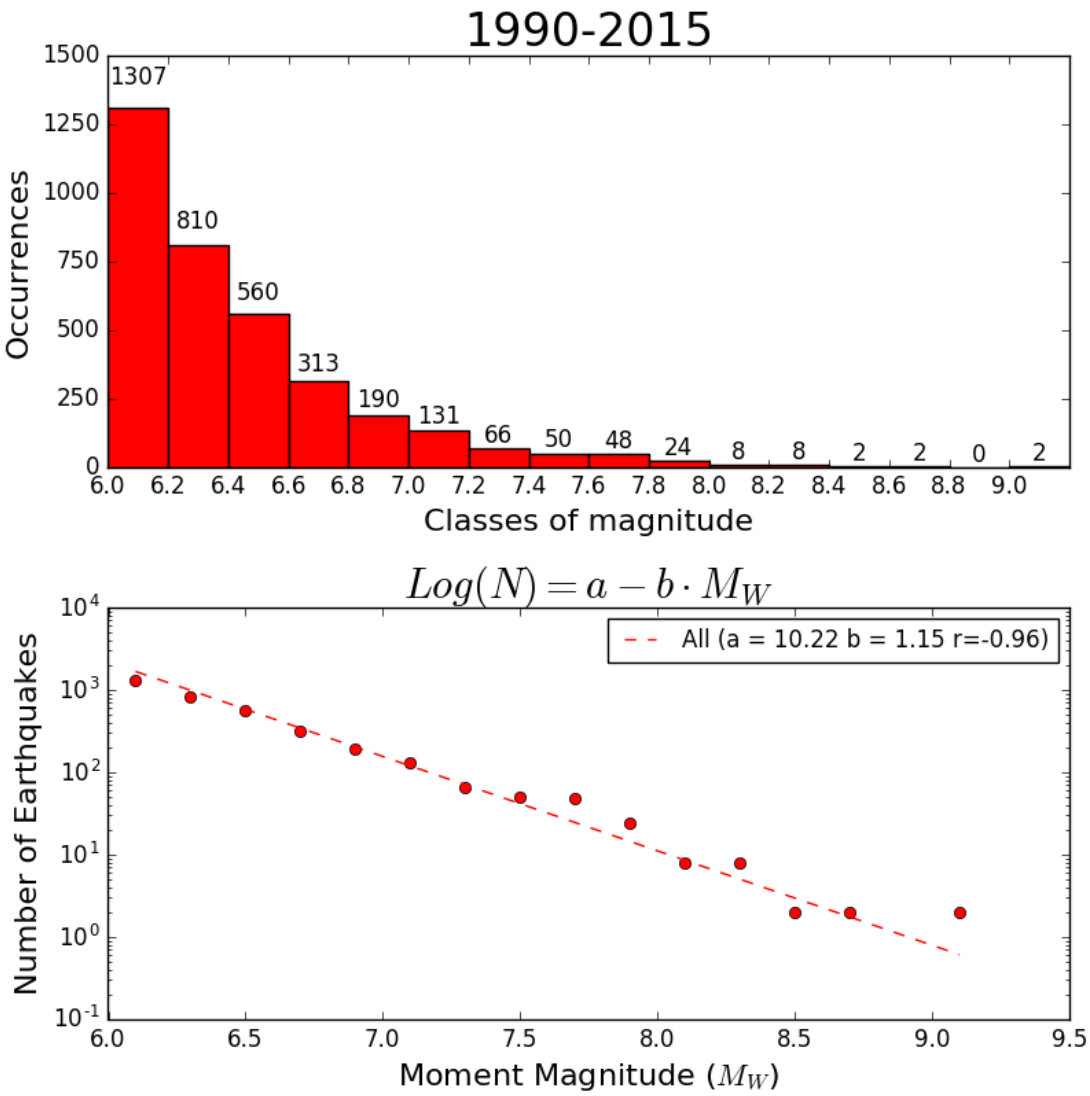

Figure 2.3: Number of events per magnitude classes

Figure 2.4 illustrates exactly what is reported in *Table 2.2*, providing a visual representation of the FFMs distribution for the different classes of magnitude.

Figure 2.5 shows the time distribution of the FFMs earthquakes, year by year, with the distinction in magnitude (6-7-8). It can be seen that there has been a growth of the available FFMs especially for earthquakes with Mw larger than 7. It can be also observed that in the last years (2014, 2015) the number slightly declines. In practice, it is expected that nowadays for each large earthquake at least one FFM is calculated, but

the final model is available in the databases with some delay that can even be as long as 1-2 years.

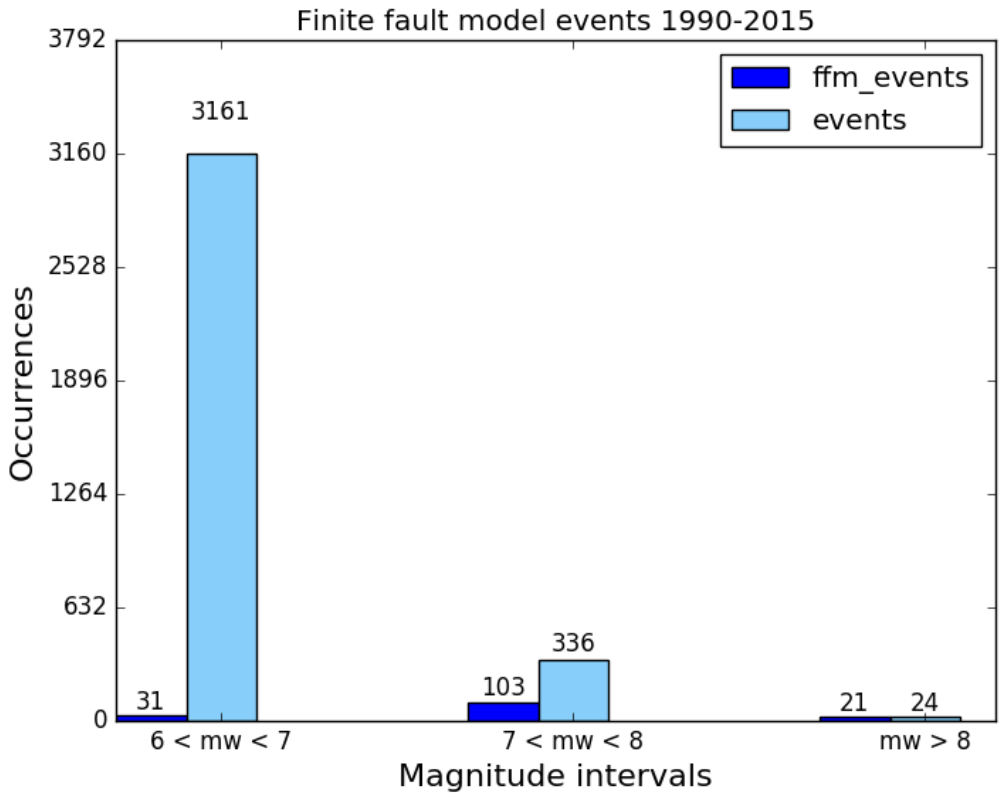

Figure 2.4: Number of events and FFMs per magnitude classes

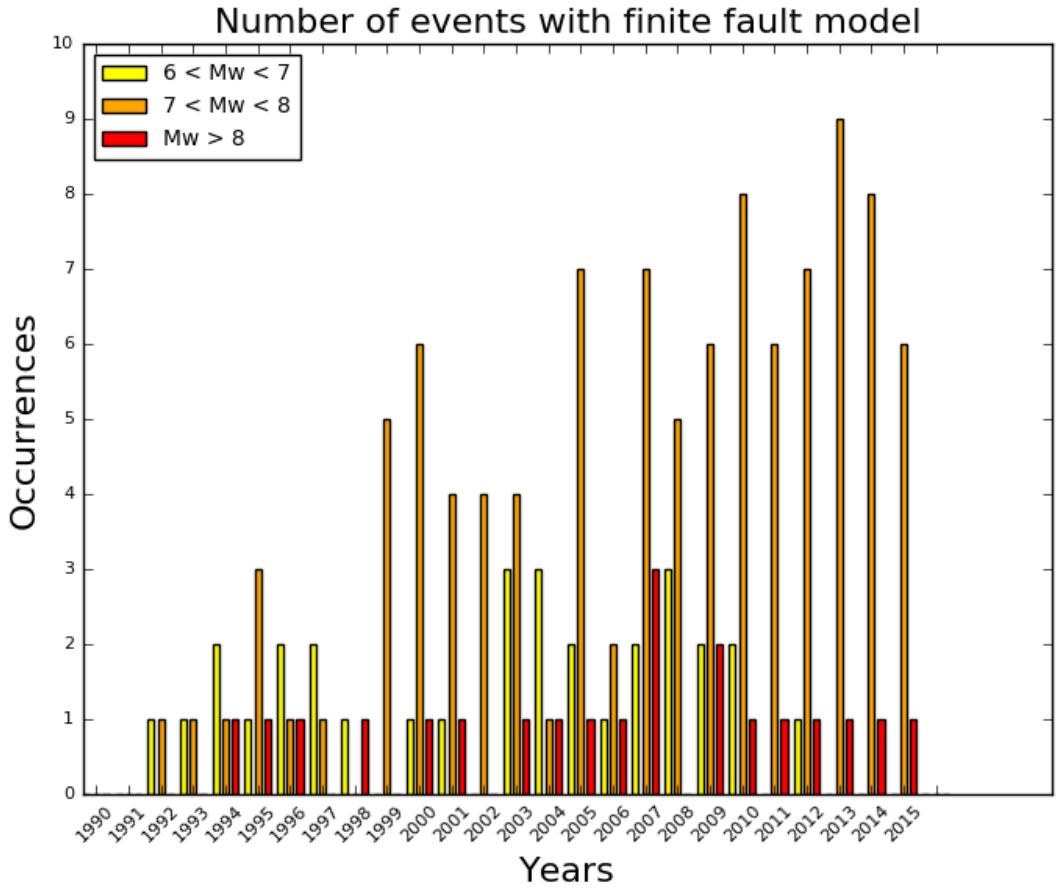

Figure 2.5: FFM events vs. time in the interval 1990-2015

Figure 2.6 and *Figure 2.7* show what is summarized in *Table 2.3* with the distinction per magnitude classes. From *Figure 2.7* one can notice that there are no events with FFM in the range $6 \leq M_W < 7$ for the Indonesian region and in the range $M_W \geq 8$ for the Mediterranean. The Andes region presents just one FFM event with magnitude lower than 7.

Comparing the two Figures, it is very interesting to observe that all the events with magnitude larger than 8 have a corresponding FFM (except one in Indonesia). The range $7 \leq M_W < 8$, instead, is perfectly covered only for the Mediterranean and Indonesian regions. The four areas are also delineated with rectangles on the map of *Figure 2.8*, which shows the geographical distribution of the events possessing an FFM.

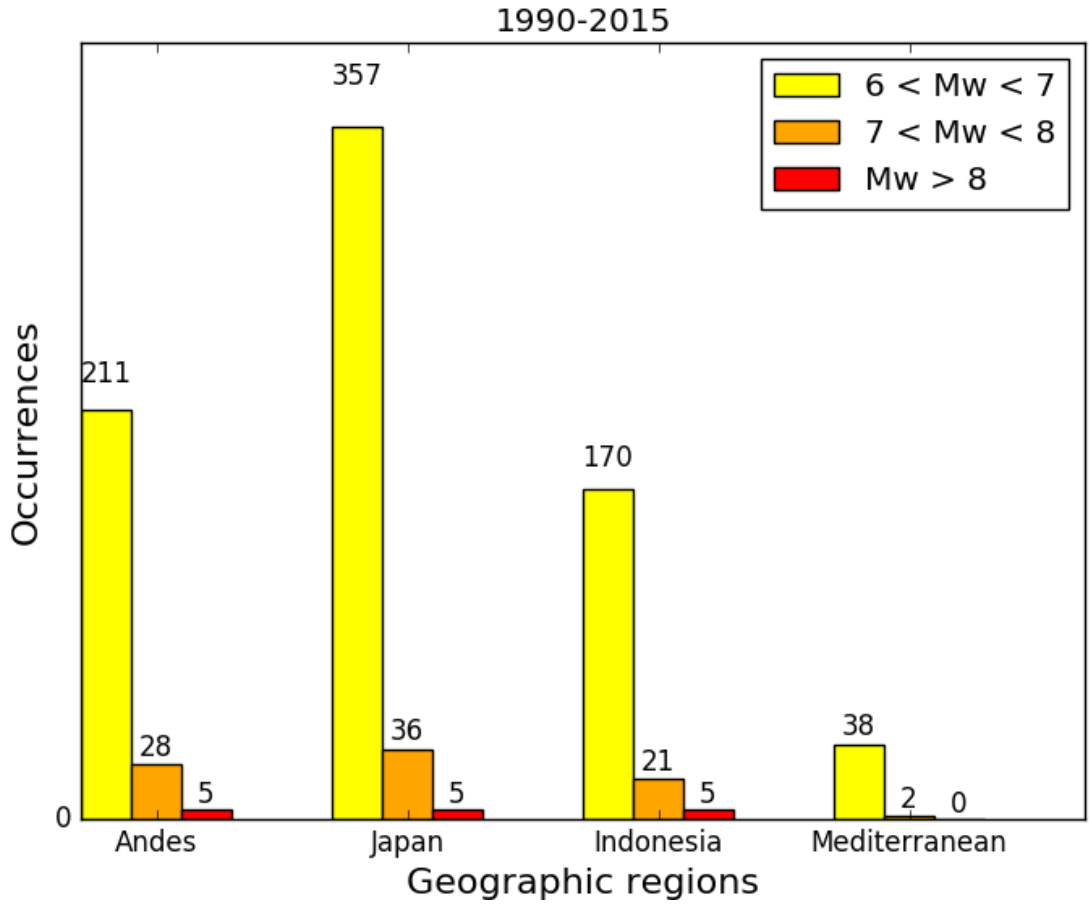

Figure 2.6: Total events in selected regions

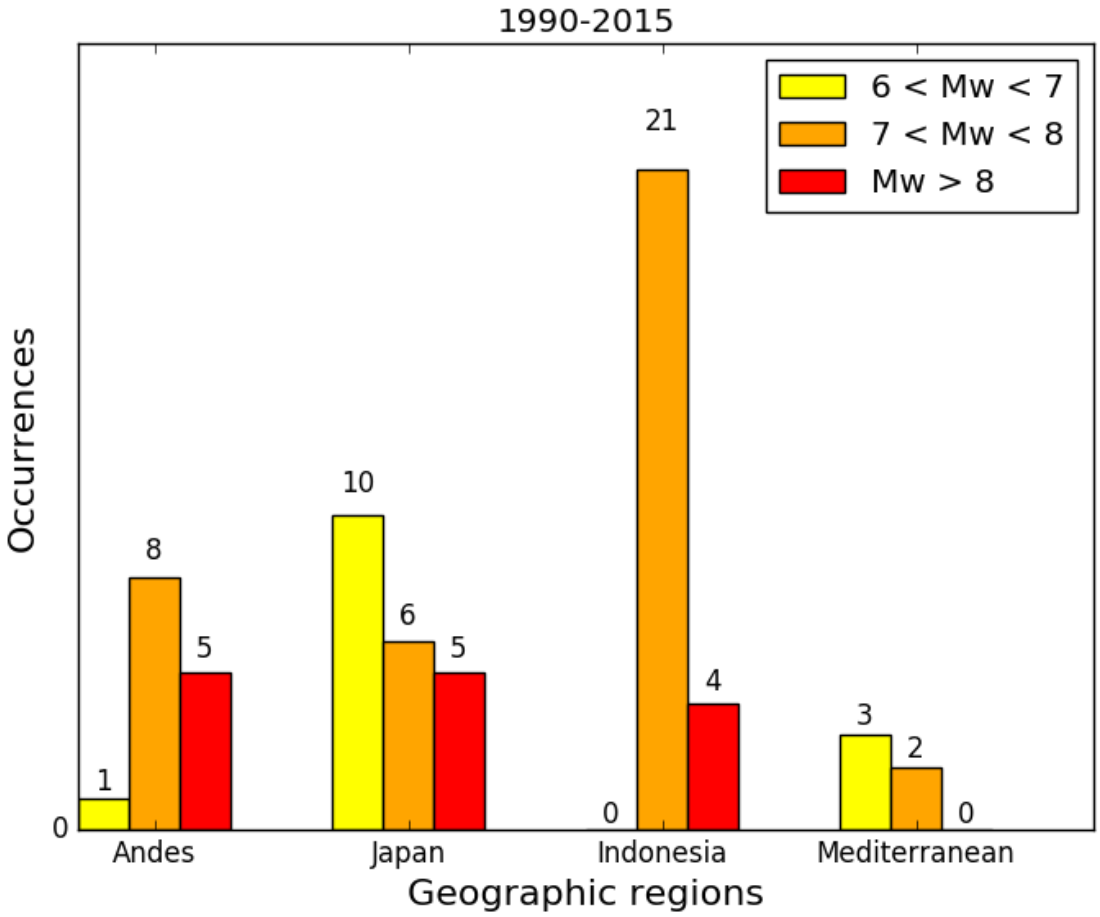

Figure 2.7: FFM events in selected regions

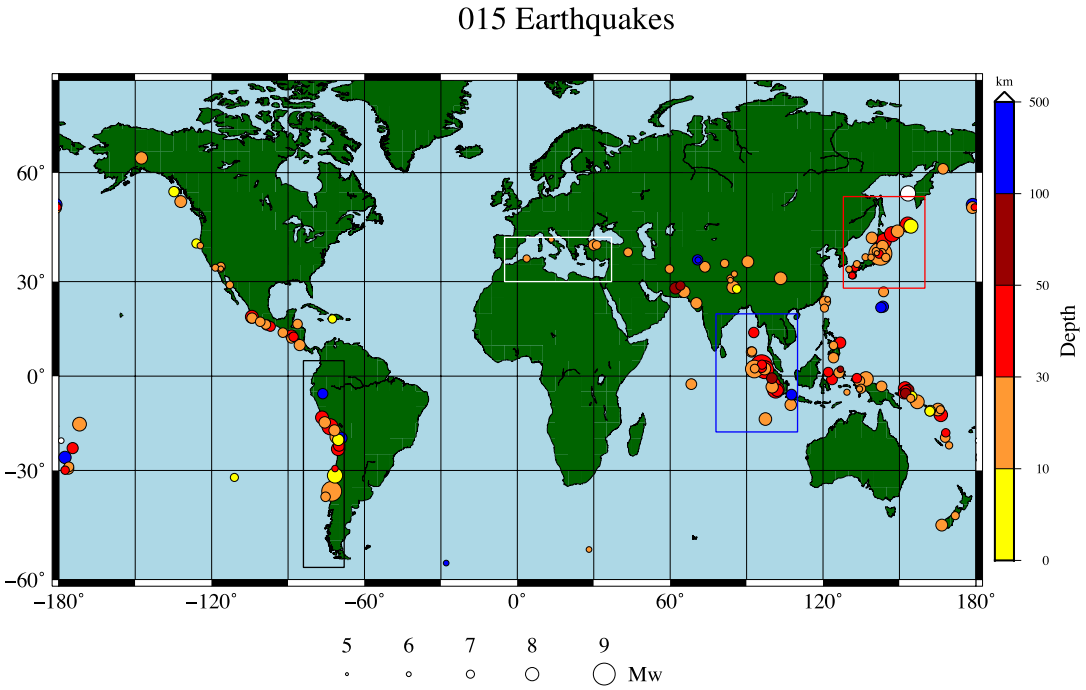

Figure 2.8: Geographical distribution of the FFM earthquakes

2.3 Finite Fault Model catalogues

Finite-fault inversions have become a topic of increasing interest in seismological research, since they allow a better understanding of the rupture mechanism and rupture evolution on the seismic fault. The data used in inversions can be of different types. They may be geodetic data of final deformation, in which case source inversions put constraints on the fault geometry and on the static slip distribution (i.e. the final displacements over the fault surface) (Mai and Thingbaijam, 2014).

Often, joint inversions, which combine available geodetic, seismic, tectonic (and when it is the case also tsunami) data, are also conducted, in order to match all the observations and provide a more detailed representation of the rupture process. Some joint inversions use all data simultaneously. Others, instead, follow an iterative approach where one set of observations is used to build an initial (prior) model for following inversions using other available data. The field of finite-fault inversion was pioneered in the early 1980s (see Olson and Apsel, 1982; Hartzell and Heaton, 1983). Subsequently, the method has been applied to numerous earthquakes (e.g., Hartzell,

1989; Hartzell et al., 1991; Wald et al., 1991; Hartzell and Langer, 1993;Wald et al., 1993; Wald and Somerville, 1995), while additional source-inversion strategies were developed and applied (e.g., Beroza and Spudich, 1988; Beroza, 1991; Hartzell and Lui, 1995; Hartzell et al., 1996; Zeng and Anderson, 1996).

Finite-fault source inversions highlight the complexity of the earthquake rupture process. The source images obtained give useful information, although with a restricted spatial resolution, of earthquake slip at depth, and potentially also on the temporal rupture evolution. Therefore, they result really important for additional work on the mechanics and kinematics of earthquake rupture processes. Hence, they play an important role in our comprehension of earthquake source dynamics.

It is beyond the scope of this thesis to treat and discuss source-inversion methods, that are the basis of the FFMs we use. In the next sub-sections we summarize the main data sources from which these models were taken.

2.3.1 USGS

The United States Geological Survey (USGS, formerly simply Geological Survey) is a scientific agency of the United States government. The organizational structure is divided into four main areas: concerning biology, geography, geology, and hydrology. The scientists of the USGS study the landscape of the United States, its natural resources, and the related natural hazards.

Many FFMs taken from USGS database and considered in the statistics are supplied by the National Earthquake Information Centre (NEIC) of United States Geological Survey. Further, several American universities are among the major contributors of these models.

2.3.2 UCSB database

This database includes a collection of rupture processes of large earthquakes (Mw>7) and interesting local events, inverted by means of the Ji's finite-fault inverse method. Only the results of recent earthquakes are provided. This work is supported, in turn, by the National Earthquake Information Center (NEIC) of the United States Geological Survey. The web page is built and maintained by Dr. C. Ji at UCSB (University of California, Santa Barbara).

(*http://www.geol.ucsb.edu/faculty/ji/big_earthquakes/home.html*)

2.3.3 Caltech

The California Institute of Technology (Caltech) has established the Tectonics Observatory in order to provide a new view of how and why the Earth's crust and lithosphere are deforming over time scales ranging from a few tens of seconds (the typical duration of an earthquake), to tens of millions of years (the time it takes to build mountains).

The Tectonics Observatory team has developed numerical models to estimate the location and amount of slip on an earthquake fault. They analyse all large earthquakes, as well as smaller ones that occur in areas of special interest to the Tectonics Observatory (*http://www.tectonics.caltech .edu /slip_history/*).

2.3.4 SRCMOD

SRCMOD website is an online database of finite-fault rupture models of past earthquakes. These earthquake source models are obtained from inversion or modelling of seismic, geodetic and other geophysical data, and characterize the space-time distribution of kinematic rupture parameters. (from *http://equake-rc.info/SRCMOD/*).

The current version of SRCMOD, directly accessible at http://equake-rc.info/SRCMOD/, provides to earthquake scientists, source modellers, and any interested user open access to more than 300 earthquake rupture models corresponding to about 100 earthquakes, in a unified representation, published over the last 30 years. The website is built on a three-tier architecture, which comprises client-side software (data presentation), server-side coding (data processing), and the back-end data storage.

Three are the file formats the primary data for the source models are stored in: 1) MATLAB (http://it.mathworks.com/products/matlab) structures (.mat files), 2) ASCII files containing finite-source parameters (.fsp files), 3) ASCII files containing a comprehensive slip model (.slp files).

We will actually focus our attention on this last data-file type.

The entire database represents an inhomogeneous global collection of earthquake rupture models. Inhomogeneous in the sense of:

- faulting type
- location of the earthquake and, consequently
- tectonic province (interplate, intraplate, subduction)
- data and observations used in the source inversion
- inversion techniques applied
- available rupture-model information provided by the authors
- model parameterizations selected and modelling choices made by the modellers.

A finite-fault (also known as kinematic) rupture model typically comprises several parameters, which include the final slip, rise time (duration of slip), rupture-onset time, and rake (angle of slip direction) (Mai and Thingbaijam, 2014). The source studies do not always invert for all these parameters. Some of them could have been fixed/assumed in advance, depending on data and the used inversion technique. The parameters may vary spatially: they are defined at node points or subfaults that constitute the rupture surface. In case of inversions using seismic data, the source time function describes the temporal slip evolution on each point of the fault and is typically chosen using a simple parametric shape or as a linear combination of many elementary slip functions (so-called multi time-window inversions) (Mai and Thingbaijam, 2014).

The spatial resolution of the model is defined by the size of the subfaults (or spacing of node points); typically, the details of the rupture process are resolved at a larger scale as a result of the chosen smoothing constraints or regularization (to handle the ill-posed inversion problem) and the trade-off between parameters (Mai et al., 2007; Monelli et al., 2009).

Thanks to the increased availability of seismic and geodetic networks, the FFM of recent earthquakes are higher detailed comparing to those of the previous decades. The number of available source models is also affected by the contribution of fast FFMs, generated from the so-called fast finite-fault inversions in a semi-automated way within hours of a sizeable earthquake and then published online on institutional web pages. But more accurate models are available with some delay, typically after several months. Scientific projects or institutions that deliver online rupture models (not only fast FFMds) include FFMs at the USGS

(http://earthquake.usgs.gov/earthquakes/eqinthenews/; last accessed August 2016), source models of large earthquakes at Caltech (http://www.tectonics.caltech.edu/slip_history/index.html; last accessed August 2016), database of big earthquakes at University of California–Santa Barbara (http://www.geol.ucsb.edu/faculty/ji/big_earthquakes/ home.html; last accessed August 2016), and source process of recent earthquakes at University of Tsukuba (http://www.geol.tsukuba.ac.jp/ ~yagi-y/eng/earthquakes.html; last accessed August 2016).

The variability in rupture models is affected by the variety of source-inversion methods and available data. Furthermore, in the current database several earthquakes have more than two rupture models. There can be a significant variability between different source models for the same event. Multiple models are available, for example to name a few, for the 1992 Landers, the 1995 Kobe, the 1999 İzmit, the 2004 Sumatra, the 2008 Wenchuan and the 2011 Tohoku earthquakes. However, the nominal uncertainties of each of the source inversions are not well known. This has been pointed out previously (e.g., Beresnev, 2003) and can be understood in the context of the data used, the model parameterizations chosen, and the inversion techniques applied in such studies (Cohee and Beroza, 1994; Das and Suhadolc, 1996; Henry et al., 2000; Graves and Wald, 2001; Yokota et al., 2001; Delouis et al., 2002).

Regarding the characteristic reported for every event, the earthquake source dimensions (i.e., length, width or area) are generally estimated prior to the inversion from the spatial distribution of aftershocks. Regarding the rupture width, the thickness of the seismogenic crust is often used to constrain it. In other cases the fault plane size is estimated using source-scaling relationships.

However, the inversion procedures commonly assume conservatively large source dimensions, so that the entire rupture can be accommodated, which leads to an overestimation of the rupture sizes with small (even zero) displacements at the fault boundaries. Thus, it is necessary to trim the rupture model by eliminating superfluous small slips at the fault edges (Mai and Thingbaijam, 2014). In the following chapter we will discuss about this procedure.

As already pointed out in section 2.1 the main analyses carried out in this thesis work are based on FFM of the SRCMOD database. The main reasons are that SRCMOD is a collector of models also from other databases, that are incorporated after accurate quality check, and that it is a user-friendly online platform, easy to use.

3 Chapter 2

In this chapter a set of earthquake source-scaling relations between geometrical properties of the seismic fault and magnitude are obtained. Such relationships are often used from seismologists and engineers in seismic hazard and risk assessments. They are also used in the frame of tsunami hazard studies, and even in the common tsunami early warning practice, where typically from the earthquake location and magnitude (available in a few minutes after the quake) one makes real-time assessment on the generated tsunami. Indeed, the source parameters of an earthquake have a significant influence on tsunami generation, as pointed out in the Introductory chapter. The detailed features of the seismic source and the heterogeneous distribution of slip along the fault plane influence the initial tsunami field, which reflects on the tsunami propagation and on the tsunami effects on the coast.

We analyse the scaling laws relating the magnitude (M_W) on one side, and some of the main fault properties such as rupture length (*Length*), rupture width (*Width*), rupture area (*Area*), maximum displacement (*MD*) and average displacement (*AD*).
As already said in the previous chapter, all FFMs we analyse are taken from SRCMOD. The total number of FFMs we considered is 98.
Every model provides the geographical coordinates of the epicentre, the hypocentre depth, the rupture width and length, the seismic moment, the magnitude. The spatial variations of the on-fault slip along the strike and down-dip directions is also provided. The slip values are assigned over a matrix of sub-faults, with assigned number of rows (*Nx*) and columns (*Nz*). The dimensions (*inDx,* i*nDz*) of the rectangle covering the entire fault are also given.

3.1 Fault size

The problem of the fault size evaluation is a sensitive issue. Establishing the rupture size of a fault (fault length or fault width) is not easy. If surface rupture occurred, for example, the fault length can be derived from the visible surface-rupture length. Alternatively, it can be estimated from the spatial extent of early aftershocks. However, these two approaches can give substantially different results (Wells and Coppersmith, 1994). As for the width, the determination of the fault width relies on aftershock only,

or, which is often the case of large strike-slip earthquakes, on the thickness of the seismogenic layer (Scholz, 1994).
Hence, the main errors in the evaluation of the fault dimension parameters can be found in the temporal evolution of the aftershock zone, in the accuracy of aftershock locations in 3D, in the interpretation of the initial extent of the aftershock sequence, in the reliability of the modelling.

As we already mentioned previously, in general, a variable slip distribution over an earthquake fault plane is obtained by inverting some kind of seismic, geodetic, tsunami, etc. data. In some cases, only one type of data is inverted, while in other cases joint inversions of different datasets are carried out. In all cases, typically, the overall dimension of the fault area to be discretized in the inversion procedure is pre-assigned based on some accepted criterion, such as general scaling laws relating earthquake magnitude and total fault area. It may happen that the predefined fault area is larger than needed.
Hence, depending on the inversion algorithm accuracy and on the quantity, quality and spatial distribution of the data to be inverted, the resulting slip matrix, that is the variable slip over the discretized rupture plane, may exhibit rows and/or columns full of zeroes along the edges. In those cases, the rupture length and width reported by the FFMs overestimate the true dimensions.
In order to get an image of the fault area affected by the seismic dislocation, we operated directly on the slip matrix with the following criterion: if there is an empty (i.e. full of zero slip values) row and/or column on the edges, we simply delete it.
Somerville et al. (1999), instead, suggested to remove from all models any rows or columns for which the mean slip was lower than a determined fraction (*0.3*) of total average slip. This criterion seems to be too drastic, at least for the purpose of our work.
The removal of part of the fault plane from the FFM implies a corresponding update of the fault dimensions. *Table 3.1* contains the minimum and average values of aspect ratio, area, length, width, mean slip before and after the filtering procedure.
Initial rupture length and width are provided by the authors of the FFM. Area and aspect ratio were directly derived from those values. The mean slip was calculated as the mean over the slip matrix given by the authors in the "*slp.txt*" file.

The final average aspect ratio (where the average is meant over all the 98 faults examined) is larger than the original one: this is due to the fact that there is a higher alteration of the down-dip dimension ($W_{after}/W_{before} = 0.941$) than of the along-strike one ($L_{after}/L_{before} = 0.995$).

Regarding the distribution of the slip, one can notice that after the trimming procedure there is an increase of *0.8 %* in the average slip value.

Table 3.1: Earthquake source average geometric parameters before and after the filtering procedure

	Before	After
Minimum aspect ratio	0.750	0.745
Average aspect ratio	2.51	2.56
Minimum Area (km^2)	100.0	90.0
Average Area (km^2)	22864	17252
Minimum Length (km)	10	10
Average Length (km)	150.51	149.81
Minimum Width (km)	10	9
Average Width (km)	70.22	66.08
Minimum mean slip (m)	0.068	0.068
Average mean slip (m)	1.23	1.24

3.2 Control of the models

The procedure of deleting the empty rows and columns on the edges does not exclude the possibility for some solutions to have many empty cells on the fault's plane or to present some very small values on the edges that do not permit to remove the edge itself. This implies some additional control. For each model the percentage of zero (Pz) slip values (*Figure 3.2*) in the matrix has been computed and, when higher than 50%, has been taken as an index of a possible anomaly, that required an individual visual checking.

This further control has led us to remove 5 anomalous FFM and to replace one FFM with another one available from a different author. The final number of FFM of our database is 98, that are the ones listed in *Table 3.3*.

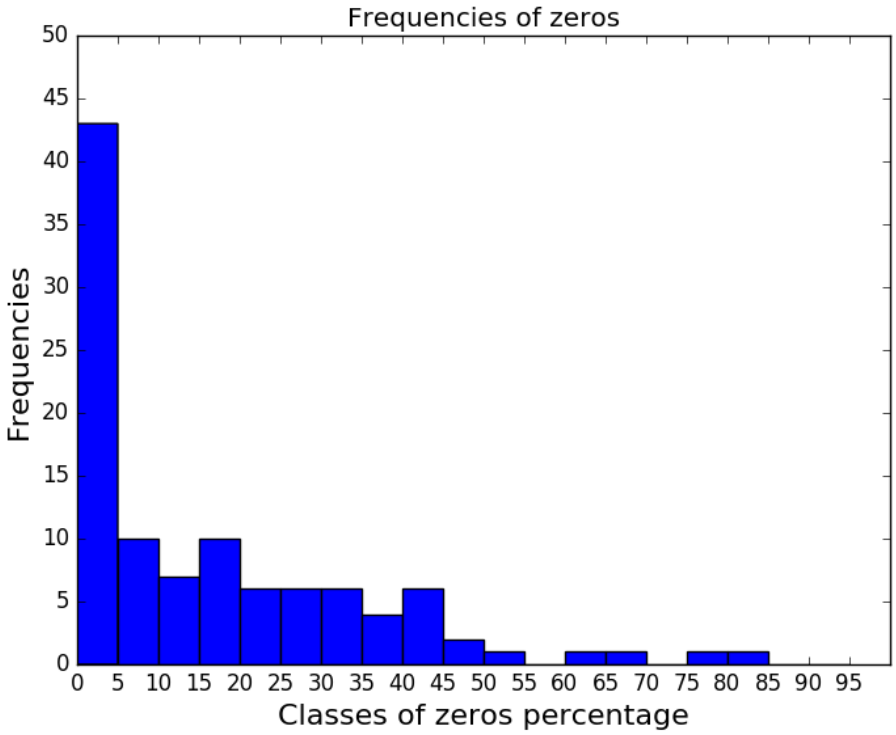

Figure 3.2: Frequency of models per classes of Pz

Below one can find the list of the anomalous events that after the visual check were either removed or modified. Usually these events are characterised by some isolated cells with small slip values that are on the edge of the fault. Killing these cells has the effect that a full row or a full column turns out to be empty and can be removed. If this "blanking" procedure produces a fault model with an empty cell percentage that is still too high (larger than 50%), the fault is removed from the database, otherwise it is kept and labelled as modified in the list below.

3.2.1 Removed Events

1994-06-05 Taiwan (Ma and Wu, 2001) Mw=6.28

It shows an isolated cell with slip of 0.39 m in the bottom right corner. Killing it and the corresponding row, lowers Pz from 80% to 70%, which is not enough.

1995-09-14 Mexico (Corboulex, 1997) Mw=7.3

After replacing in the last column two 0.10 m slip values with 0.0, Pz passes 65% to 64%.

2006-12-26 Taiwan (Yen et al., 2008) Mw=6.8

Replacing a 0.05 m slip in the second last row with a 0.0, produces a resulting Pz = 77%, which is still too high.

2007-12-09 Indonesia (Konca et al., 2008) Mw=7.9

Replacing a 0.08 m slip in the first column with a 0.0, there has been a change from Pz= 62% to 61%.

2013-04-16 Kashmir, Iran (Wei, 2013) Mw=7.8

Without anything to delete Pz remains equal to 54%.

To help understand the process, in *Figure 3.1* it is shown, as an example, the FFM by Ma and Wu (2001) of 05/06/1994 earthquake in Taiwan.
It is immediate to notice that most of the matrix cells are zero-slip (Pz=80%), and that Pz could not be reduced to less than 50% even after correcting the edge slip values.

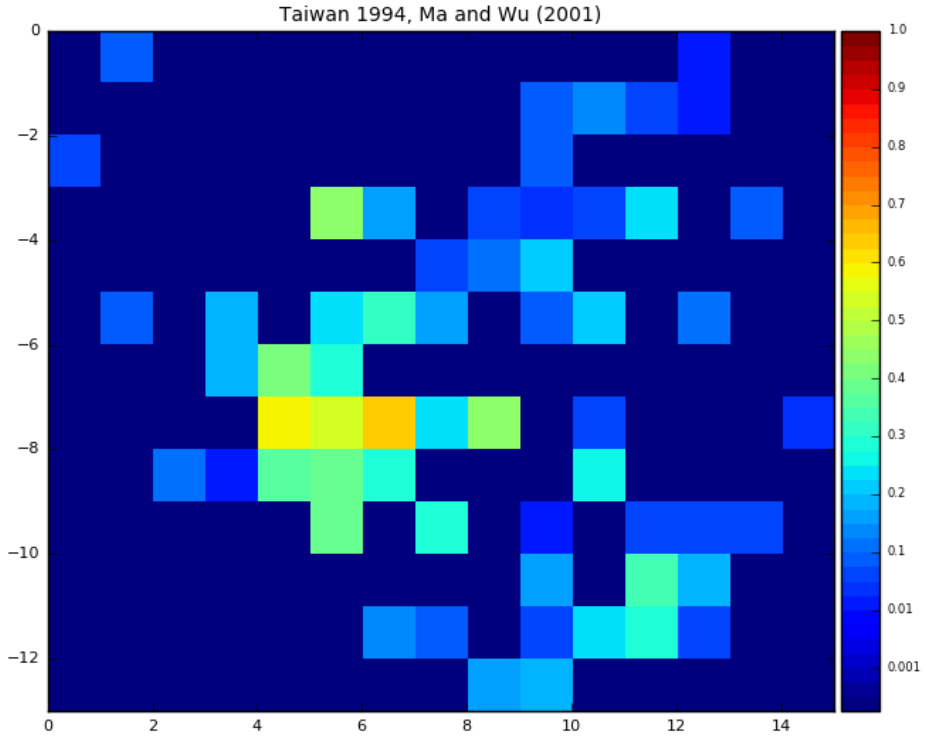

Figure 3.1: Image of one of the removed events

3.3 Events with more than one solution

Some of the events considered have more than just one FFM, which poses a problem of selection. Generally, we have selected the most recent solution, but sometimes, cross-checking different fault representations, we have made a different choice. With events with a high number of solutions, such as the 11/03/2011 Tohoku, Japan, those models that presented solutions very different from the average have been rejected.

Often, one of the discriminating criteria was the degree of fullness of the FFM slip matrix. In particular, for the event of 15/08/2007 in Peru, we noticed the lack of slip values different from zero in a significant portion of the matrix (*Figure 3.2*, left image) only after we made the visual control. So the FFM was removed from our database and an alternative model was included. The two models are shown, one next to the other, in *Figure 3.2*.

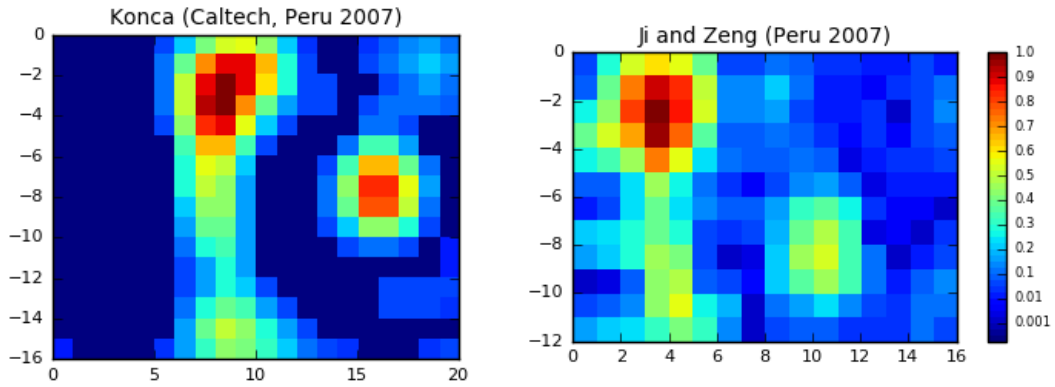

Figure 3.2: FFMs of the 2007 Peru earthquake by two different authors. On the left, the discarded model; on the right, the chosen model

The next two figures show the frequency of FFM per classes of Pz in the final dataset of 98 FFMs, (*Figure 3.3*) and similar statistics for slip values lower than 1 cm (*Figure 3.4*): for this latter case we show statistics for all the events (top-left histogram), and also for distinct magnitude classes: $6 \leq Mw < 7$ (top-right), for $7 \leq Mw < 8$ (bottom-left) and for $Mw \geq 8$ (bottom-right).

As many as 42 FFMs exhibit $Pz \leq 5\%$ of zero slip values in the slip matrix. Only 23 events have Pz larger than 25%, which means that for the remaining 75 FFMs, the zero-slip cells occupy less than a quarter of the fault plane.

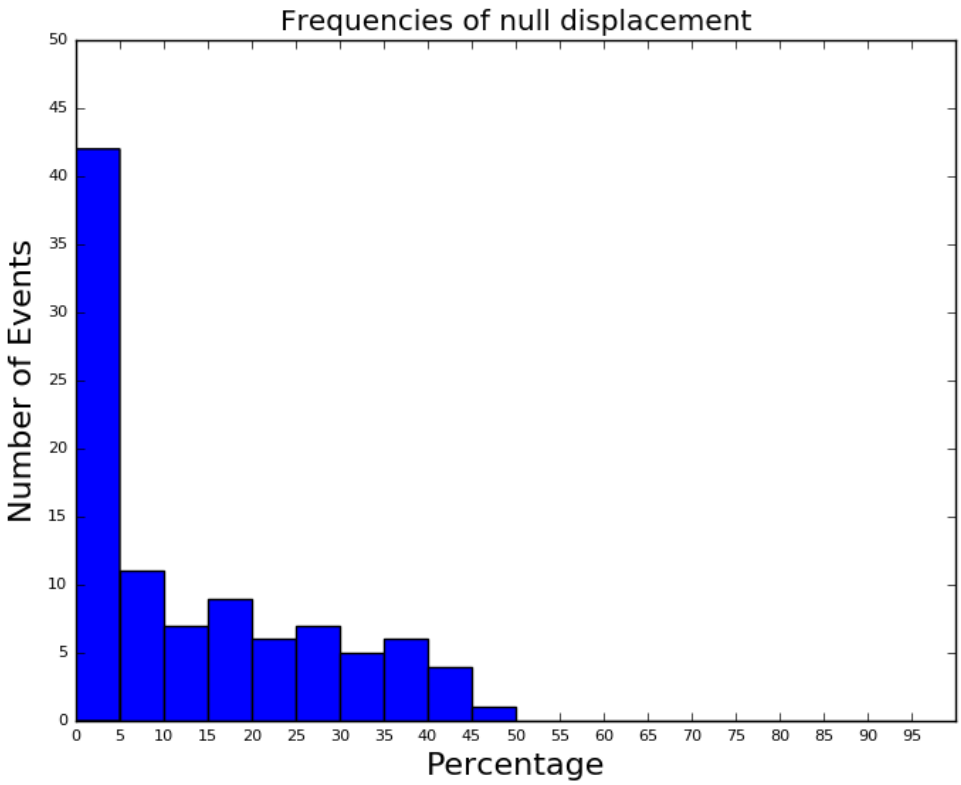

Figure 3.3: Frequency of the zero-slip cells in the set of the selected models

Figure 3.4 (first histogram) shows that about one half of FFMs exhibit a percentage of weak slip (lower than 1 cm) cells between 0-5%. It is interesting to note that there is not a great difference between the magnitude range 7 - 8 histogram (top-right) and the range 6 - 7 histogram (bottom-left). Instead, the histogram for the largest earthquakes (Mw ≥ 8) is somewhat different: here the highest percentage is smaller than 20%, and just 4 over 16 events present a percentage larger than 10%.

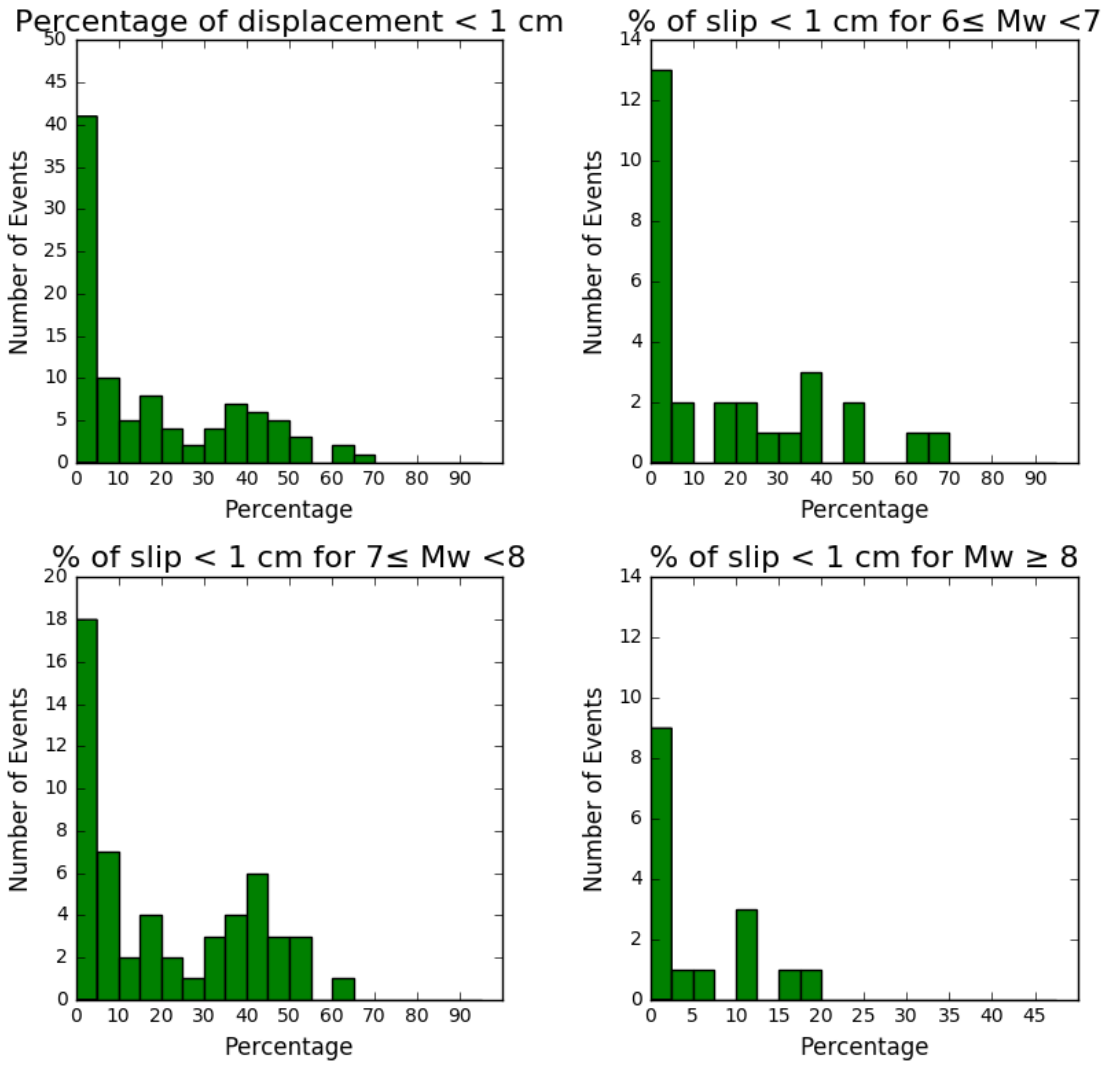

Figure 3.4: Histograms of the percentage of the small-slip (< 1cm) cells for different classes of magnitude

The next two graphs (*Figure 3.5, Figure 3.6*) show the distribution of the selected 98 FFMs per magnitude and slip type. From Figure 2.7 it is evident that the majority of the earthquakes fall in the range $7 \leq M_W \leq 8$ with a peak of 14 events centred in *7.5*, while 13 events have magnitude larger than *8*.

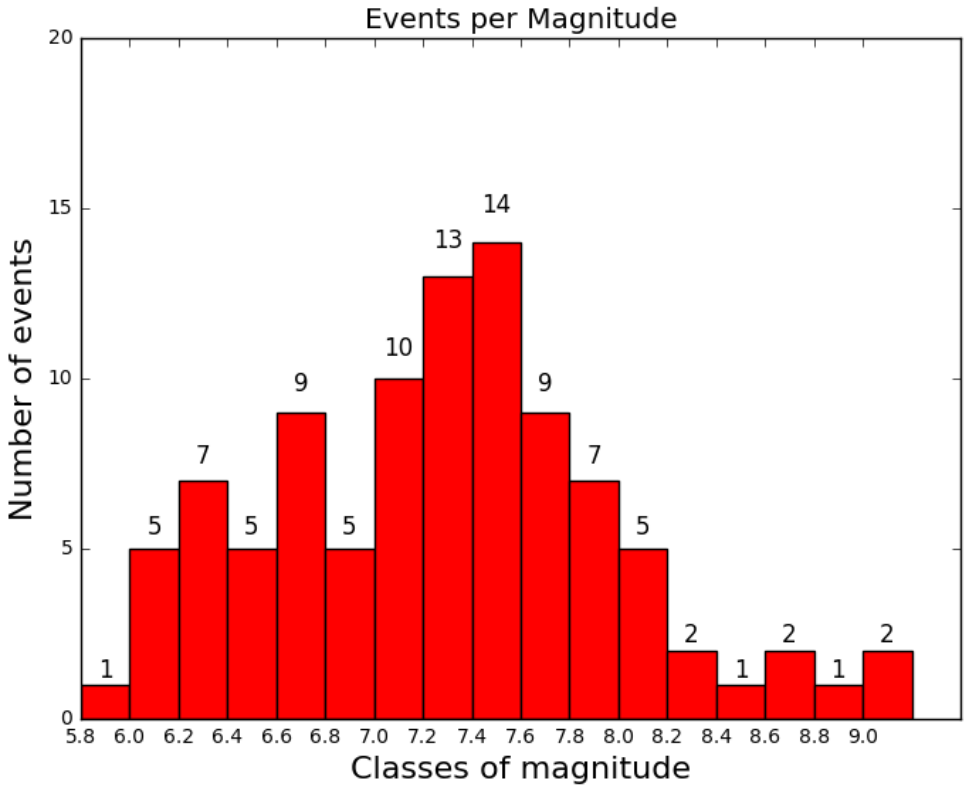

Figure 3.5: Number of FFMs per classes of magnitude (step = 0.2 Mw)

Figure 3.6 shows how many models fall in one the defined slip-type categories: 11 normal, 22 strike-slip, 32 reverse and 33 oblique events. The categories are defined here according to the slip rake. An earthquake with slip rake falling in a 10°-interval centred on 90° (-90°) is considered a reverse (normal) event. Further an earthquake with slip rake falling in a 10°-interval centred either on 0° or on 1800° is considered a strike-slip event. The "oblique" category includes all the events that do not belong to the other categories. Within the same mechanism, the events are divided into 3 classes of

magnitude ($6 \leq M_W \leq 7,\ 7 \leq M_W \leq 8,\ M_W \geq 8$): for every slip type the intermediate class is the one with the highest number of events.

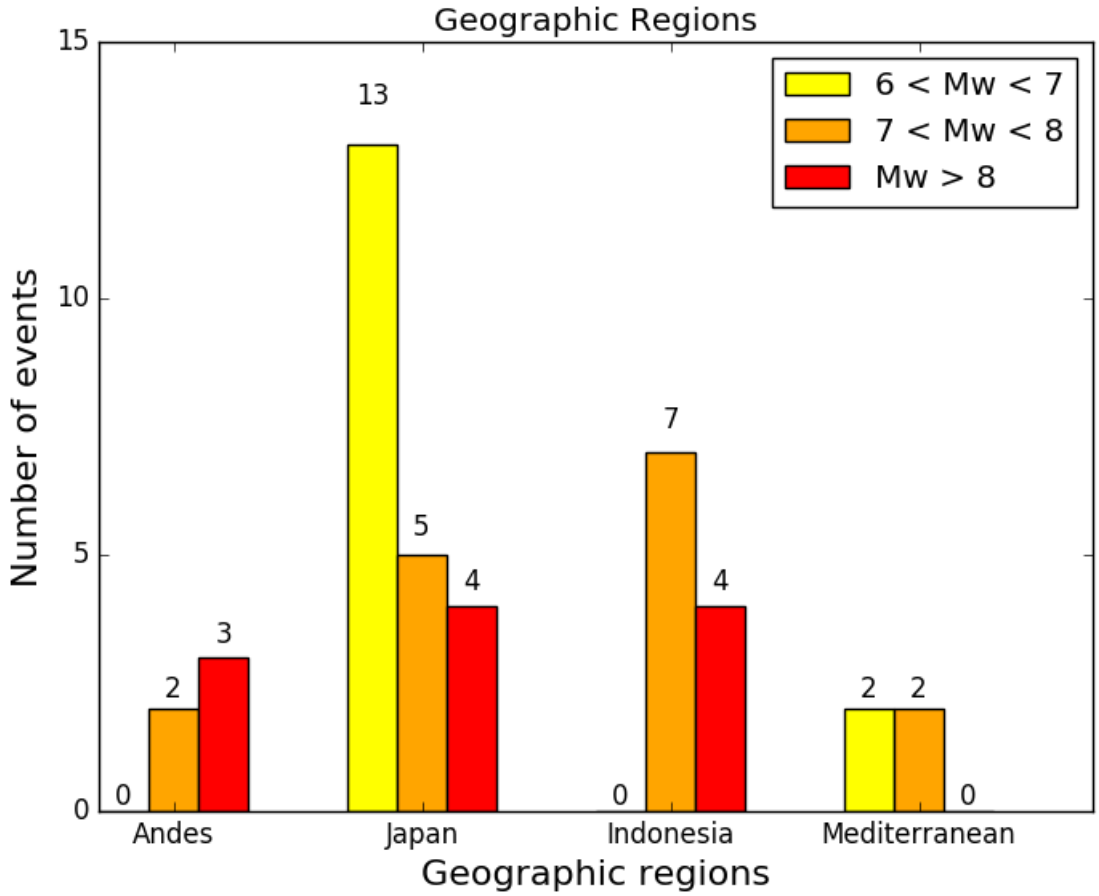

Figure 3.6: Number of FFMs per faulting style and magnitude

Below, in *Table 3.2*, it is repeated what was already reported in *Table 3.1*, but distinguishing between the different slip types. In this way, it is possible to highlight some facts. The strike-slip events are those with the lowest width (*25.52 km*), and consequently the largest average aspect ratio (*4.74*), while dip-slip events present the lowest values (in particular *1.79* for the reverse ones).

The dip-slip events (normal and reverse) are the most altered by the trimming procedure and the down-dip dimension is more altered than the along-strike one. Indeed, the new aspect ratio for dip-slip events is higher than the original one. For the strike-slip earthquakes the opposite happens: the final average aspect ratio is smaller than the original one.

Regarding the slip distribution, the strike-slip events are those with the higher mean slip (*1.59 m*), but the reverse ones are those with the largest variation, increasing the average value of *2.3%*.

Table 3.2: earthquakes' source average geometric characteristic before and after the trimming procedure for different slip-type

	SS (before)	SS (after)	Normal (before)	Normal (after)	Reverse (before)	Reverse (after)	Oblique (before)	Oblique (after)
Minimum aspect ratio	1.44	1.40	0.77	0.90	0.75	0.74	1.0	0.99
Average aspect ratio	4.74	4.70	1.95	2.00	1.66	1.79	2.04	2.05
Minimum Area (km^2)	150.0	150.0	150.0	150.0	432.0	411.25	100.0	90.0
Average Area (km^2)	4759	4728	3654	3621	50855	33709	14194	14188
Minimum Length (km)	15	15	15	15	18	17	10	10
Average Length (km)	133.43	132.38	75.81	75.54	208.76	207.59	130.30	130.15
Minimum Width (km)	10	10	10	10	18	18	10	9
Average Width (km)	25.52	25.52	36.10	35.32	116.82	104.50	66.21	66.10
Minimum mean slip (m)	0.115	0.1435	0.136	0.160	0.120	0.120	0.068	0.068
Average mean slip (m)	1.594	1.603	0.8361	0.843	1.015	1.039	1.336	1.338

3.4 The models of the study

Table 3.1 summarizes some of the main features of the earthquakes and related FFMs.

An Identification Number (I.N.) is reported for each model as well as: occurrence date and slip type, magnitude, seismic moment, hypocentre depth, rupture dimensions and area, maximum and average displacement. In the last column of the Table the author/authors of the FFM are also given.

Below this table, *Figure 3.7* represents all the models under study on the same global map: each of them is drawn with a circle whose diameter is proportional to the magnitude and whose colour is an index of depth.

Table 3.3: Finite-Fault Models used in this study

I. N.	Location	Date (m/d/y)	Slip Type	Mw	Mo	Depth (km)	L (km)	W (km)	Area (km^2)	MD (m)	AD (m)	References
1	Joshua Tree (Calif.)	04/23/1992	SS	6.2	2.70E+18	12.5	28	20	560	0.84	0.14	Bennet et al. (1995)
2	Landers (Calif.)	06/28/1992	SS	7.2	7.20E+19	7	76	15	1140	6.77	1.91	Zeng and Anderson (2000)
3	Tibet, Pumqu-Xainza	03/20/1993	O	6.3	2.97E+18	8.25	30	22	660	0.52	0.14	Wang et al. (2014)
4	Hokkaido-nansei-oki (Japan)	07/12/1993	R	7.6	2.85E+20	20	200	70	14000	4.36	0.62	Mendoza and Fukuyama (1996)
5	Northridge (Calif.)	01/17/1994	R	6.7	1.30E+19	17.5	17.5	23.5	412	4.14	0.76	Zeng and Anderson (2000)
6	Sanrikuki (Japan)	12/28/1994	R	7.7	3.99E+20	10	110	140	15400	4.03	0.71	Nagai et al. (2001)
7	Kobe (Japan)	01/16/1995	SS	6.8	1.76E+19	14	52	20	1040	2.75	0.50	Cho and Nakanishi (2000)
8	Colima (Mexico)	10/09/1995	R	8.0	9.67E+20	16.55	200	100	20000	4.77	1.18	Mendoza and Hartzell (1999)
9	Tibet, Pumqu-Xainza	07/03/1996	O	6.1	1.49E+18	8.25	25	18	450	0.45	0.10	Wang et al. (2014)
10	Hyuga-nada1 (Japan)	10/19/1996	R	6.8	1.84E+19	11.6	32.12	32.12	1032	2.92	0.54	Yagi et al. (1999)
11	Nazca Ridge (Peru)	11/12/1996	O	7.8	6.57E+20	21	180	120	21600	4.37	0.49	Salichon et al. (2003)
12	Hyuga-nada2 (Japan)	12/02/1996	R	6.7	1.19E+19	20.4	29.2	29.2	853	1.65	0.42	Yagi et al. (1999)
13	Kagoshimaen-hoku-seibu (Japan)	03/26/1997	SS	6.1	1.50E+18	7.6	15	10	150	0.87	0.34	Horikawa (2001)
14	Kagoshimaen-hoku-seibu (Japan)	05/13/1997	SS	6.0	1.16E+18	7.7	17	10	170	0.41	0.21	Horikawa (2001)
15	Antarctica (Strike-Slip Segment)	03/25/1998	SS	8.0	1.07E+21	12	290	35	10150	35.16	3.14	Antolik et al. (2000)
16	Antarctica	03/25/1998	O	7.8	4.85E+20	12	90	60	5400	21.10	2.83	Antolik et al. (2000)
17	Tibet, Pumqu-Xainza	08/25/1998	O	6.2	1.91E+18	8.25	38	23	874	0.20	0.07	Wang et al. (2014)
18	Iwate (Japan)	09/03/1998	O	6.3	3.20E+18	3	10	9	90	1.40	0.44	Nakahara et al. (2002)
19	Izmit (Turkey)	08/17/1999	SS	7.5	1.77E+20	16	160	28	4480	5.51	1.30	Cakir et al. (2004)
20	ChiChi (Taiwan)	09/20/1999	O	7.6	3.11E+20	7	78	39	3042	11.90	3.75	Sekiguchi et al. (2002)
21	Oaxaca (Mexico)	09/30/1999	N	7.5	1.82E+20	39.7	90	45	4050	2.46	0.64	Hernandez et al. (2001)
22	Hector Mine (Calif.)	10/16/1999	SS	7.1	5.82E+19	7.5	54	18	972	9.46	1.81	Salichon et al. (2004)
23	Duzce (Turkey)	11/12/1999	SS	6.7	1.28E+19	10	40.95	12.6	516	5.09	0.93	Birgoren et al. (2004)
24	Tottori (Japan)	10/06/2000	SS	6.7	1.40E+19	14.5	32	20	640	3.21	0.62	Semmane et al. (2005)a
25	Bhuj (India)	01/26/2001	R	7.4	1.33E+20	20	60	35	2100	12.44	1.51	Antolik and Dreger (2003)
26	Geiyo (Japan)	03/24/2001	R	6.7	1.19E+19	46.46	30	18	540	2.40	0.67	Kakehi (2004)
27	Denali (Alaska)	11/03/2002	SS	7.9	7.08E+20	6	292.5	18	5265	10.57	4.25	Asano et al. (2005)
28	Colima (Mexico)	01/22/2003	R	7.5	2.30E+20	20	70	85	5950	3.14	0.61	Yagi et al. (2004
29	Boumerdes (Algeria)	05/21/2003	R	7.3	8.40E+19	16	64	32	2048	3.52	1.24	Semmane et al. (2005)

30	Carlsberg Ridge	07/15/2003	SS	7.6	2.82E+20	11.32	320	36	11520	3.16	0.55	Wei (Caltech, Carlsberg 2003)
31	Miyagi-hokubu (Japan)	07/25/2003	SS	6.1	1.80E+18	6.5	18	10	180	1.03	0.31	Hikima and Koketsu (2004)
32	Tokachi-oki (Japan)	09/25/2003	R	8.2	2.36E+21	25	120	100	12000	7.06	3.11	Koketsu et al. (2004)
33	Bam, Iran	12/26/2003	O	6.5	7.30E+18	8	25	20	500	1.62	0.48	Poiata et al. (2012a)
34	Irian-Jaya, indonesia	02/07/2004	SS	7.2	7.08E+19	11.23	100	28	2800	3.37	1.03	Wei (Caltech, Irian-Jaya 2004)
35	Zhongba, Tibet	07/11/2004	N	6.2	2.24E+18	10	20	22.27	445	0.69	0.16	Elliott et al. (2010)
36	Parkfield (Calif.)	09/28/2004	O	6.1	1.36E+18	8.26	36.1	11.9	430	0.52	0.10	Custodio et al. (2005)
37	Niigata-Ken Chuetsu, Japan	10/23/2004	R	6.6	1.07E+19	10.6	28	18	504	3.08	0.67	Asano and Iwata (2009)
38	Sumatra	12/26/2004	R	9.1	6.50E+22	35	1480	224	331520	11.43	2.94	Ammon et al. (2005)
39	Fukuoka (Japan)	03/20/2005	SS	6.6	1.15E+19	14	26	18	468	2.67	0.68	Asano and Iwata (2006)
40	Sumatra	03/28/2005	O	8.7	1.17E+22	25.69	380	260	98800	12.50	2.56	Shao and Ji (UCSB, Sumatra 2005)
41	Zhongba, Tibet	04/07/2005	O	6.2	2.24E+18	5.98	28	18.72	524	1.29	0.19	Elliott et al. (2010)
42	Northern California	06/15/2005	SS	7.2	7.08E+19	9.003	102	35	3570	2.96	0.67	Shao and Ji (UCSB, Northern California 2005)
43	Honshu, Japan	08/16/2005	R	7.5	2.00E+20	34.49	96	56	5376	1.32	0.22	Shao and Ji (UCSB, Honshu 2005)
44	Kashmir, Pakistan	10/08/2005	O	7.6	2.82E+20	10.51	126	54	6804	6.37	1.75	Shao and Ji (UCSB,Kashmir 2005)
45	Kuril Islands	11/15/2006	R	8.3	3.16E+21	25.85	400	137.5	55000	8.93	1.69	Ji (UCSB, Kuril 2006)
46	Kuril Islands	01/13/2007	O	8.1	1.58E+21	18.15	200	35	7000	20.25	7.02	Ji (UCSB, Kuril 2007)
47	Noto Hanto, Japan	03/25/2007	O	6.7	1.57E+19	9.62	30	16	480	5.07	1.09	Asano and Iwata (2011)
48	Solomon islands	04/01/2007	R	8.1	1.58E+21	11.6	300	80	24000	3.73	1.47	Ji (UCSB, Solomon Islands 2007)
49	Pisco, peru	08/15/2007	O	8.0	1.12E+21	29.41	192	108	20736	8.21	1.63	Ji and Zeng (Peru 2007)
50	Niigata-ken Chuetsu-oki	08/17/2007	N	6.6	1.60E+19	8.9	33.25	29.75	990	2.58	0.32	Cirella et al. (2008)
51	Bengkulu, indonesia	09/12/2007	R	8.5	6.70E+21	21.23	400	250	100000	5.22	1.21	Gusman et al. (2010)
52	Tocopilla, Chile	11/14/2007	R	7.8	5.82E+20	36.95	375	200	75000	2.99	0.22	Ji (UCSB, Tocopilla 2007)
53	Gerze, Tibet	01/09/2008	O	6.4	4.47E+18	7.5	20	19.65	393	1.96	0.37	Elliott et al. (2010)
54	Gerze, Tibet	01/16/2008	N	5.9	7.94E+17	4	15	10	150	0.88	0.20	Elliott et al. (2010)
55	Simeulue, Indonesia	02/20/2008	R	7.4	1.41E+20	24.8	152	112	17024	1.08	0.15	Sladen (Caltech, Simeulue 2008)
56	Yutian, Tibet	03/20/2008	N	7.1	5.01E+19	4.104	54	19.05	1029	5.14	1.50	Elliott et al. (2010)
57	Wenchuan, China	05/12/2008	O	8.0	1.41E+21	16	320	60	19200	8.01	3.21	Yagi et al. (2012)
58	Iwate Miyagi Nairiku	06/13/2008	N	7.0	3.65E+19	6.5	42.66	17.38	741	6.36	1.82	Cultrera et al. (2013)
59	Zhongba, Tibet	08/25/2008	O	6.7	1.26E+19	7.626	30	30.4	912	1.54	0.25	Elliott et al. (2010)
60	Kermedac Islands, new Zealand	09/29/2008	R	7.0	3.55E+19	39.5	70	70	4900	0.98	0.14	Hayes (NEIC, New Zealand 2008)
61	Sulawesi, Indonesia	11/16/2008	R	7.3	1.00E+20	25.5	120	56	6720	2.33	0.45	Sladen (Caltech, Sulawesi 2008)

62	Papua	01/03/2009	O	7.6	2.82E+20	34.59	120	96	11520	4.96	0.59	Hayes (NEIC, Papua 2009)
63	L'Aquila, Italy	04/06/2009	N	6.3	3.13E+18	8.639	30	22	660	1.36	0.19	Gualandi et al. (2013)
64	Offshore Honduras	05/28/2009	O	7.3	1.00E+20	13.51	180	36	6480	3.09	0.58	Hayes and Ji (Offshore Honduras 2009)
65	Fiordland, New Zealand	07/15/2009	O	7.6	2.82E+20	24.14	160	96	15360	5.57	0.63	Hayes (NEIC, New Zealand 2009)
66	Java, Indonesia	07/17/2006	R	7.8	6.77E+20	15	250	140	35000	2.12	0.66	Yagi and Fukahata (2011)
67	Gulf of California	08/03/2009	SS	6.9	2.51E+19	9.163	108	20.8	2246	2.32	0.31	Hayes (NEIC, Gulf of California 2009)
68	Samoa	09/29/2009	N	8.0	1.12E+21	16.85	180	49.08	8834	14.92	3.33	Hayes (NEIC, Samoa 2009)
69	Padang, Indonesia	09/30/2009	O	7.6	2.82E+20	80	54	45	2430	5.60	1.78	Sladen (Caltech, Padang 2009)
70	Vanuatu	10/07/2009	O	7.6	2.82E+20	35	91	60	5460	2.93	0.87	Sladen (Caltech, Vanuatu 2009)
71	Haiti	01/12/2010	O	7.0	3.55E+19	11	45	22.5	1013	3.72	1.45	Sladen (Caltech, Haiti 2010)
72	Maule, Chile	02/27/2010	O	8.9	2.51E+22	37	600	187	112200	12.90	4.05	Shao et al. (UCSB, Maule 2010)
73	El Mayor-Cucapah, Mexico	04/04/2010	SS	7.4	1.20E+20	10	120	16	1920	9.25	1.89	Mendoza and Hartzell (2013)
74	Northern Sumatra	04/06/2010	R	7.8	5.62E+20	30.64	240	216	51840	3.17	0.22	Hayes (USGS, Northern Sumatra 2010)
75	Northern Sumatra	05/09/2010	R	7.2	7.08E+19	44.63	90	90	8100	1.13	0.18	Hayes (NEIC, Northern Sumatra 2010)
76	Darfield, South Island New Zealand	09/03/2010	O	7.0	3.80E+19	10.83	80	26	2080	3.51	0.60	Hayes (NEIC, Darfield 2010)
77	Sumatra	10/25/2010	R	7.7	3.98E+20	17.43	375	196	73500	1.20	0.12	Hayes (NEIC, Southern Sumatra 2010)
78	Bonin Islands	12/21/2010	O	7.4	1.41E+20	17.77	110	42	4620	3.71	0.53	Hayes (NEIC, Bonin Islands 2010)
79	Vanuatu	12/25/2010	N	7.3	1.00E+20	15.17	90	42	3780	2.82	0.44	Hayes (NEIC, Vanuatu 2010)
80	Pakistan	01/18/2011	N	7.2	7.08E+19	66.79	60	60	3600	3.49	0.33	Hayes (NEIC, Pakistan 2011)a
81	Offshore Honshu, Japan	03/09/2011	R	7.3	1.00E+20	20.72	126	126	15876	1.35	0.19	Hayes (NEIC, Offshore Honshu 2011)
82	Tohoku-Oki, japan	03/11/2011	R	9.1	5.50E+22	21	525	260	136500	48.00	9.55	Wei et al. (2012)
83	Kermadec Islands	07/06/2011	N	7.3	1.00E+20	19.04	216	72	15552	4.62	0.34	Hayes (USGS, Kermadec Islands 2011)
84	Vanuatu	08/20/2011	R	7.3	1.00E+20	31.42	102	90	9180	0.93	0.12	Hayes (NEIC, Vanuatu 2011)
85	Kermadec Islands	10/21/2011	O	7.4	1.41E+20	32.1	90	90	8100	3.19	0.28	Hayes (NEIC, Kermadec Islands 2011)
86	Van,Turkey	10/23/2011	R	7.1	5.01E+19	19	95	40	3800	4.65	0.50	Konca (2015)
87	Sumatra	01/10/2012	SS	7.2	7.08E+19	18.37	90	21	1890	6.71	1.29	Hayes (NEIC, Sumatra 2012)
88	Oaxaca, Mexico	03/20/2012	R	7.4	1.41E+20	19.74	126	108	13608	4.53	0.28	Hayes (NEIC, Oaxaca 2012)
89	Sumatra	04/11/2012	SS	8.6	8.90E+21	22	384	60	23040	34.00	8.72	Wei (Caltech, Sumatra 2012)
90	Offshore El Salvador	08/27/2012	O	7.3	1.00E+20	19.85	210	128	26880	1.06	0.09	Hayes (NEIC, Offshore El Salvador 2012)
91	East of Sulangan, Philippines	08/31/2012	O	7.6	2.72E+20	34.04	128	90	11520	3.14	0.42	Hayes (USGS, Philippines 2012)
92	Costa Rica	09/05/2012	R	7.6	2.54E+20	39.32	150	120	18000	3.05	0.29	Hayes (NEIC, Costa Rica 2012)
93	Masset,Canada	10/28/2012	R	7.8	7.00E+20	17	210	90	18900	3.16	0.60	Wei (Caltech, Masset 2012)

94	Santa Cruz islands	06/02/2013	O	8.1	1.54E+21	12.7	144	90	12960	12.70	2.86	Lay et al. (2013)
95	Okhotsk Sea	05/24/2013	SS	8.3	5.02E+21	608	195	60	11700	9.92	3.82	Ye at al. (2013)
96	Scotia Sea	11/17/2013	SS	7.7	8.94E+20	10.72	392	50	19600	4.40	0.83	Hayes (USGS, Scotia Sea 2013)
97	Iquique, Chile	04/01/2014	O	8.1	1.58E+21	21.54	285	160	45600	4.21	0.67	Wei (Caltech, Iquique 2014)
98	Gorkha, Nepal	04/25/2015	O	7.9	9.09E+20	15	160	88	14080	7.53	2.48	Yagi and Okuwaki (2015)

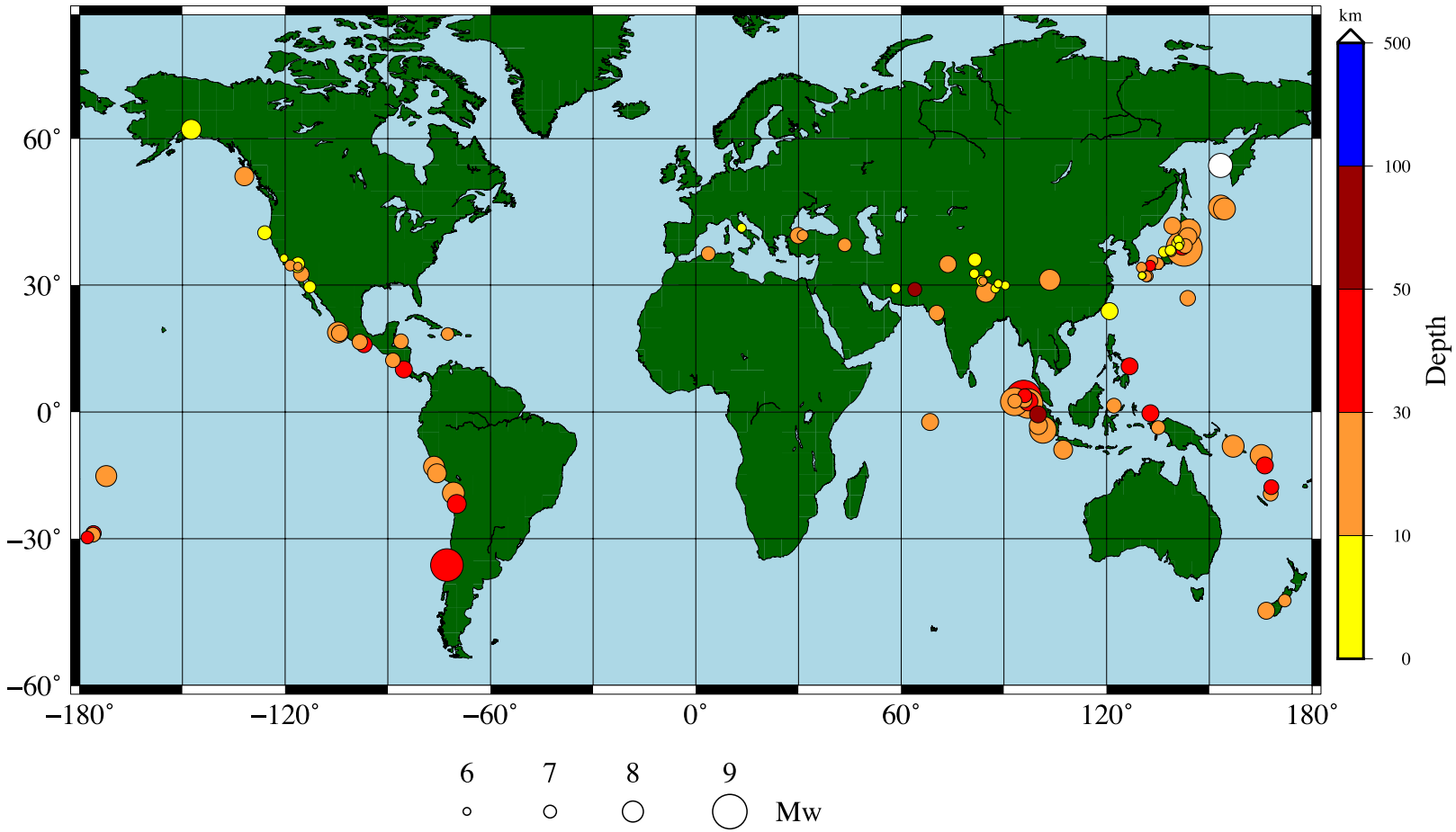

Figure 3.7: Geographical distribution of the earthquake FFMs analysed in this study (see Table 3.3)

3.5 Source scaling relationships

In *Table 3.4* the regression formulas computed in this study for maximum slip (MD), mean slip (AD), fault length (Length), fault width (Width) and fault area (Area) versus moment magnitude (M_W) are listed, divided into 5 categories: strike-slip events, reverse events, normal events, oblique events, all events (2nd column).

The number of data points used in each case is shown in the 3rd column. The best estimates for the coefficients *a* and *b* are listed in the 4th and 5th columns, followed by the coefficients of correlation *r* and the standard error σ.

For the calculations and the regressions, the magnitude values were taken with two decimal figures. However, when considered individually as estimates of the moment magnitude, they are considered significant only to one decimal figure.

Table 3.4: Direct and inverse regressions between rupture dimensions (Length, Width), rupture area (Area), maximum displacement (MD), average displacement (AD), and moment magnitude (MW) (r is the correlation coefficient and $\underline{\sigma}$ is the standard error).

Equation	Slip Type	Number of events	a	b	r	$\underline{\sigma}$
$M_W = a+b*Log(MD)$	SS	22	6.34	1.29	0.88	0.16
	R	32	7.03	1.05	0.62	0.24
	N	11	6.3	1.39	0.86	0.27
	All	98	6.65	1.23	0.75	0.11
	Oblique	33	6.61	1.33	0.85	0.15
$Log(MD) = a+b*M_W$	SS	22	-3.65	0.6	0.88	0.073
	R	32	-2.20	0.36	0.61	0.084
	N	11	-3.25	0.53	0.86	0.105
	All	98	-2.81	0.46	0.75	0.041
	Oblique	33	-3.43	0.54	0.85	0.061

Equation	Slip Type	Number of events	a	b	r	σ
M_W = a+b *Log(AD)	SS	22	7.17	1.36	0.87	0.17
	R	32	7.77	0.78	0.57	0.21
	N	11	7.26	1.06	0.74	0.32
	All	98	7.49	0.99	0.66	0.11
	Oblique	33	7.48	1.11	0.77	0.16
Log(AD) = a+b * M_W	SS	22	-4.00	0.56	0.87	0.068
	R	32	-3.36	0.41	0.57	0.108
	N	11	-3.88	0.52	0.74	0.157
	All	98	-3.45	0.45	0.66	0.051
	Oblique	33	-4.10	0.54	0.77	0.08
M_W =a+b*Log(L)	SS	22	4.38	1.44	0.93	0.12
	R	32	4.8	1.32	0.90	0.12
	N	11	4.23	1.56	0.92	0.23
	All	98	4.38	1.5	0.91	0.07
	Oblique	33	4.15	1.64	0.91	0.12
Log(L) =a+b* M_W	SS	22	-2.39	0.60	0.93	0.052
	R	32	-2.55	0.62	0.90	0.054
	N	11	-2.00	0.54	0.92	0.079
	All	98	-2.11	0.56	0.91	0.026
	Oblique	33	-1.73	0.50	0.91	0.042
M_W =a+b* Log(W)	SS	22	3.75	2.51	0.83	0.38
	R	32	4.67	1.52	0.81	0.21
	N	11	4.33	1.77	0.74	0.53
	All	98	4.84	1.49	0.8	0.11
	Oblique	33	4.31	1.80	0.87	0.18

Equation	Slip Type	Number of events	a	b	r	σ
$Log(W) = a+b * M_W$	SS	22	-0.61	0.27	0.83	0.041
	R	32	-1.33	0.43	0.81	0.058
	N	11	-0.69	0.31	0.74	0.094
	All	98	-1.47	0.43	0.8	0.032
	Oblique	33	-1.40	0.42	0.87	0.043
$M_W = a+b *Log(A)$	SS	22	3.86	1.0	0.94	0.08
	R	32	4.54	0.75	0.89	0.07
	N	11	4.01	0.91	0.88	0.16
	All	98	4.29	0.84	0.91	0.04
	Oblique	33	4.03	0.91	0.92	0.07
$Log(A) = a+b* M_W$	SS	22	-3.01	0.88	0.94	0.07
	R	32	-3.88	1.04	0.89	0.1
	N	11	-2.68	0.85	0.88	0.153
	All	98	-3.58	0.98	0.91	0.046
	Oblique	33	-3.14	0.92	0.92	0.072

Let us first consider the relationships between the fault's dimensions and the magnitude. Regarding the length of the fault plane, it results highly correlated to the magnitude, with the stronger value of the correlation coefficient for the strike-slip events.

The width presents instead a lower slope. Contrary to the length case, strike-slip events have the lowest slope with respect to the other categories: this suggests an easier rupture propagation along the strike direction for strike-slip events.

The area of the fault also increases with the magnitude, with higher values and slopes for reverse earthquakes.

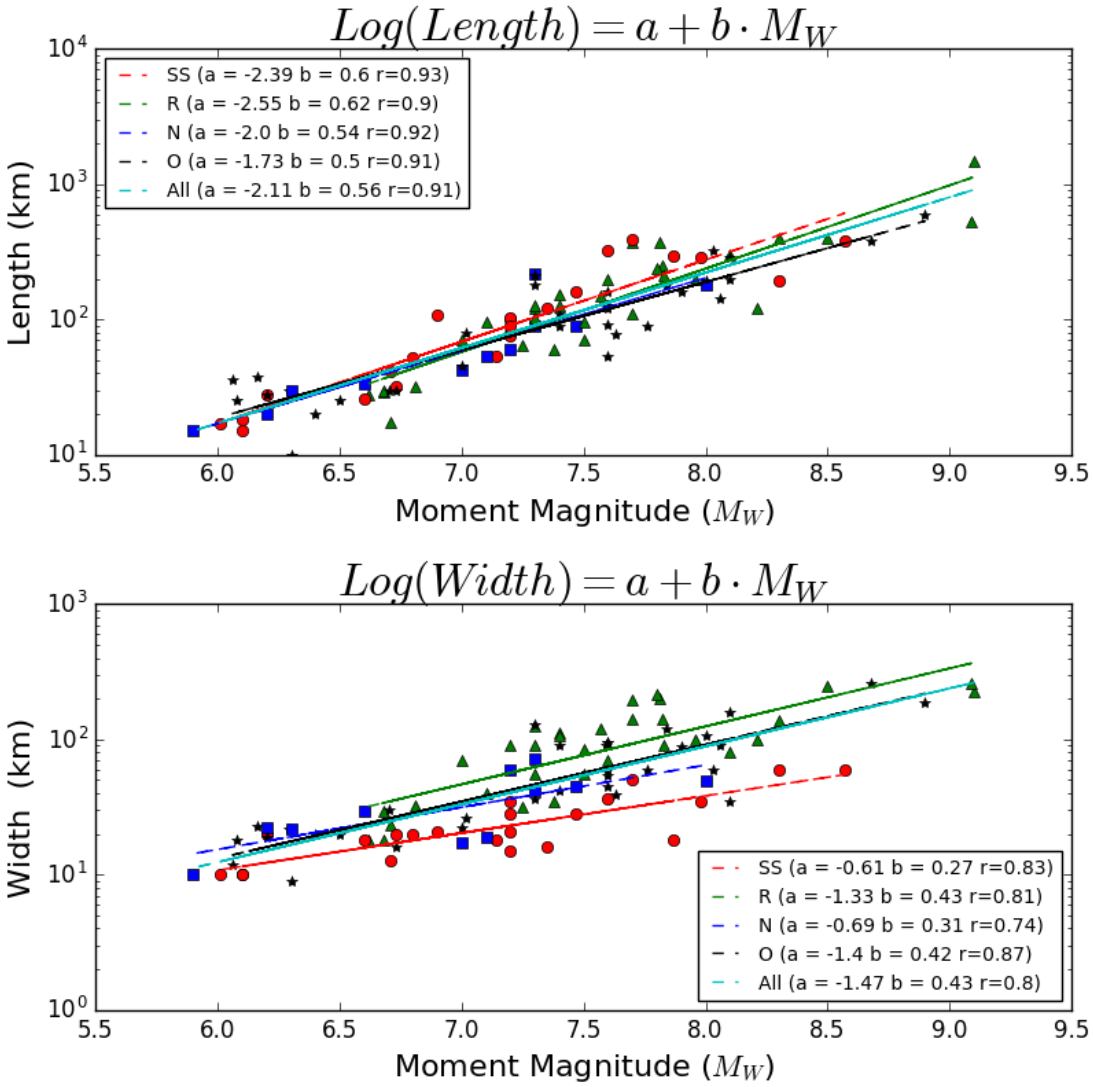

Figure 3.8: Regression law of rupture length and width vs. magnitude

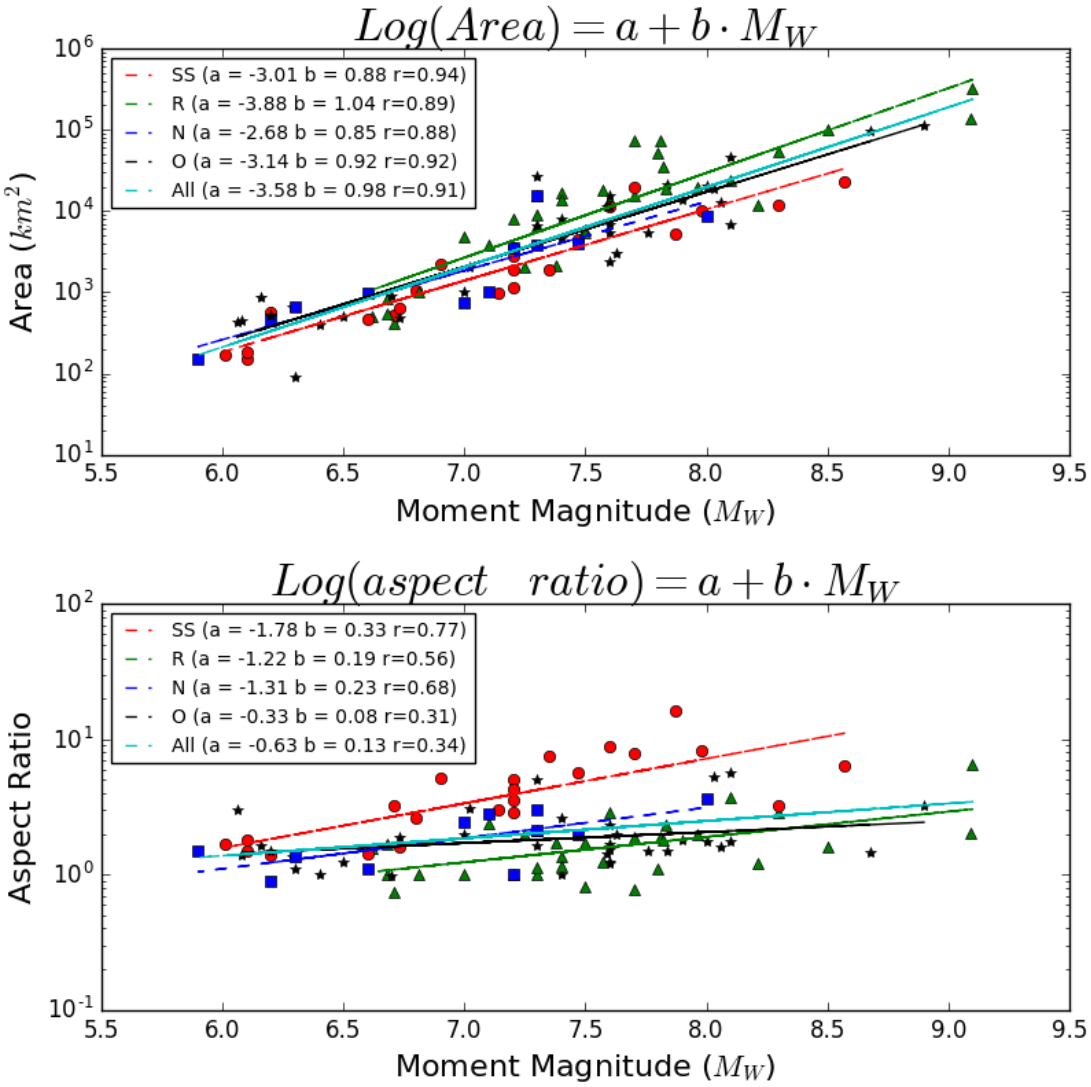

Figure 3.9: Regression laws of area and aspect ratio vs. magnitude

Considering the Maximum Displacement MD (*Figure 3.10*, top graph) one observes that it increases with the magnitude, but the correlation coefficient is not that high. The strike-slip events, for which the correlation coefficient has the highest value, generally exhibit a larger peak of slip, for a fixed magnitude, with respect to the other mechanisms.

Reverse earthquakes, instead, present the lowest value of slip peak.

The same considerations hold when one considers the average displacement (*Figure 3.10*, bottom graph).

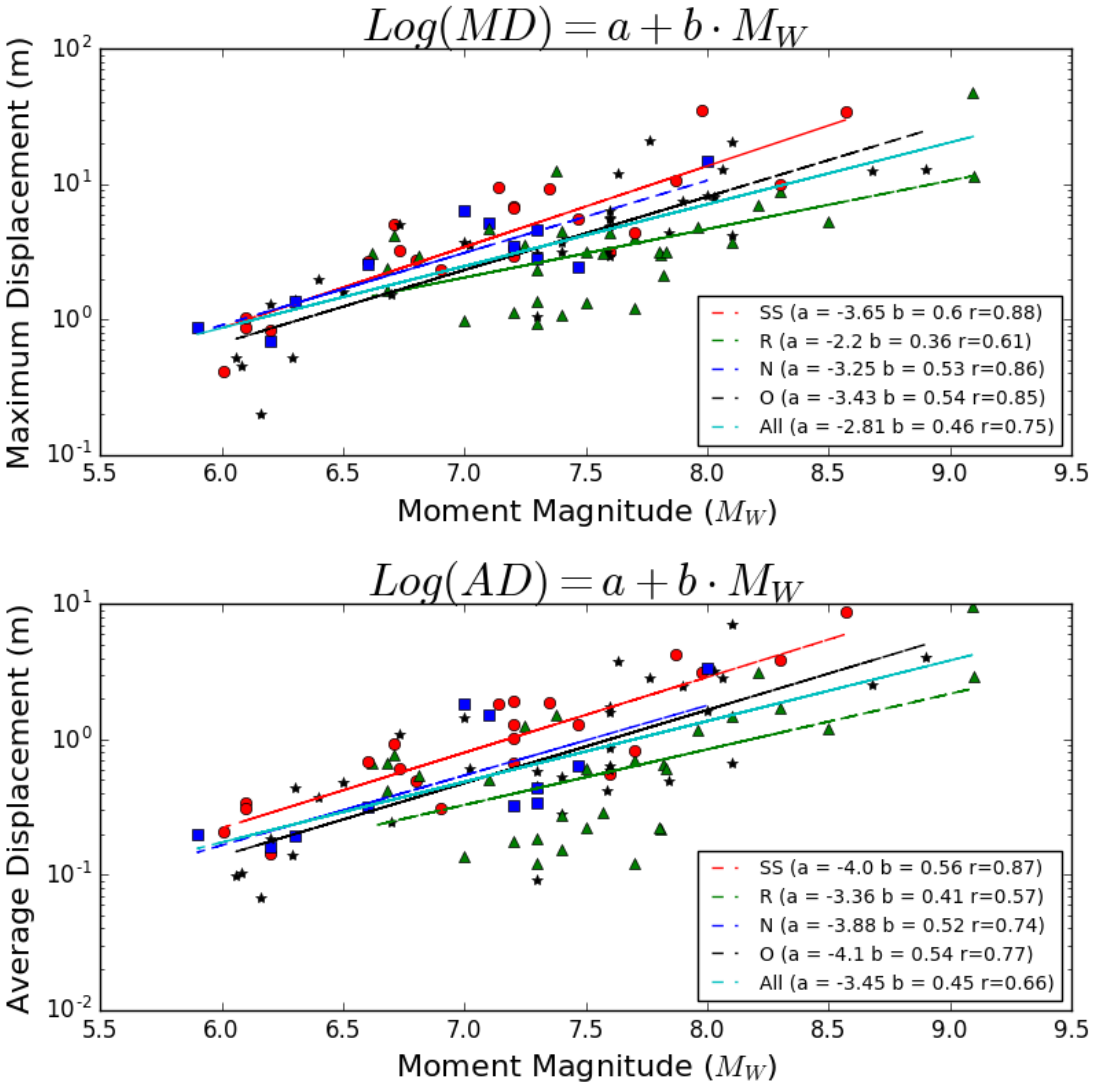

Figure 3.10: Regression laws of max and mean slip vs. magnitude

It results interesting to see if the slip correlates also with the fault dimensions. For this reason, the regression between mean slip and max slip with length is illustrated in *Figure 3.11*. The graphs show that for the displacement vs length relationships the correlation is weak ($0.35 \leq r \leq 0.77$ for *MD*, $0.2 \leq r \leq 0.69$ for *AD*), and is higher for the strike-slip events (with the exception of *MD vs. Length* that has the highest correlation for the normal events). Hence, both slip and length correlate better with the magnitude.

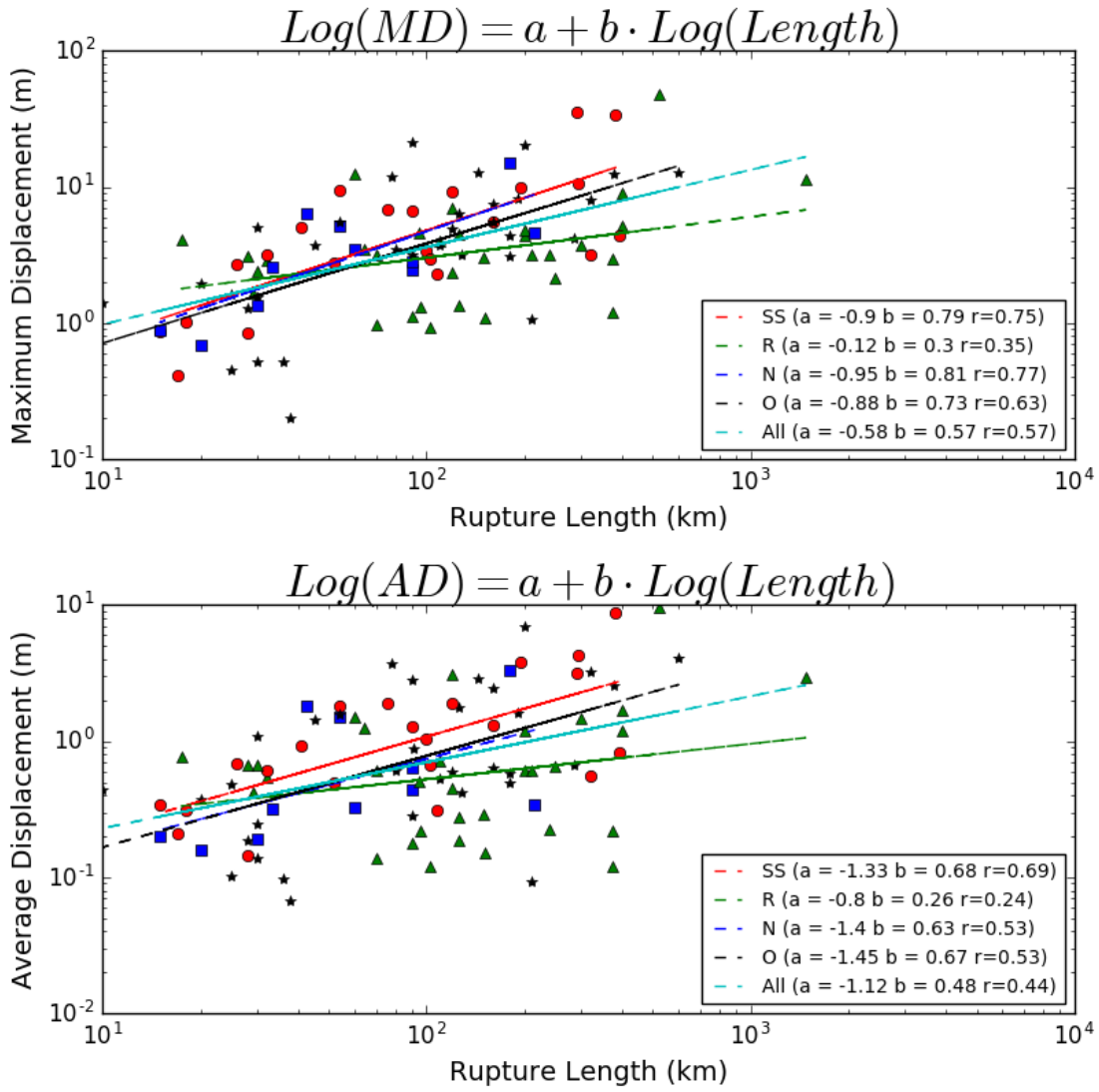

Figure 3.11: Regression law of max and mean slip vs. rupture length

Taking into account that the most widely used scaling relations are those of Wells and Coppersmith (1994), it is interesting to make some comparisons with their results.

Table 3.5: Regression laws by Wells and Coppersmith (1994)

Equation	Slip Type	Number of events	a	b	r	Standard Deviation
M_W =a+b*Log(L)	SS	93	4.33	1.49	0.96	0.24
	R	50	4.49	1.49	0.93	0.26
	N	24	4.34	1.54	0.88	0.31
	All	167	4.38	1.49	0.94	0.26
Log(L) =a+b* M_W	SS	93	-2.57	0.62	0.96	0.15
	R	50	-2.42	0.58	0.93	0.16
	N	24	-1.88	0.50	0.88	0.17
	All	167	-2.44	0.59	0.94	0.16
M_W =a+b* Log(W)	SS	87	3.80	2.59	0.84	0.45
	R	43	4.37	1.95	0.90	0.32
	N	23	4.04	2.11	0.86	0.31
	All	153	4.06	2.25	0.84	0.41
Log(W) =a+b * M_W	SS	87	-0.76	0.27	0.84	0.14
	R	43	-1.61	0.41	0.90	0.15
	N	23	-1.14	0.35	0.86	0.12
	All	153	-1.01	0.32	0.84	0.15
M_W = a+b *Log(A)	SS	83	3.98	1.02	0.96	0.23
	R	43	4.33	0.90	0.94	0.25
	N	22	3.93	1.02	0.92	0.25
	All	148	4.07	0.98	0.95	0.24
Log(A) = a+b* M_W	SS	83	-3.42	0.90	0.96	0.22
	R	43	-3.99	0.98	0.94	0.26
	N	22	-2.87	0.82	0.92	0.22
	All	148	-3.49	0.91	0.95	0.24

Regarding the rupture length, our results are in agreement with those obtained by Wells and Coppersmith (1994).

For what concerns the rupture width and magnitude, because of differences in slope and/or intercept, our relations lead to higher width and area for the same magnitude. We have to take into account that Wells and Coppersmith *(1994)* considered a larger number of events, with magnitude also smaller than *6* and *5*. This could explain why the length presents a more regular behaviour with the increase of the magnitude, while the width shows a different trend depending on the magnitude window taken into account.

Table 3.6 tests, in the case of rupture length, how close our results are to those by Wells and Coppersmith (1994). The value of Length for the different slip types calculated for an $M_W = 7.5$ is listed, as well the value of magnitude calculated for $L = 150$ *km*.

Table 3.6: Comparison on the length and magnitude values respectively predicted for a given magnitude or length

Calculated value	Slip Type	Wells and Coppersmith	This study
L (km, $M_W = 7.5$)	SS	120	129
	R	85	126
	N	74	112
	All	97	123
M_W (L = 150 km)	SS	7.57	7.51
	R	7.73	7.65
	N	7.69	7.62
	All	7.62	7.64

From *Table 3.6* it is evident that our regression laws give larger rupture length for every slip type. Again, it is important to highlight that our set of events regards only earthquakes with $M_W \geq 6$.

Figure 3.12 shows the relationship between seismic moment and magnitude. The two are perfectly correlated, which suggests that in building the FFM the two quantities have been analytically derived one from the other according to the Hanks and Kanamori law. If one wants to compare the source dimensions with the seismic moment, we can proceed following the reasoning explained below.

Calling *D* the generic source dimension one has:

$$\log_{10} D = a_d + b_d \cdot M_W$$

and accepting that

$$M_W = a_M + b_M \cdot \log_{10} M_0$$

where the coefficient values are those given by the Hanks and Kanamori law) one can conclude that:

$$\begin{cases} M_W \propto b_M \cdot \log_{10} M_0 \\ \log_{10} D \propto b_d \cdot M_W \end{cases} \quad \Longrightarrow \quad \log_{10} D \propto b_d \cdot b_M \cdot \log_{10} M_0$$

$$D \propto M_0^{b_d \cdot b_M} \implies M_0 \propto D^{\frac{1}{b_d \cdot b_M}}$$

Following this elementary algebraic strategy, we obtain from our regression laws:

$$L \propto {M_0}^{0.37} \implies M_0 \propto L^{2.71}$$
$$W \propto {M_0}^{0.28} \implies M_0 \propto W^{3.52}$$
$$A \propto {M_0}^{0.65} \implies M_0 \propto A^{1.55}$$
$$(MD) \propto {M_0}^{0.3} \implies M_0 \propto (MD)^{3.37}$$
$$(AD) \propto {M_0}^{0.3} \implies M_0 \propto (AD)^{3.37}$$

The relationships obtained are in agreement with those calculated by Mai and Beroza (2000):

$$L \propto {M_0}^{0.39}$$
$$W \propto {M_0}^{0.32}$$
$$A \propto {M_0}^{0.72}$$
$$AD \propto M_0^{0.29}$$

and are also consistent with the relation:

$$M_0 = \mu \cdot (AD) \cdot A$$

where μ is the shear modulus.

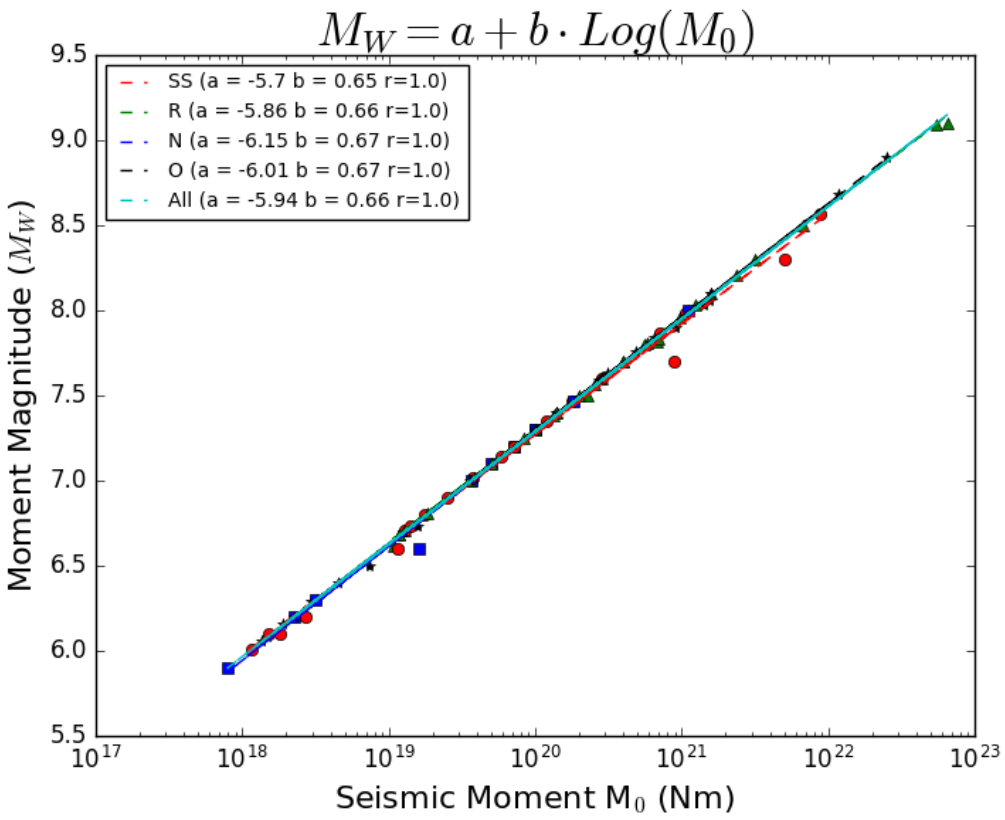

Figure 3.12: Regression law of magnitude vs. seismic moment

3.6 Conclusions

The quantity that best correlates with magnitude is the rupture area ($0.89 \leq r \leq 0.94$), followed by the rupture length ($0.90 \leq r \leq 0.93$) and rupture width ($0.74 \leq r \leq 0.87$). The slip presents a weaker correlation than the fault dimensions with the magnitude, but still stronger with magnitude than with rupture length.

The strike-slip events are those that present the best correlation among these scaling relations ($0.83 \leq r \leq 0.94$). They are also the only ones that show a correlation of the aspect ratio with the magnitude (*Figure 3.9*), with $r = 0.77$: the normal events follow with an $r = 0.68$.

The reverse events are characterized by the highest values of rupture width and area for an assigned magnitude.

4 Chapter 3

In this chapter we will discuss the position of the hypocentre with respect to the peak of slip and the areas of maximum displacement.

This can be another key to understand roughly but quickly how the rupture tends to evolve on the fault, and, so, how the slip will distribute over the fault plane. Knowing with a good probability and in a short time where the slip will be more or less intense will allow one to characterize the potential tsunami.

It has to be noticed that this is not a secondary feature, because in the very nearfield of large earthquakes, ground motions are strongly dependent on "local" directivity effects, that is, the relative position of the hypocentre with respect to regions of high slip (Mai, 2001; Guatteri et al., 2003).

These regions are known as asperities. The criterion to define an asperity is not unique. Somerville et al. (1999) define an asperity as a connected region whose average slip is 1.5 or more times larger than the average displacement over the entire fault. Alternatively, Mai et al. (2005) define asperities with respect to the maximum displacement (MD), in order to distinguish between events with rather smooth slip distributions and ruptures with complex slip distribution presenting locally very high slip values. Hence, they define as large asperities the regions where slip takes values between 1/3 and 2/3 of MD; and very large asperities the regions where the slip takes values larger than 2/3 of MD.

The rupture nucleation point is of great importance in the definition of the finite-fault inverse problem, because it is very important in spontaneous dynamic rupture modelling. The starting region of an earthquake strongly influences whether the rupture will actually propagate spontaneously or not, for some given initial stress distribution. Indeed, knowing in advance the probable rupture nucleation point for a set of initial conditions will permit to better compute the dynamic rupture process, avoiding, or at least stemming, the inconvenient and frequent trouble of rupture calculations that abort before rupturing the desired earthquake size. In finite source inversions, the rupture nucleation point is determined by waveform modelling and, hence, may differ from the actual location owing to differences between the dynamic range and the frequency

passbands of the accelerographs and of the typical high-gain seismic network stations (Mai et al. 2005).

4.1 Aspect Ratio

To provide a standard imaging of the FFMs, a careful analysis of the FFM aspect ratio has been carried out. Considering the aspect ratio frequency, shown in *Figure 4.1*, our set of 98 events was subdivided in three classes: the first class includes all events with aspect ratio between 0 and 2.4, the second class events with aspect ratio between 2.4 and 4.5, and the third one the remaining FFMs with aspect ratio between 4.5 and 9.0. Only one event, the one identified with code 27 in our list, remained out of these classes having an aspect ratio of 16.25. The reference aspect ratio of each class is the respective mean value.

Table 4.1: Number of events and reference aspect ratio for each class

	Number of Events	Mean Value
Class 1	67	1.498
Class 2	18	3.125
Class 3	12	6.462

Figure 4.1 shows the class boundaries with black dashed lines, the median aspect-ratio value in green, and the mean value in blue. More than the half of FFMs have aspect ratio lower than 2.

The choice of dividing the events in different classes of aspect ratio derives from the goal to obtain, as much as possible, standard representations of slip matrices in order to better analyse and compare slip distributions and structures. But still we cannot force to the same typical size events with very different aspect ratios, for instance with aspect ratio close to 1 and with aspect ratio much larger than 1. That led us to the creation of the three classes: in this way, we can obtain homogeneous standard representation of similar-dimension faults without altering the original proportions too much.

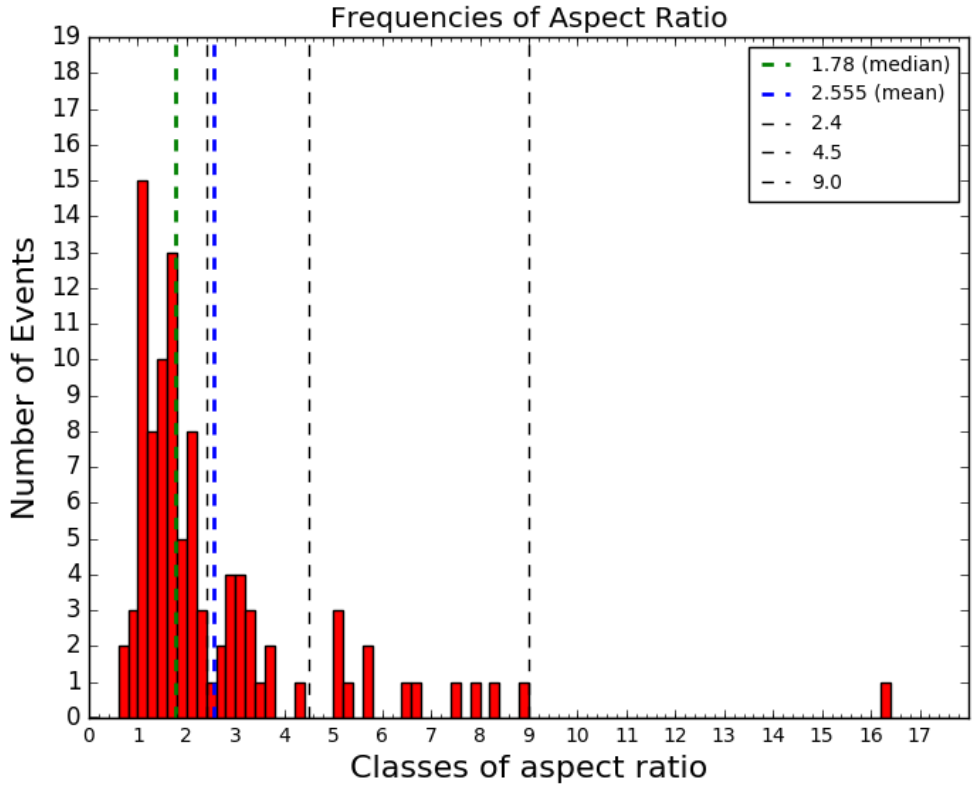

Figure 4.1: Frequency the FFM aspect ratios

4.1.1 Creation of the new images

Once the classes of aspect ratio have been established, every fault plane was standardized to its reference fault with the simple transformation law:

$$\begin{aligned} W &\rightarrow 1 \\ L &\rightarrow (A.R.)_R \\ dz &\rightarrow \frac{dz}{W} \\ dx &\rightarrow \frac{dx}{L} \cdot (A.R.)_R \end{aligned}$$

where L and W are the fault length and width respectively, dx and dz are the subfaults size in the along-strike and down-dip directions, and $(A.R.)_R$ is the reference aspect ratio. All the dimensions used in the following were rescaled according to these transformations.

4.2 Hypocentre and maximum slip

The images of the next Figure reproduce all the events, rescaled according to their reference aspect ratio, with the distribution of slip represented by a greyscale from 0 to

1, since every cell was normalized by means of the maximum slip value of the same event. These can be also called the images of the rescaled finite-fault models or RFFMs for short. On each fault, the rupture nucleation point is shown in yellow. Further, the point with the maximum displacement id displayed in red for strike-slip events, blue for normal events, green for reverse events and fuchsia for oblique events.

On the top of every image one can find in the order: the number of the event in the aspect ratio class, the number of the event in the general list (the I. N. of *Table 3.3*), the moment magnitude (Mw), the maximum displacement (MD) and the average displacement (AD).

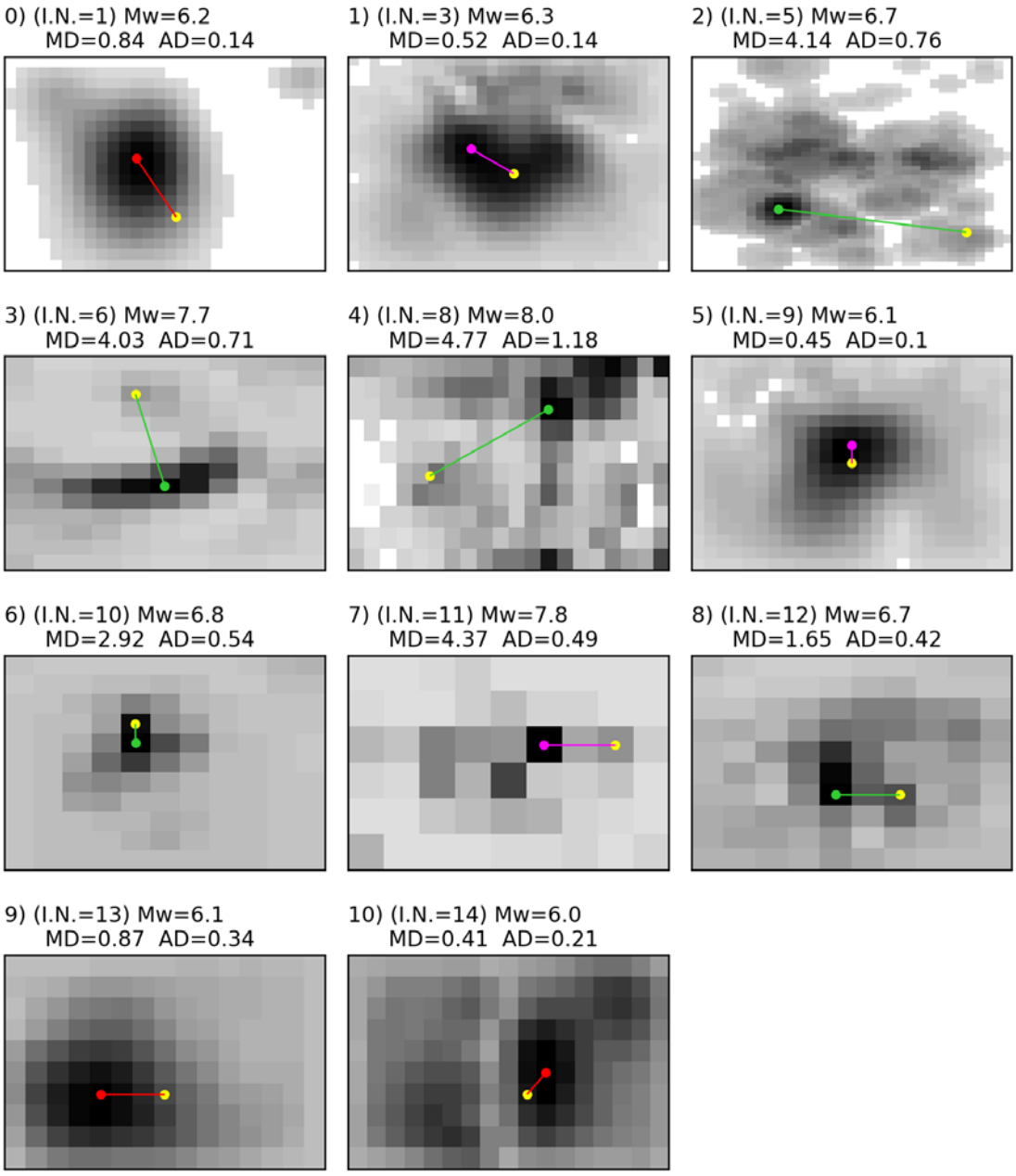

Figure 4.2: First set of RFFM images for the aspect-ratio class 1

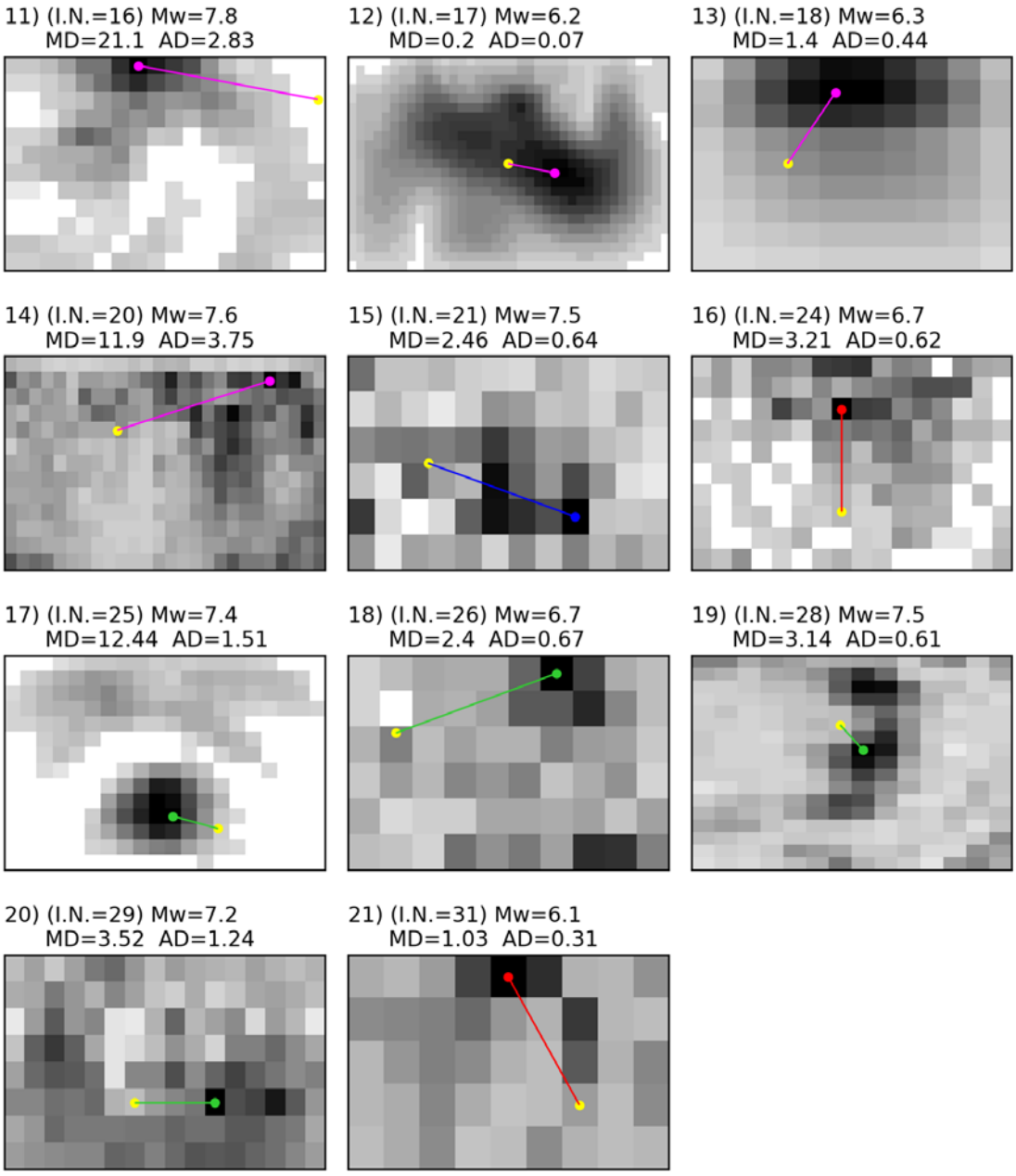

Figure 4.3: Second set of RFFM images for aspect-ratio class 1

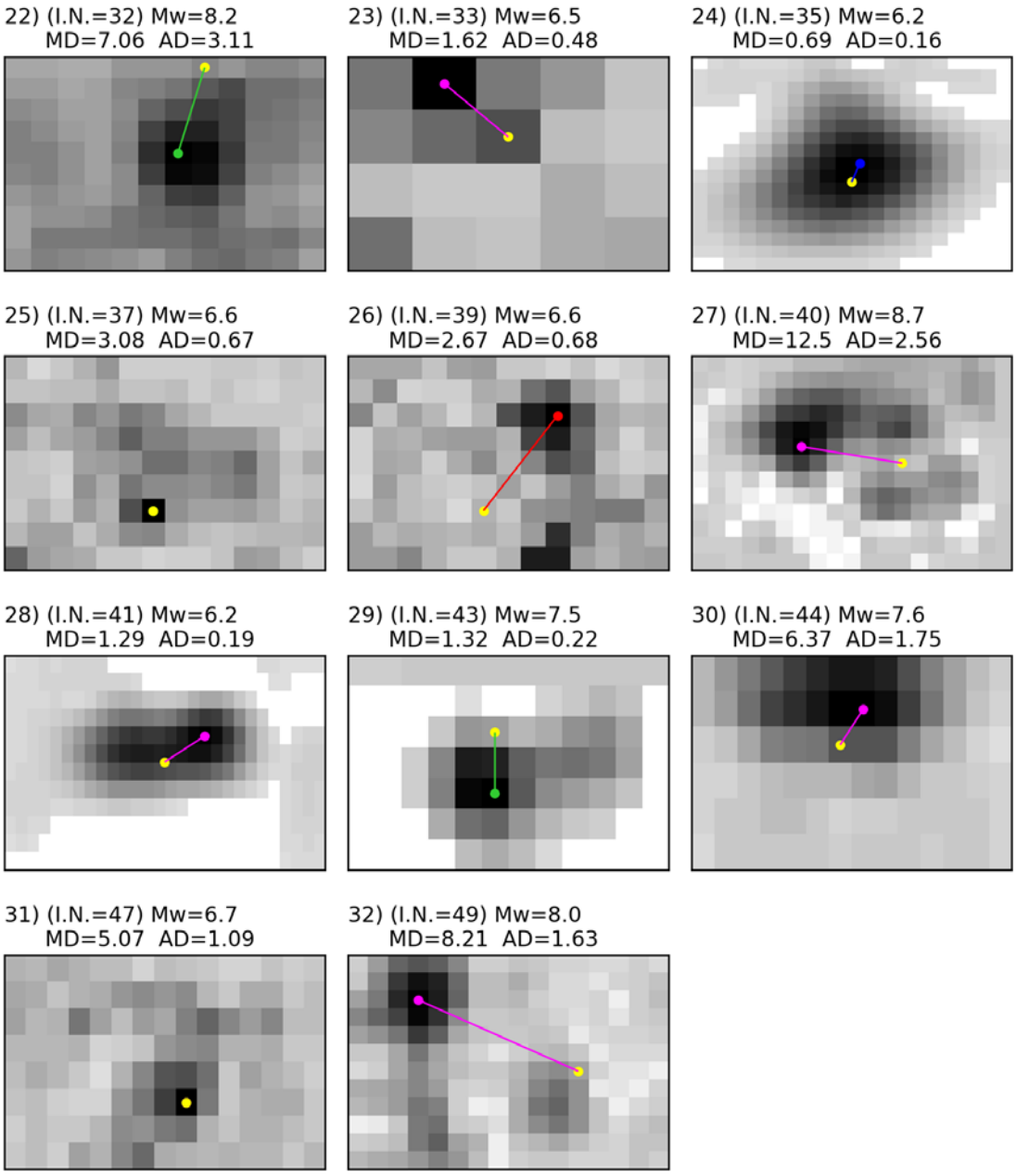

Figure 4.4: Third set of RFFM images for aspect-ratio class 1

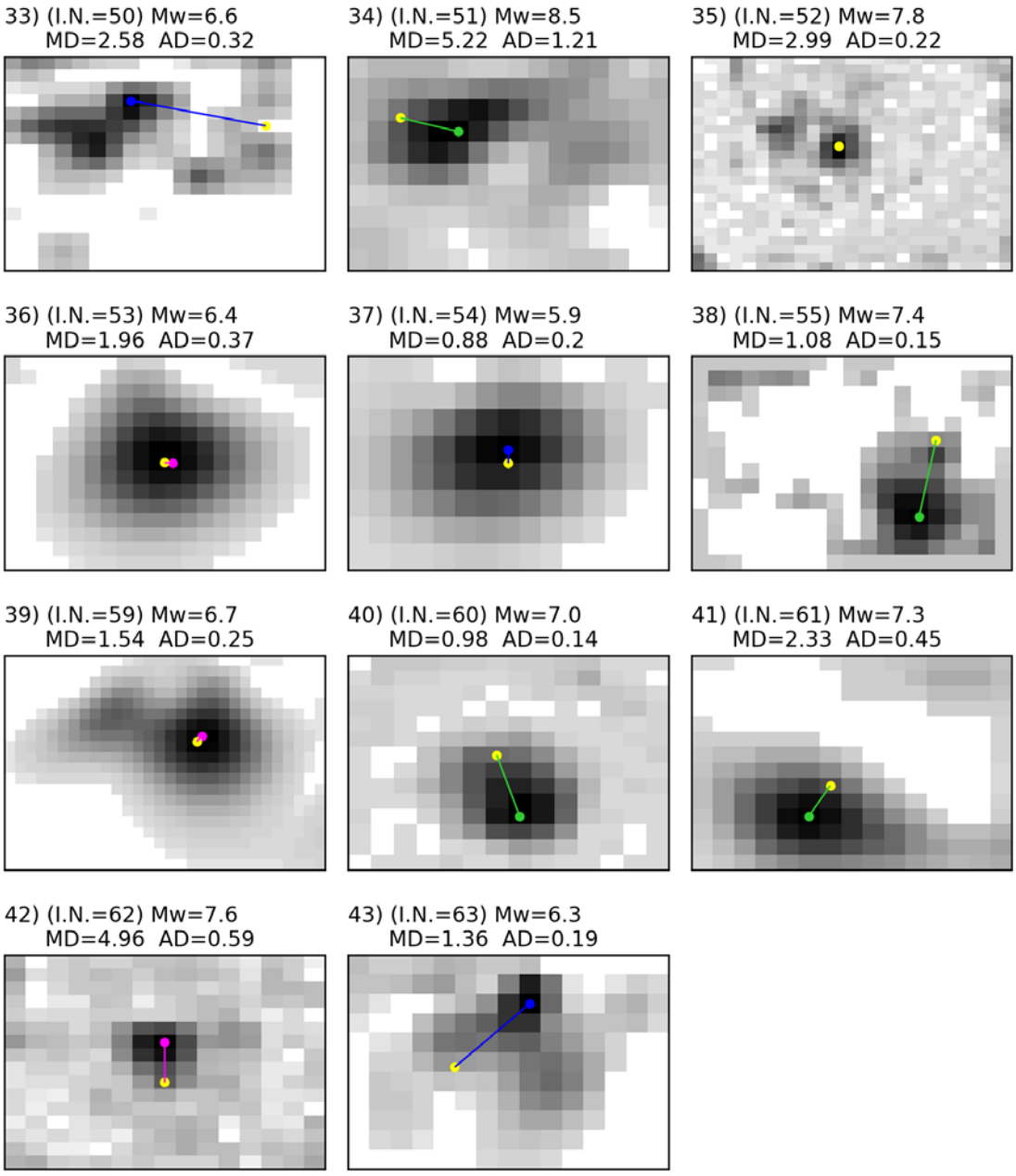

Figure 4.5: Fourth set of RFFM images for aspect-ratio class 1

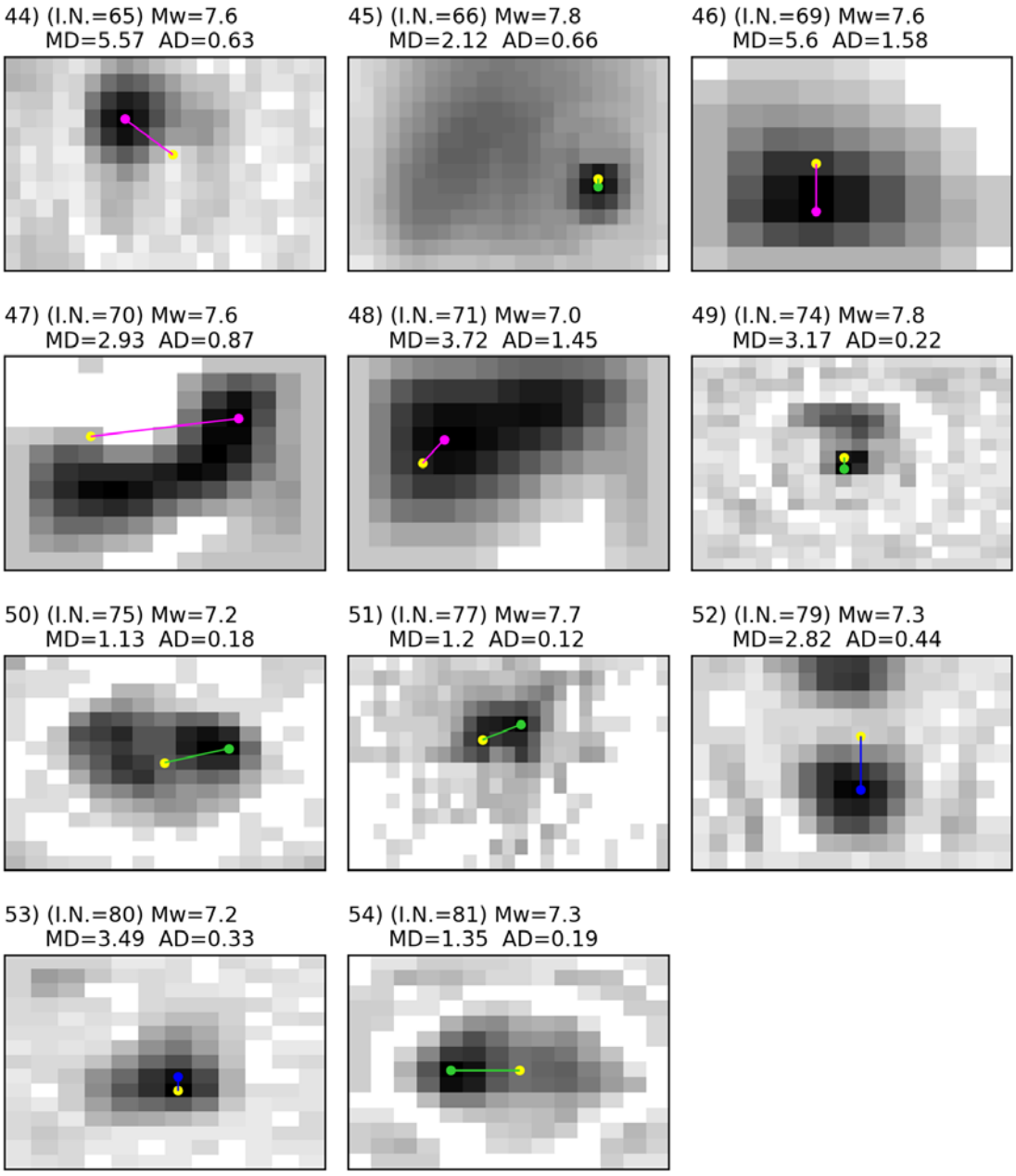

Figure 4.6: Fifth set of RFFM images for aspect- ratio class 1

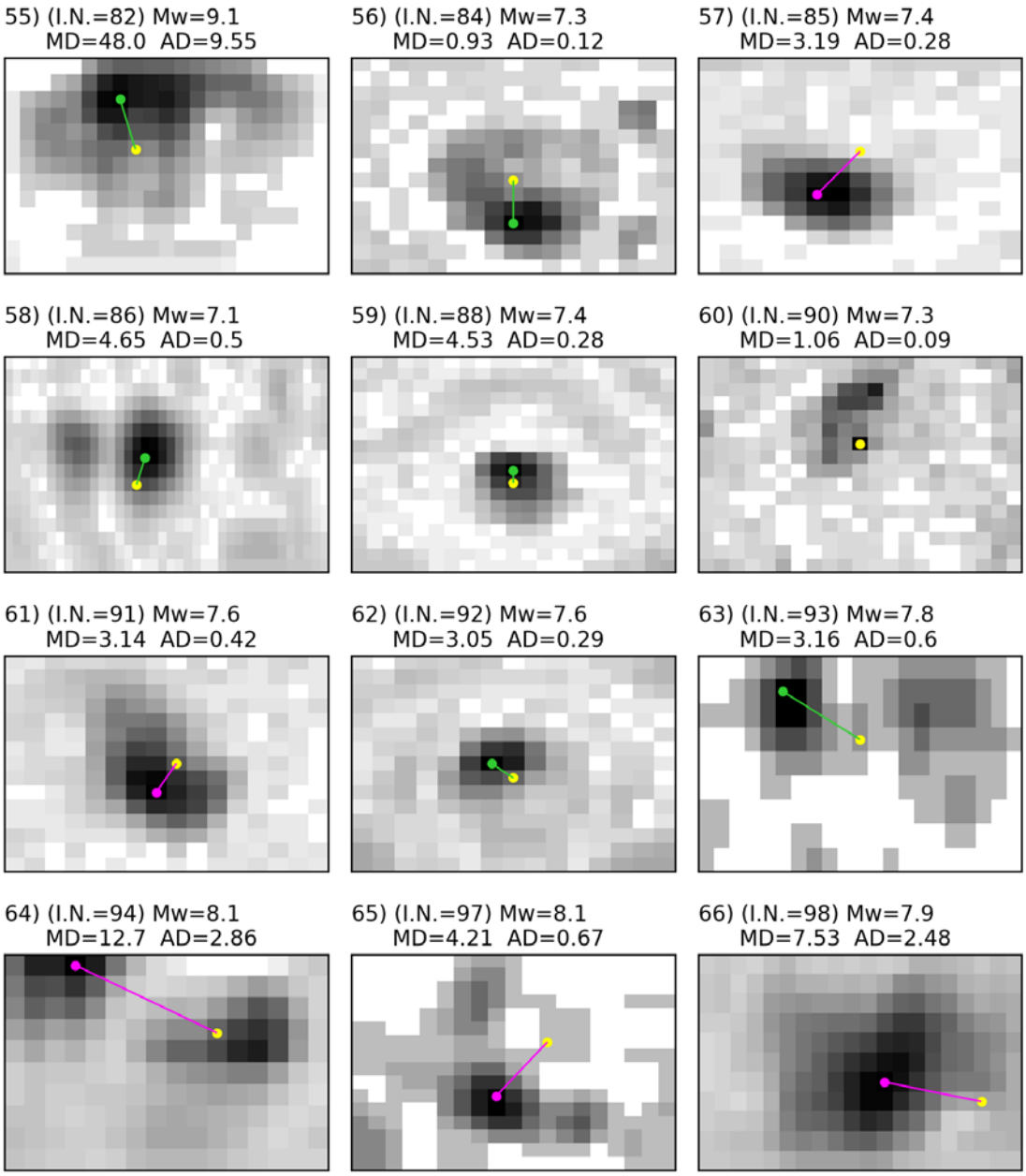

Figure 4.7: Sixth and last set of RFFM images for aspect-ratio class 1

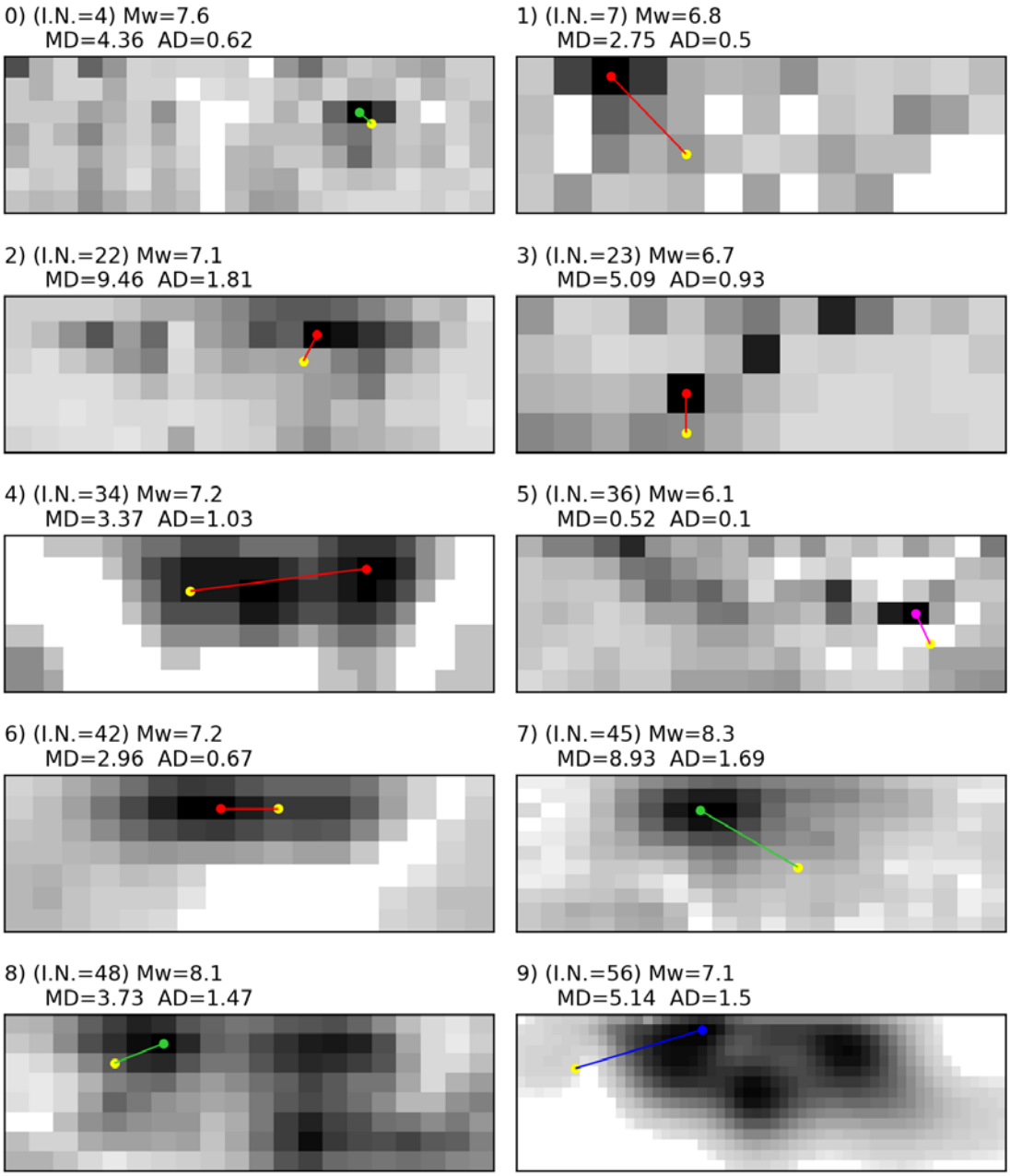

Figure 4.8: First set of RFFM images for aspect-ratio class 2

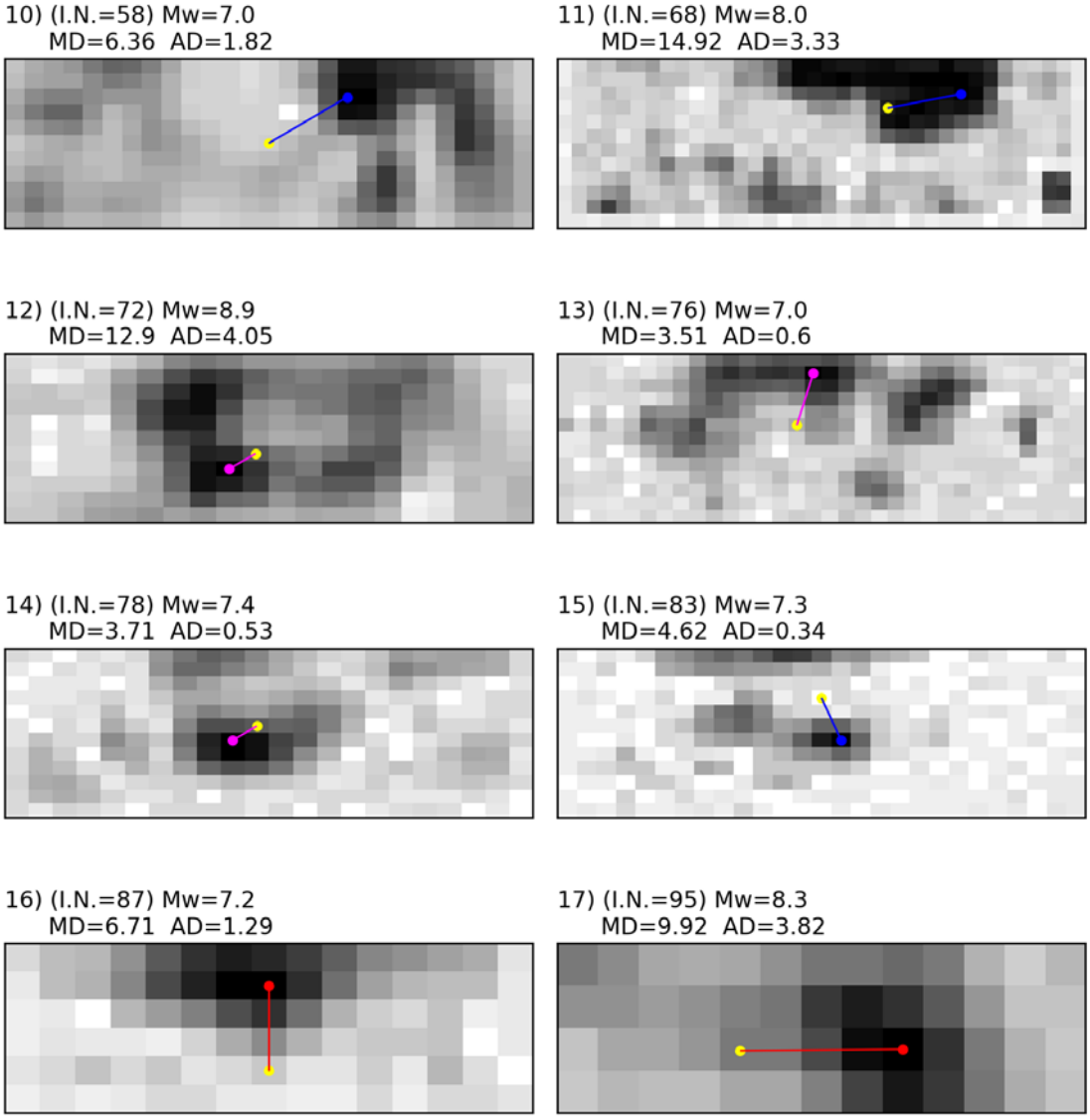

Figure 4.9: Second and last set of RFFM images for aspect-ratio class 2

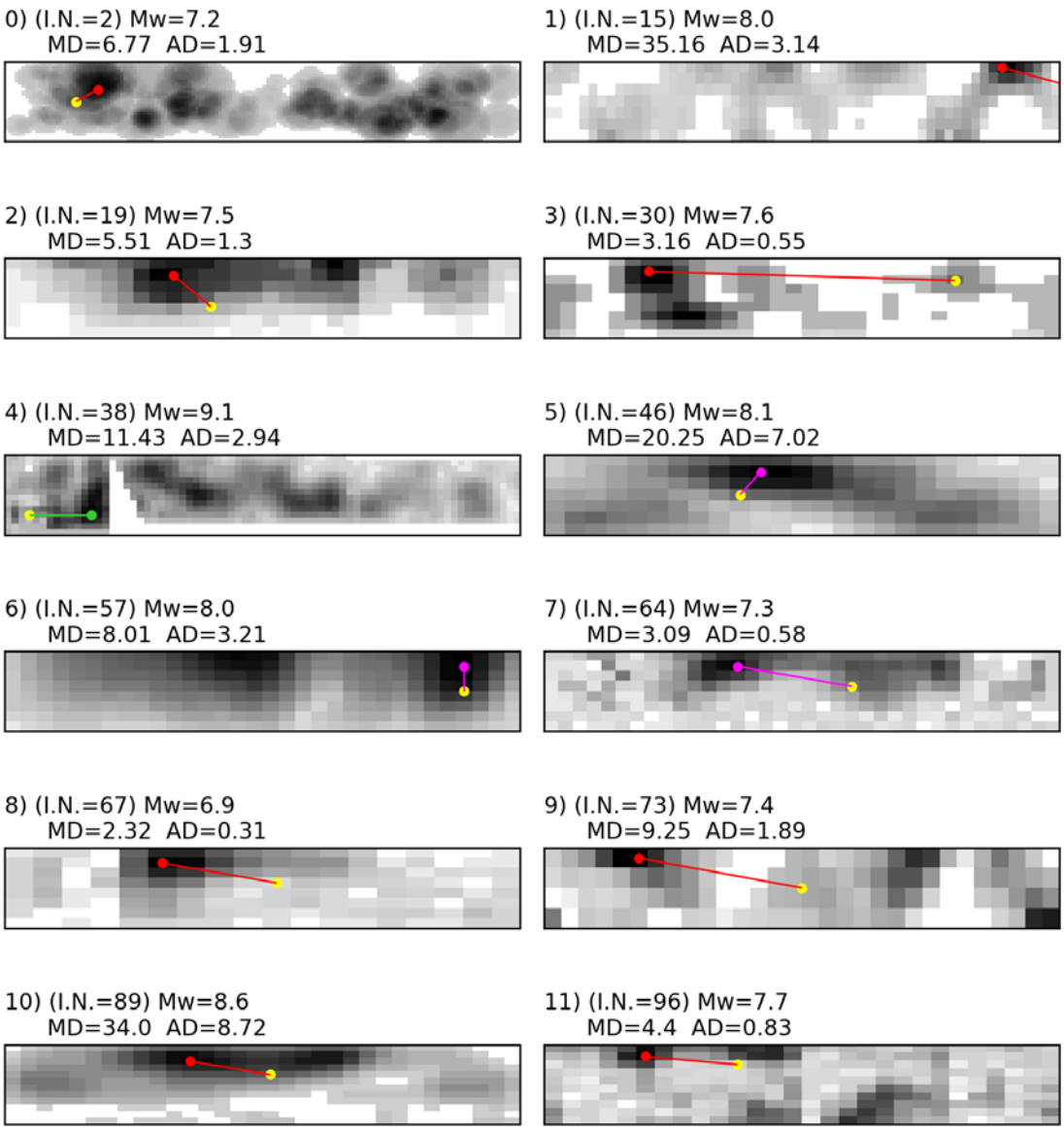

Figure 4.10: RFFM images for aspect-ratio class 3

Even though the RFFM images do not permit to have an immediate idea of the real dimensions of the faults, they can highlight intuitively and immediately some possible regularities or common patterns of different earthquakes of the same class or of different classes, with different focal mechanisms. Looking at the RFFM pictures it is possible to notice some, although qualitative, facts.

The nucleation point is not at all coincident with the maximum displacement point. And, anyway, the two points are never coincident for strike-slip earthquakes. These events exhibit actually the largest distance between hypocentre and maximum displacement.

One can further notice that the hypocentre often lies on the edge of a significant asperity. This holds for all classes. In the first class, 49 over 67 events have the hypocentre very close to the slip peak or to the most relevant asperity. Many of these events, characterized by a low aspect ratio, have a single asperity, that is often found to be located at some distance from the fault-pane centre. Indeed, the rupture evolution of the earthquake is influenced by several factors, which may include the geological composition of the crust, the presence of fluids, etc., and therefore rupture propagation is far from being an isotropic process nucleating from a central source.

In the second class, where several events show the existence of more than one asperity on the fault plane, for 14 over 18 events the hypocentre is found near the edge of an asperity. This holds also for the third class, characterized by a large aspect ratio: here, the cases of a hypocentre close to a significant asperity are 8 over 12.

A further important observation is that the hypocentre is almost always deeper than the peak of slip. For only 23 cases over 98 the opposite is true.

Regarding the horizontal distance, no clear pattern of the relative orientation of the vector joining maximum slip and hypocentre can be identified by simple inspection. For a better insight, we plotted all together, in the same standard fault (one for each class) the above mentioned vector (*Figure 4.11*).

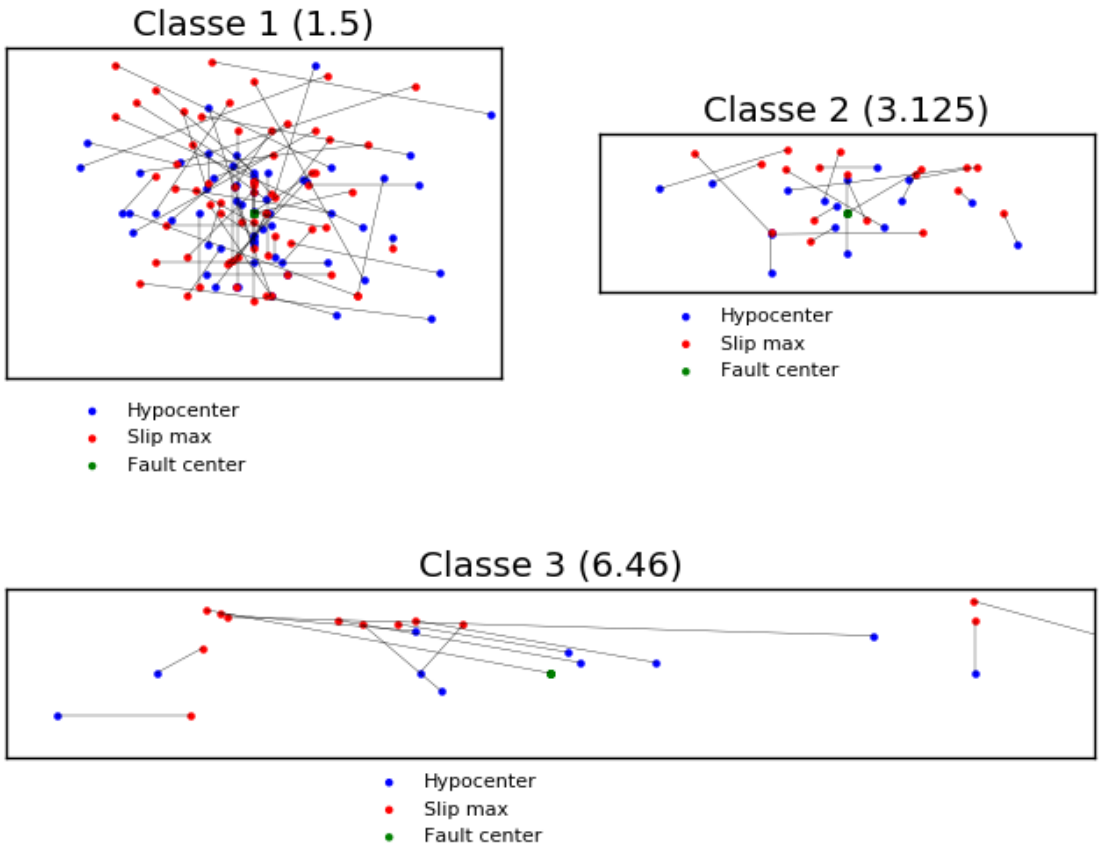

Figure 4.11: Vectors joining hypocentres (blue points) with maximum displacement positions (red points) displayed on the characteristic class fault

From *Figure 4.11* we deduce that the number of hypocentres falling in the right side and on the left side of fault plane is almost equal for all classes, which suggests a left/right symmetry. This allowed us to create a new dataset of RFFMs by moving the hypocentres of all events to the left half of the fault plane: this is simply achieved by letting unchanged all the RFFMs having the hypocentres on the left side and by mirroring all the others with respect to a vertical line passing through the fault centre.

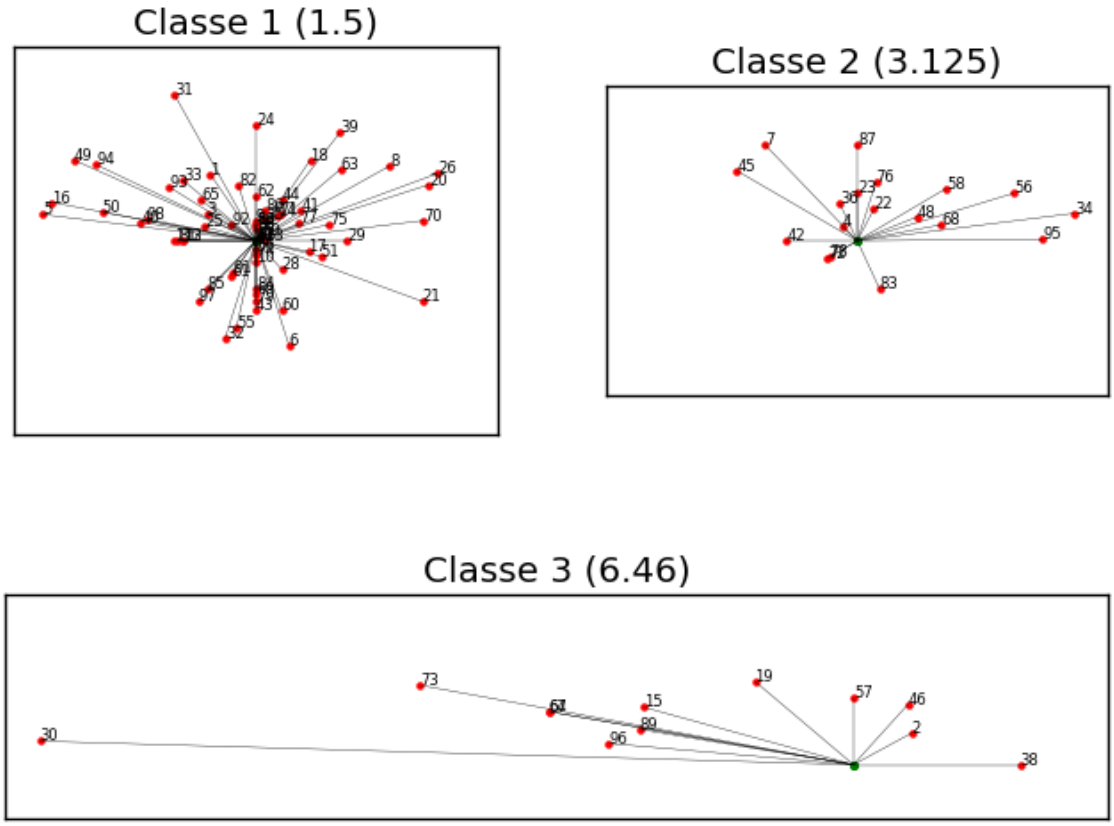

Figure 4.12: Hypocentre-max slip vectors for the RFFMs, drawn from a common (hypocentre) origin. Distances and angles were left unchanged.

From *Figure 4.12* and *Figure 4.13* one can easily confirm what was mentioned previously: that the hypocentre is mainly deeper than the maximum displacement. Few are the cases that exhibit the opposite behaviour, and only in the first and second class.

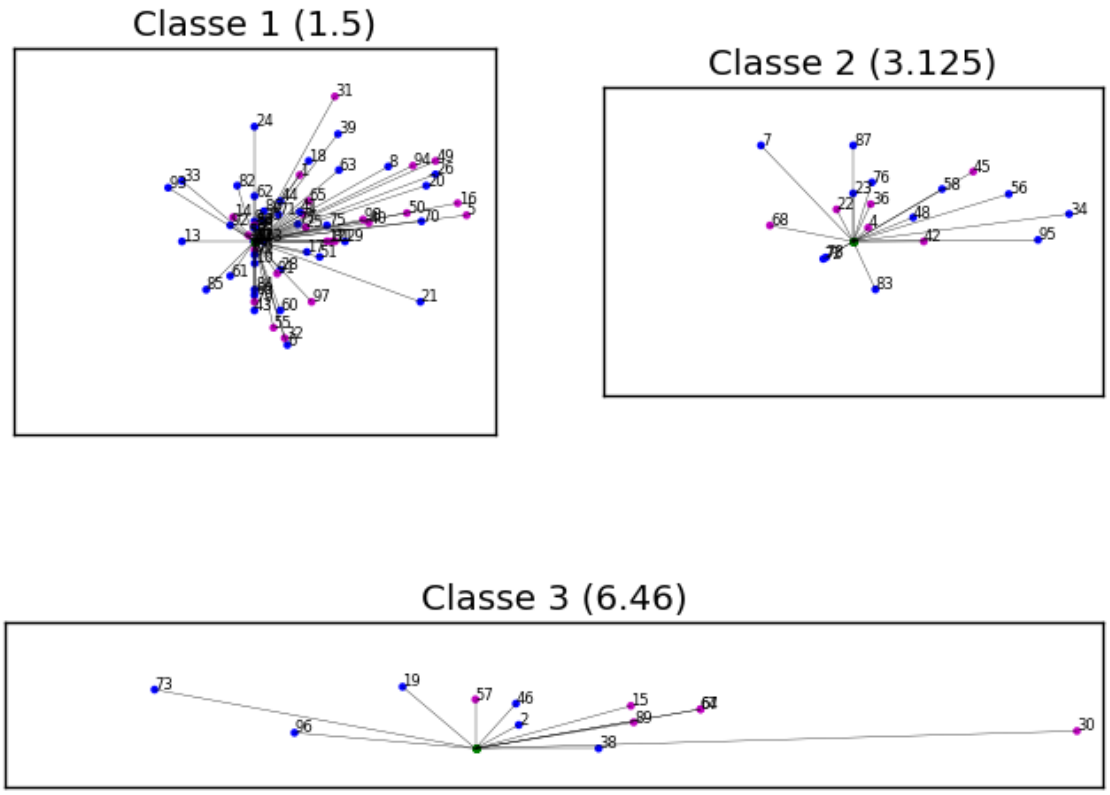

Figure 4.13: The same as Figure 4.12, but referred to the set of mirrored RFFMs. Blue points refer to unchanged models, magenta points to the mirrored models.

4.2.1 Position of the slip peak

Looking at the images in *Figure 4.2-Figure 4.10* it is noticeable that the peak of slip is more often off to the side than in the fault centre. Only 18 events of class 1 and 2 events of the class 2 have the peak at the centre of the fault. It is possible, also, to note a sort of positive correlation between the distance of the maximum displacement from the fault centre and the magnitude; and this growth seems to be larger, with the same magnitude, for the strike-slip earthquakes.

For this reason, this possible correlation was studied more carefully with a linear regression. *Figure 4.14* shows a good level of correlation between the distance and the magnitude: and the distance is effectively markedly larger for strike-slip events. The normal earthquakes are, instead, the ones having the stronger growth.

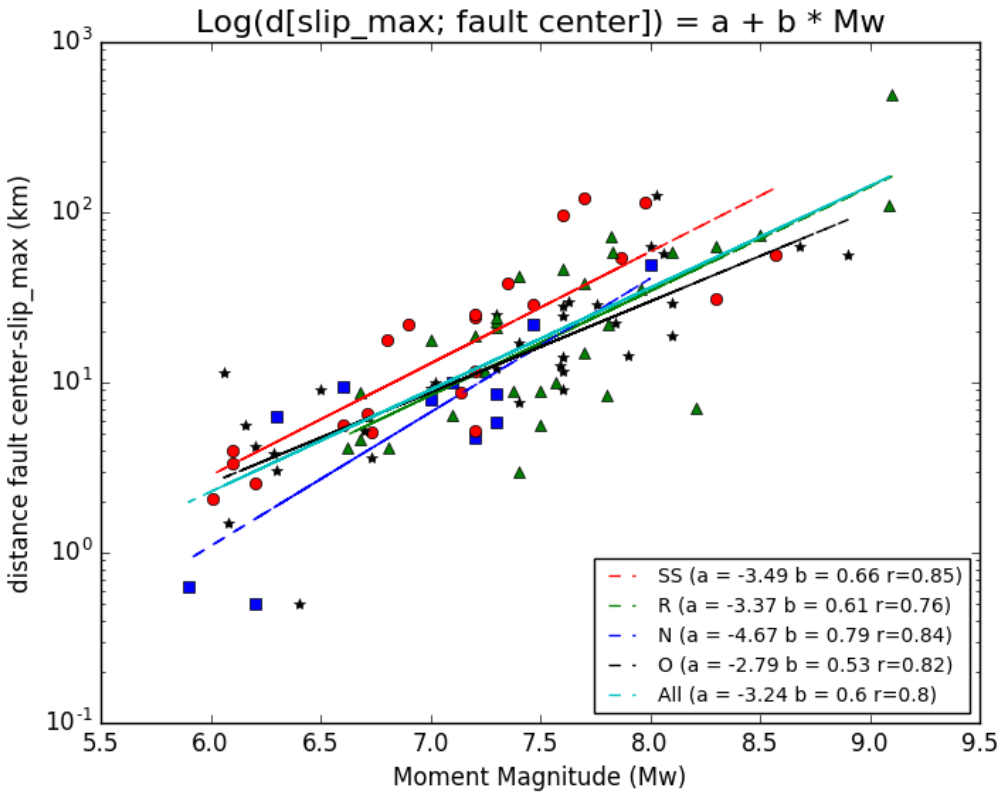

Figure 4.14: Linear regression between the logarithm of the distance between the point of maximum displacement and the fault center vs. Magnitude

The question may arise whether this correlation is attributable to the horizontal or to the vertical components of distance vector or to both. To better answer this question, the single components (along-strike and down-dip) have been plotted vs. magnitude. From *Figure 4.15* one can observe that the correlation between vertical component and magnitude is higher than the one involving the horizontal component for strike-slip and oblique events. Normal events present the best correlation (r = 0.9) for the horizontal component regression and the strongest growth with the increase of the magnitude.

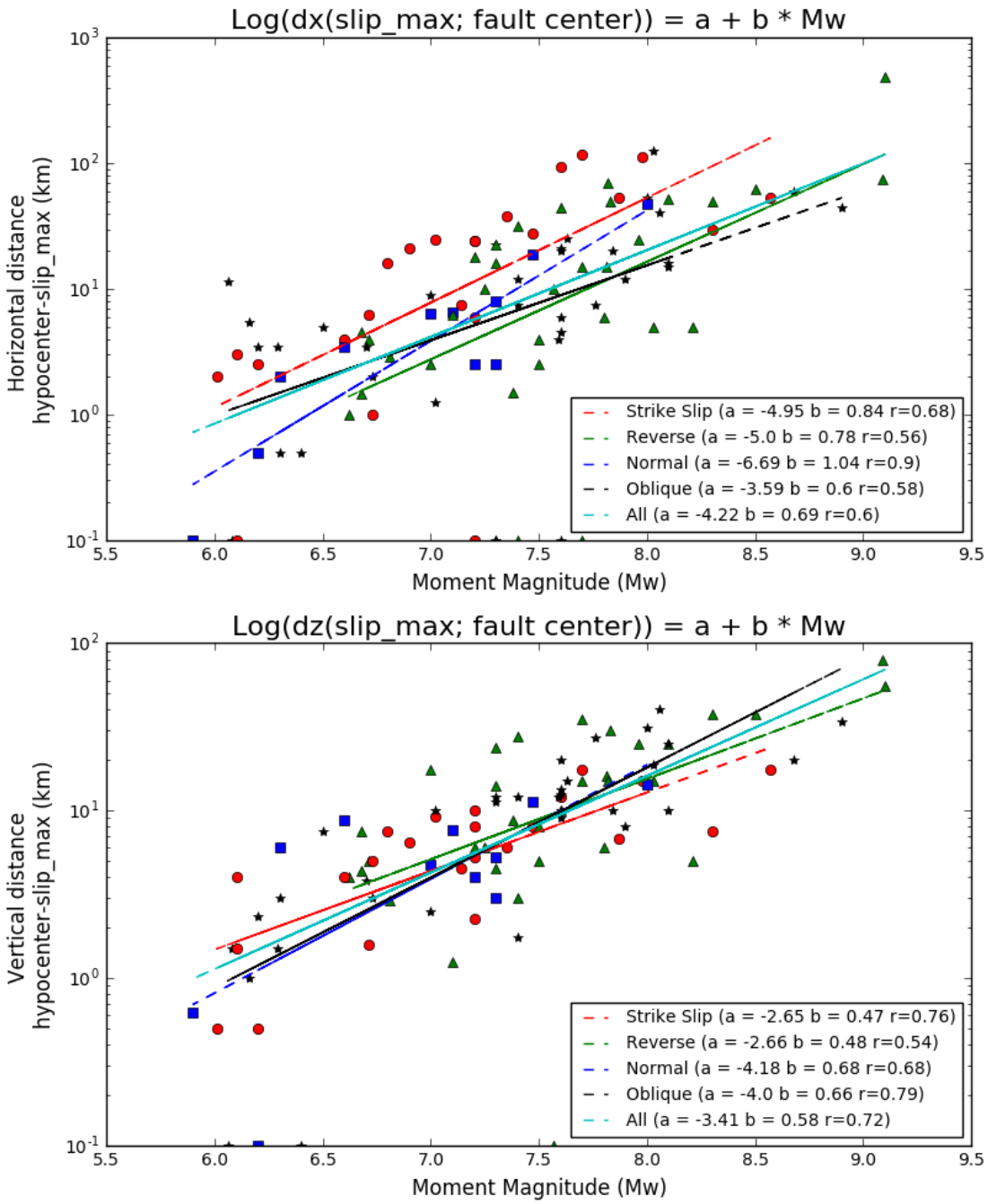

Figure 4.15: Regressions of along-strike (top) and down-dip (bottom) components of the distance slip_max-fault center vs. magnitude

4.3 Conclusions

From the above analysis one can draw some interesting considerations, synthesised in the following.

The hypocentre position rarely coincides with the peak of slip, and often lies at larger depth.

The hypocentre is almost always found near an asperity: in case of low aspect-ratio RFFMs, it is highly likely that this asperity is the one containing the slip peak.

Regarding the position of the peak of slip, this generally lies far from the fault centre, with distance increasing with the earthquake magnitude, and more quickly for normal events.

5 Chapter 4

In this chapter we focus our attention on the distribution of slip over the fault. The goal is to find possible regularities or characteristic configurations in the set of the RFFMs.

Having in mind tsunami generation by earthquakes, it is once more pointed out that the slip distribution on the fault plane influences decisively the geographical pattern of the maximum heights of the tsunami waves on the coast. Getting regressions allowing one to derive reliable on-fault distributions of slip from the earthquake magnitude would ensure improvements in the estimates of tsunami hazard, especially in areas such as the Mediterranean, where the tsunamigenic sources are often located a few kilometres or a few tens of kilometres away from the coast. In addition to this, it is manifest that a better knowledge of the coseismic slip distribution could improve the so-called "decision support chain" as part of the tsunami early warning systems.

A relevant problem for the tsunami warning centres, particularly for those, like in the Mediterranean, where the tsunami leading time is short, is that the decision whether issuing or not an alert after a potentially tsunamigenic earthquake, has to be made, in real-time operations, with a lack of relevant information on the earthquake source. However, focal mechanism is one of the main discriminants concerning the earthquake's ability in the generation of tsunami waves. Nowadays, information on focal mechanism is available relatively late (some tens of minutes), because it is based on the inversion of seismic data. Other data, in particular geodetic data, are perhaps more suitable to obtain a rough estimate of the earthquake focal mechanism in shorter times (3-4 minutes), but their availability and utilisation is limited by the GPS networks that do not have a global coverage and by the tsunami warning centres operational procedures that are mainly focused on seismic data.

Possible relations and useful patterns emerging from the line of research that is started by the present study could potentially lead to an immediate, and more accurate estimate of the distribution of slip based on earthquake magnitude and focal mechanism, and in turn to improve the performance of the tsunami warning centres alert procedures, especially for what regards the near field.

5.1 Limits of the finite-fault inversion

As already mentioned in previous chapters, this study deals with finite-fault models derived from finite-fault inversions. The inversion matrix of seismic data for slip distribution on finite faults is based on the formulation of the representation theorem as a linear inverse problem (Beresnev, 2003).

In view of the approach and the parameterization involved, the resolution technique implies a certain degree of subjectivity, which is a source of uncertainties. To obtain meaningful solutions, the inverse problem requires to be numerically stabilized and geologically constrained. Even if this has been well faced, significant uncertainties still derive from the seismic parameterization.

In addition to the above factors, the choice of using linear inverse-problem resolution techniques requires that only one variable (the final slip values on the subfaults) has to be determined with others, like the slip duration, being fixed a priori in the procedure.

Furthermore, in the inverse resolution process continuous integrals are computed numerically, which implies that results depend on gridding. For the present FFM dataset the smallest subfault size is of 0.5 km. It is also known, however, that the stability of the inverse problem decreases with the growth of the grid size. It is worth stressing here that the greatest limitation of slip inversions is that, at the end, they belong to the wider category of inverse geophysical problems that are known to admit no unique solution, unless a priori knowledge is injected in the procedure.

5.2 Some basic statistics

This section shows some significant statistics of the slip distribution of the FFMs.

Figure 5.1 shows how the slip is distributed over the fault compared to the fault area. The four histograms show the distribution of the area percentage with values of slip larger than a given fraction of the maximum displacement (MD): ¼ of MD (“considerable slip” values) for the histogram at the top-left, ½ of MD (“very considerable” values) for the histogram at the top-right, ¾ of MD (“large slip” values) for the histogram at the bottom-left, and 9/10 of MD (“very large slip” values) for the histogram at the bottom-right. Considering the first one, half of the FFMs have a percentage of area containing “considerable slip” lower than the 30%; 15 events present

areas of “considerable slip” larger than the half of the fault plane, and 2 events even larger than 90% of the total fault area.

Passing to the second histogram, no events present a “very considerable” slip area larger than half of the fault plane, and the average value of this regions is 13.7% of the total area.

For the regions of “large slip” the maximum percentage is less than 20% of the total area, and less than half of FFMs present values larger than 5%.

Finally “very large slip” regions are, on average, only about 1.9% of the total area, and only one event presents a percentage between 8.5% and 9%.

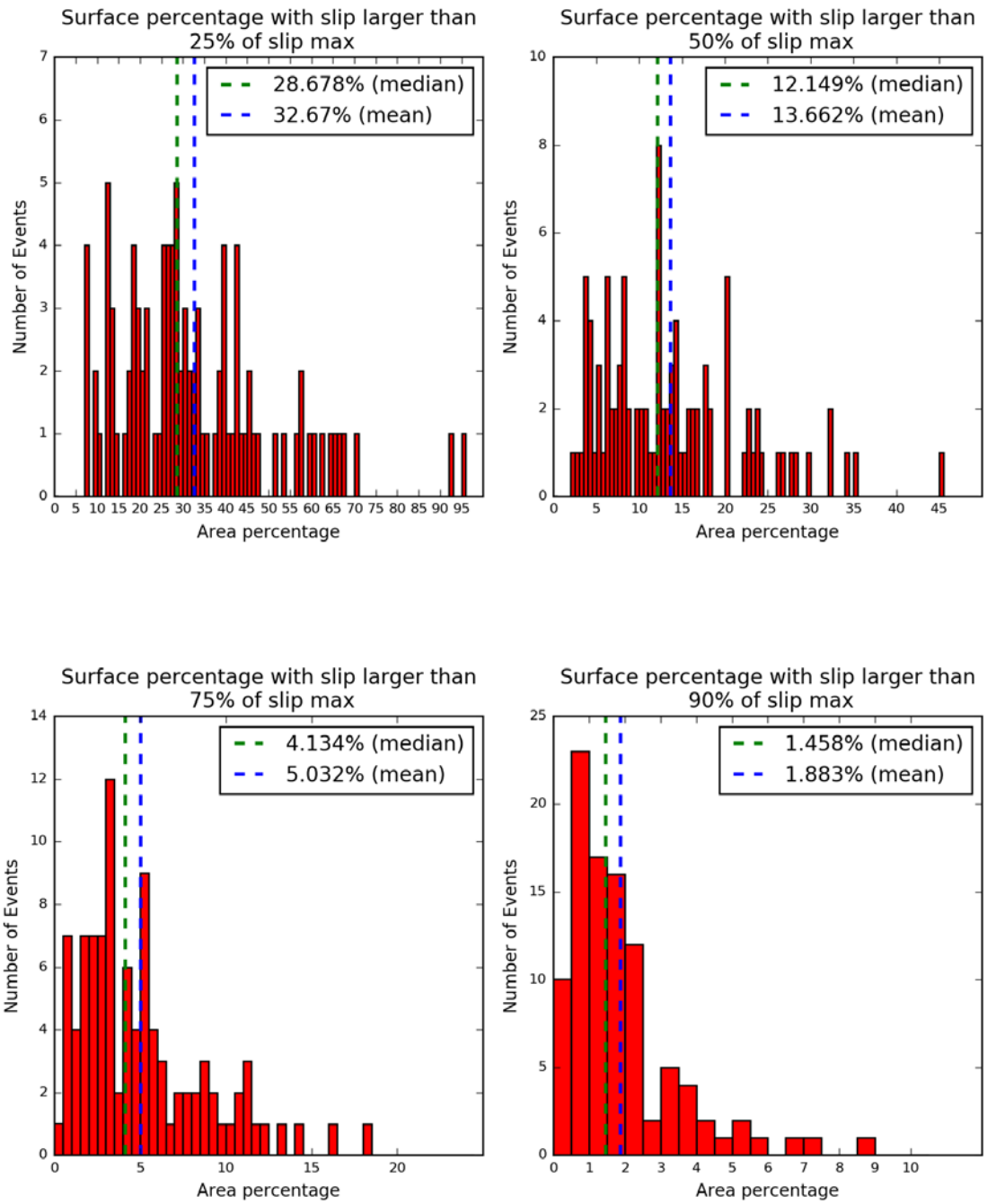

Figure 5.1: Frequency of FFMs with a percentage of fault area covered by slip values larger than 0.25 MD (top-left), 0.50 MD (top-right), 0.75 (bottom-left), 0.90 MD (bottom-right), where MD is the Maximum Displacement.

Figure 5.2 shows the slip distribution for the three aspect-ratio classes, of the Maximum Displacement (MD, red bars, right side) and of the Average Displacement (AD, light blue bars, right side) of the original FFMs.

It is evident to notice that both MD and AD distributions increase their mean values passing from Class 1 to Class 2, and from Class 2 to Class 3.

With the exception of one event (I.N. 82, Tohoku Japan 11/03/2011) with MD ≈ 50 m, and five events with 10 m ≤ MD ≤ 25 m, the first aspect-ratio class has MD values lower than 10 m for 62 over 67 events.

The second class presents the highest AD/MD ratio. Compared to the first class, it has larger regions of high slip, which are suggestive of more than one asperity. Compared to the third class, it shows a smaller extension over which the slip can be distributed, leading to a larger ratio of the mean slip over the max slip.

Regarding the third class, MD and AD values are more than double of the values of the total events.

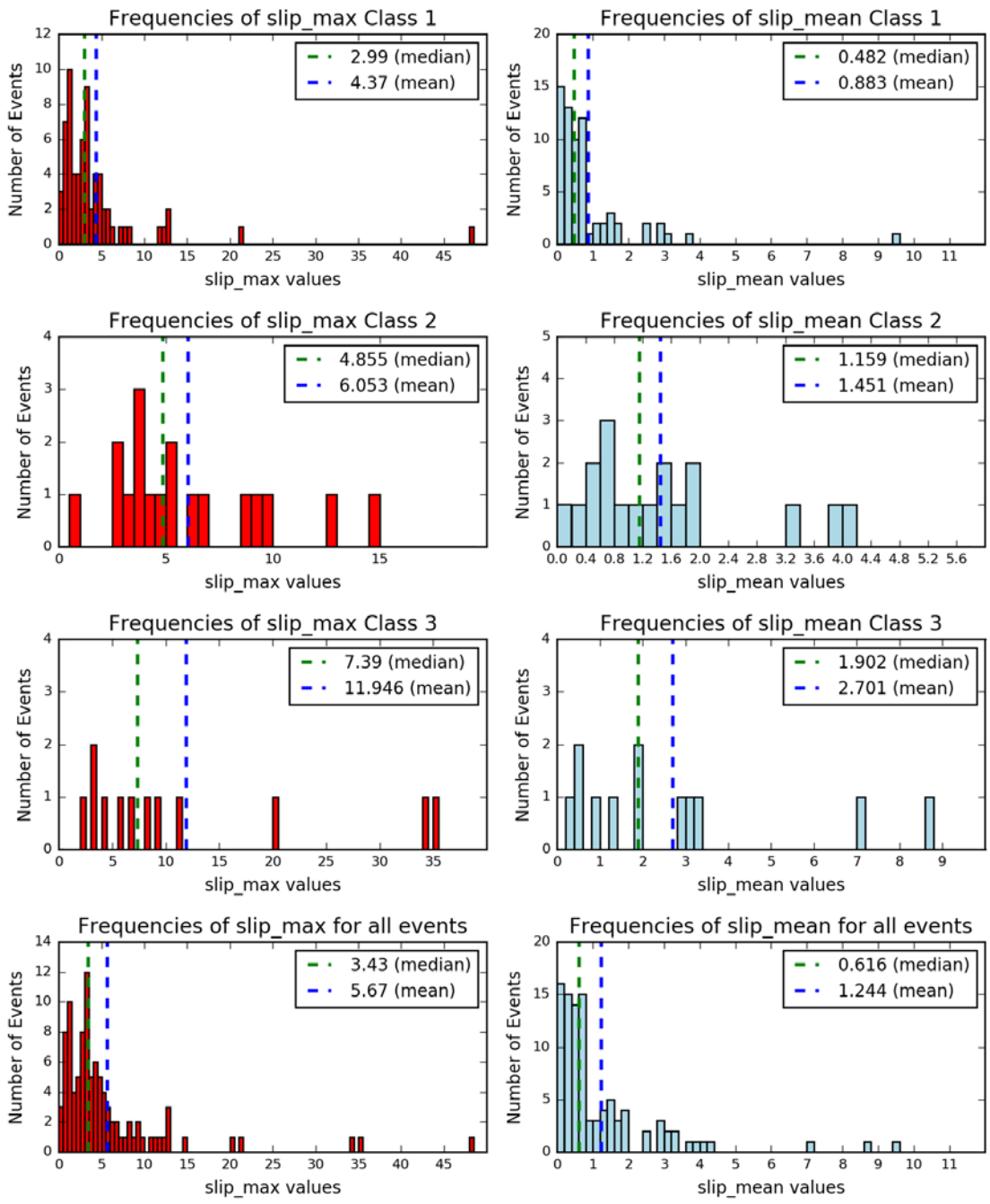

Figure 5.2: Frequency for each aspect-ratio class and for the total, of the slip max (red) and the slip mean (light blue).

5.3 Choice of the standard grids

The FFMs were derived from different data sources (geodetic, teleseismic, inSAR, local P waves, or combination of some of them), and calculated following different inversions techniques.

In order to make the inter-comparison easier the FFMs were bilinearly interpolated into common grids, one for each aspect ratio class. To help select the appropriate grid size for each class, the distribution of Nx and Nz (number of subfaults along strike and down-dip directions, respectively) for our FFM dataset has been studied. In *Figure 5.3* displays from the top to the bottom, the distribution for classes 1, 2, and 3, and for the total set of FFMs: Nx on the left side, Nz on the right. Based on these graphs, a standard grid has been established for each class. For class 1 we opted for nx = 15 and nz = 10, values slightly smaller than the average but perfectly in proportion with the reference aspect ratio (1.5).

For class 2 and class 3 the distributions of subfault dimensions do not agree so well with the respective reference aspect ratios. Hence for both of them we opted for the median values: (20,8) for the second class and (32,8) for the third class.

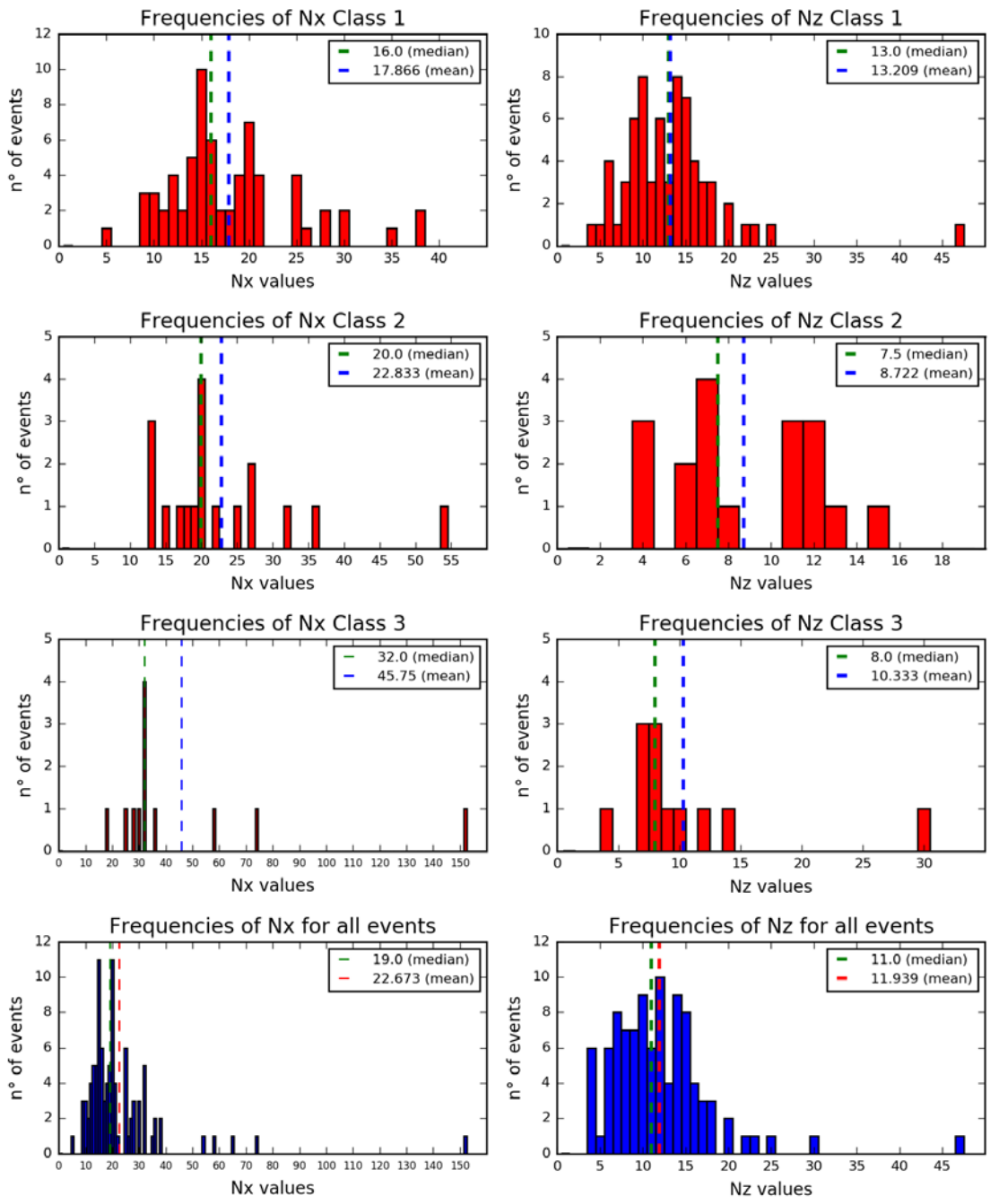

Figure 5.3: Bar charts showing the distribution of Nx (left) and Nz (right), for every class (red) and for all the events together (blue.

Once established the standard grids, we proceeded as explained in the following:

- for all FFMs presenting the horizontal coordinate of the hypocentre larger than the central one (i.e. with the original hypocentre on the right side), the fault plane has been rotated by 180 degrees around a central vertical axis;

- every slip matrix has been normalized with respect to its maximum values, in order to have all events with a peak of 1.0;
- The FFM have been kriging interpolated over grids with standard dimensions (10 x 15 for the first class, 20 x 8 for the second class, 32 x 8 for the third class).

Since kriging, though leaving the slip distribution patterns almost unchanged, modifies the value of maximum and mean displacement, as final step, we further divided each element of the new matrix for the "new maximum" value in order to regain a matrix with a peak value of 1.0.

The new model is here called the rescaled FFM and often denoted RFFM.

We recall here that in chapter 3 all images of the RFFMs are displayed distinctly for aspect-ratio classes.

5.4 Similarity matrices

Once obtained a common representation criterion for the slip distribution over the fault plane of the same aspect-ratio class, it is necessary to establish the way through which compare the models between each other.

The first choice was to create, for each class, three matrices of similarity. The construction of the matrixes has been done in the same way for all the classes according to the following procedure.

Considering a class of N events, the final similarity matrices will be square (N x N) matrices. The (n,m) element of the matrix represents the coefficient of similarity between the n-th the m-th events. For the first matrix (called DELTA matrix), the choice of the similarity coefficient was:

$$C_{DELTA} = 1 - \frac{\sum_{i,j}|x_{i,j} - y_{i,j}|}{N}$$

where x and y are the RFFM slip values of the cells of the n-th matrix and of the m-th matrix. For the second one (called RMS matrix) the similarity coefficient is based on the root mean square of the squared differences:

$$C_{RMS} = 1 - \sqrt{\frac{\sum_{i,j}|x_{i,j} - y_{i,j}|^2}{N}}$$

In virtue of these definitions, the resulting matrices DELTA and RMS are symmetric with diagonal unit elements. In the following, the DELTA and RMS matrices are graphically represented.

For Class 2 and Class 3 the displayed matrix images have, in the middle of each sub-square, the numbers of the events whose comparison is expressed by that sub-square. For Class 1, because of the higher number of events included, the number are simply reported on the sides of the square images.

The numeric values of the sub-squares could be interpreted from the colour scale on the right of each image.

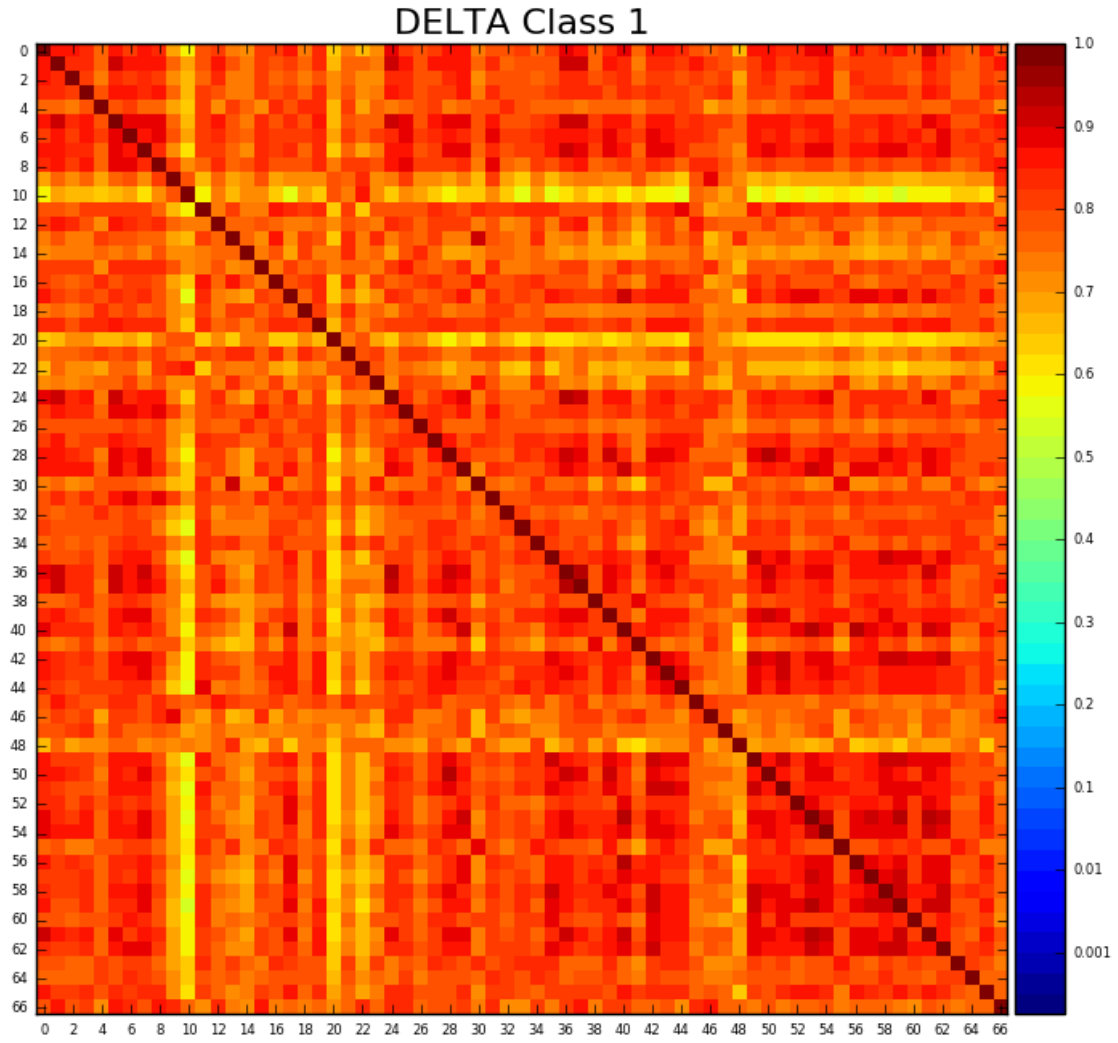

Figure 5.4: Similarity matrix for the events of class 1

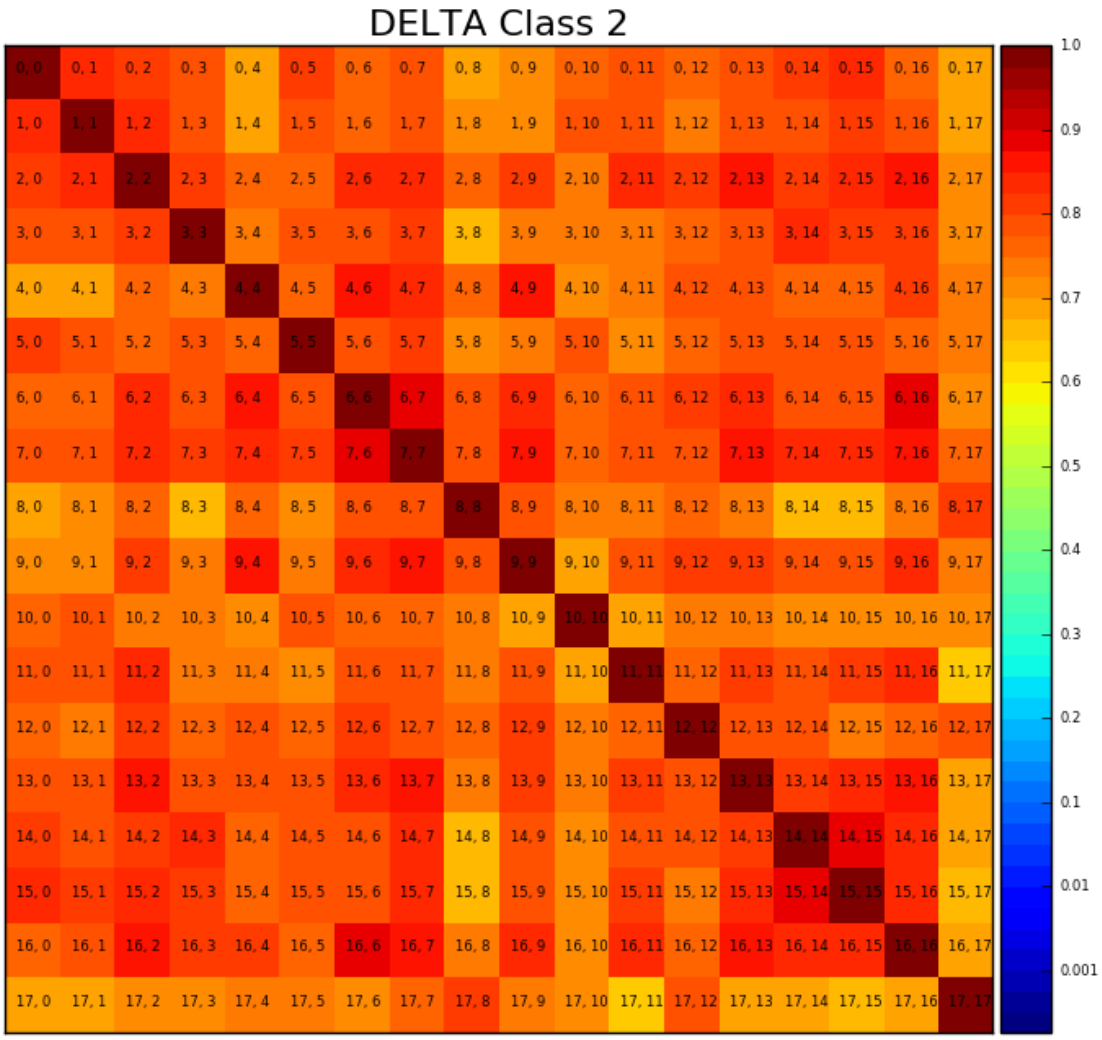

Figure 5.5: Similarity matrix for the events of class 2

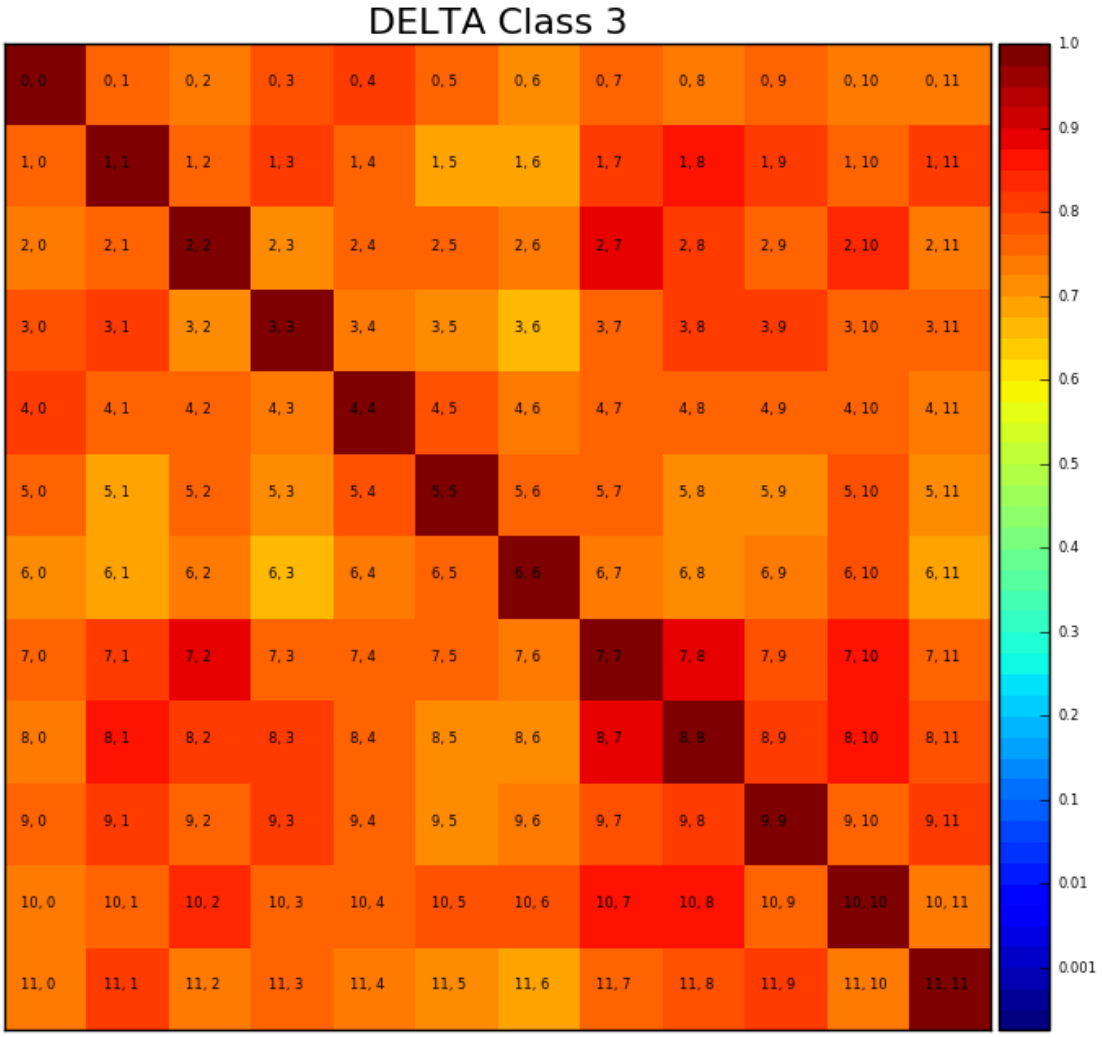

Figure 5.6: Similarity matrix for the events of class 3

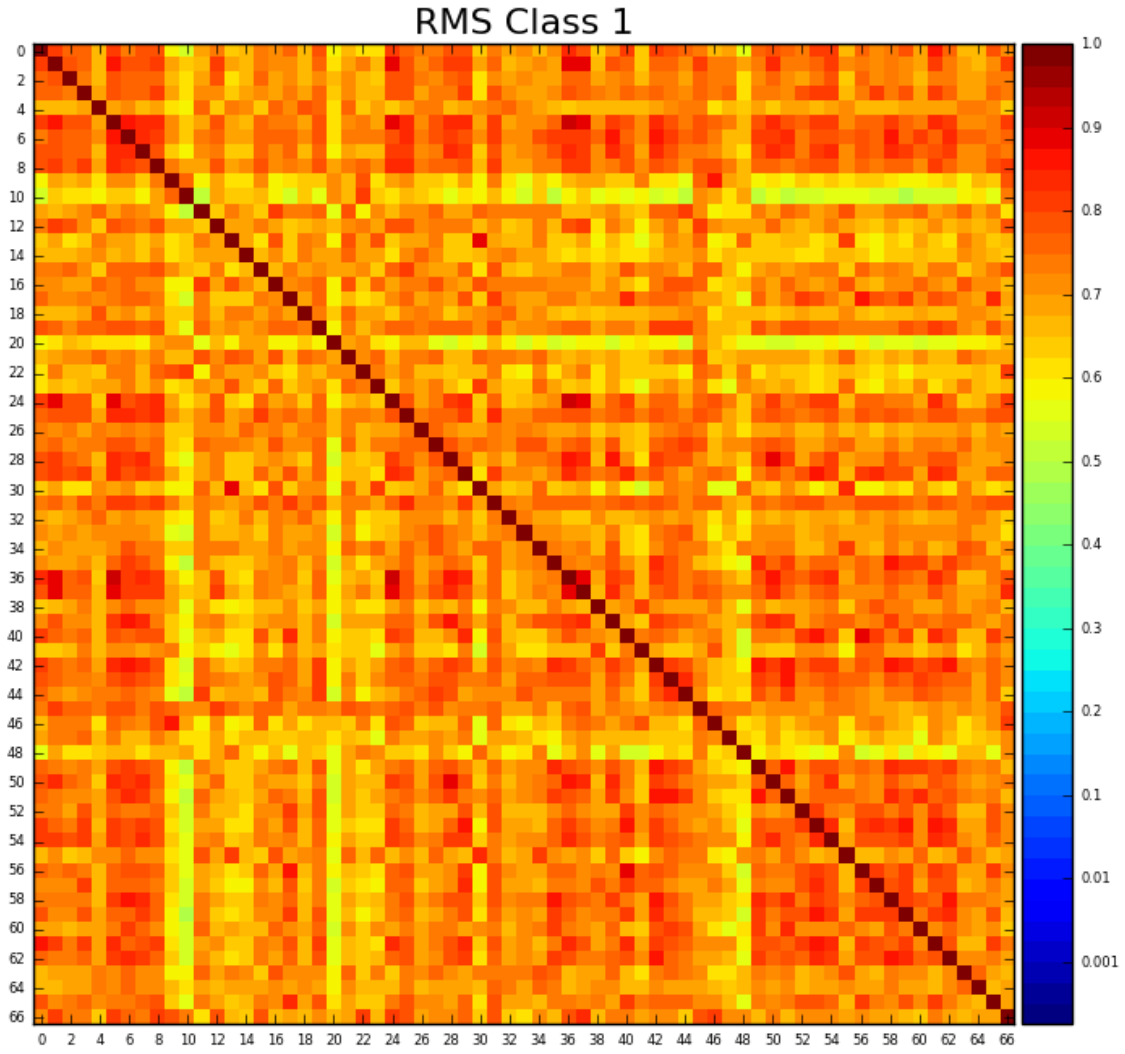

Figure 5.7: RMS similarity matrix for RFFMs of class 1

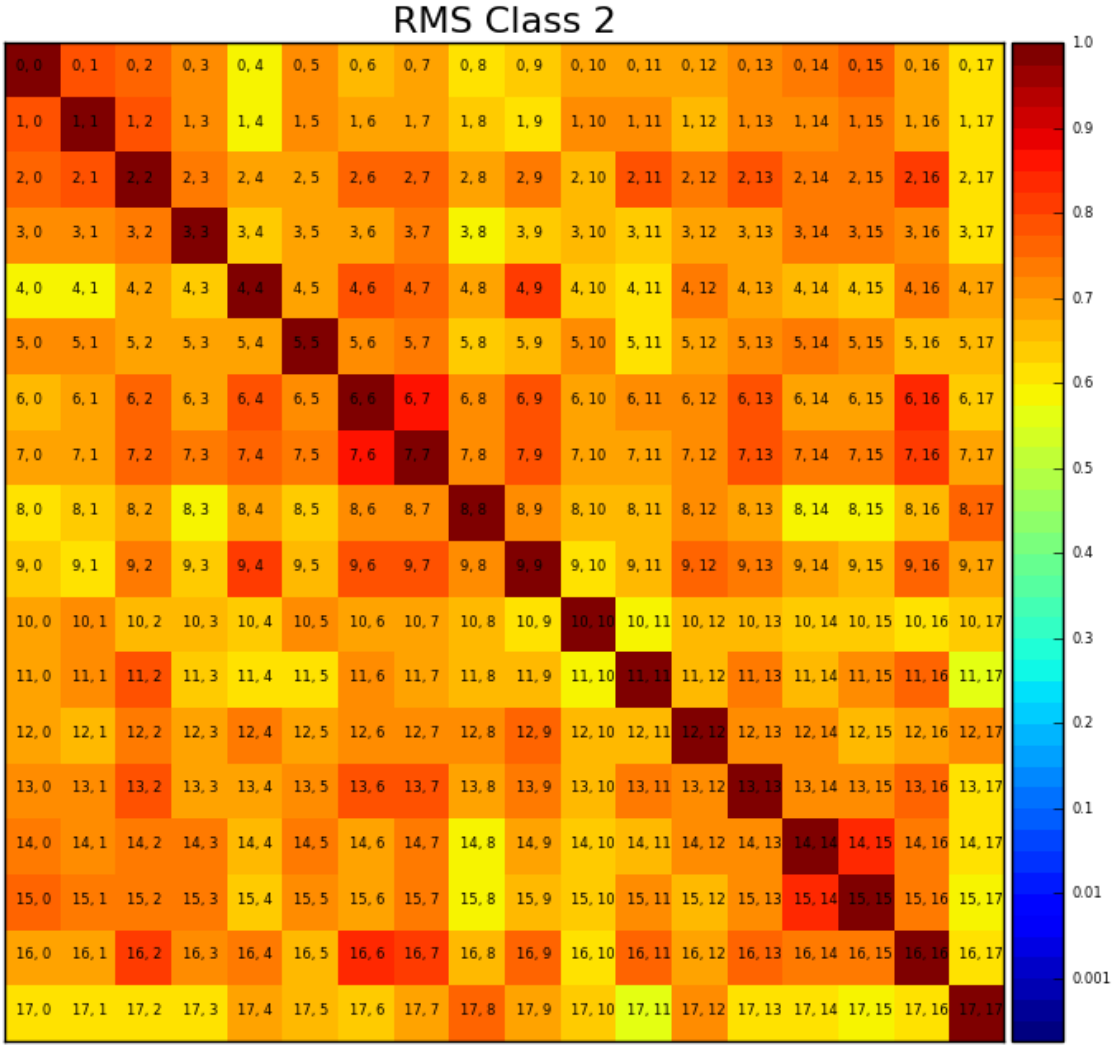

Figure 5.8: RMS similarity matrix for RFFMs of class 2

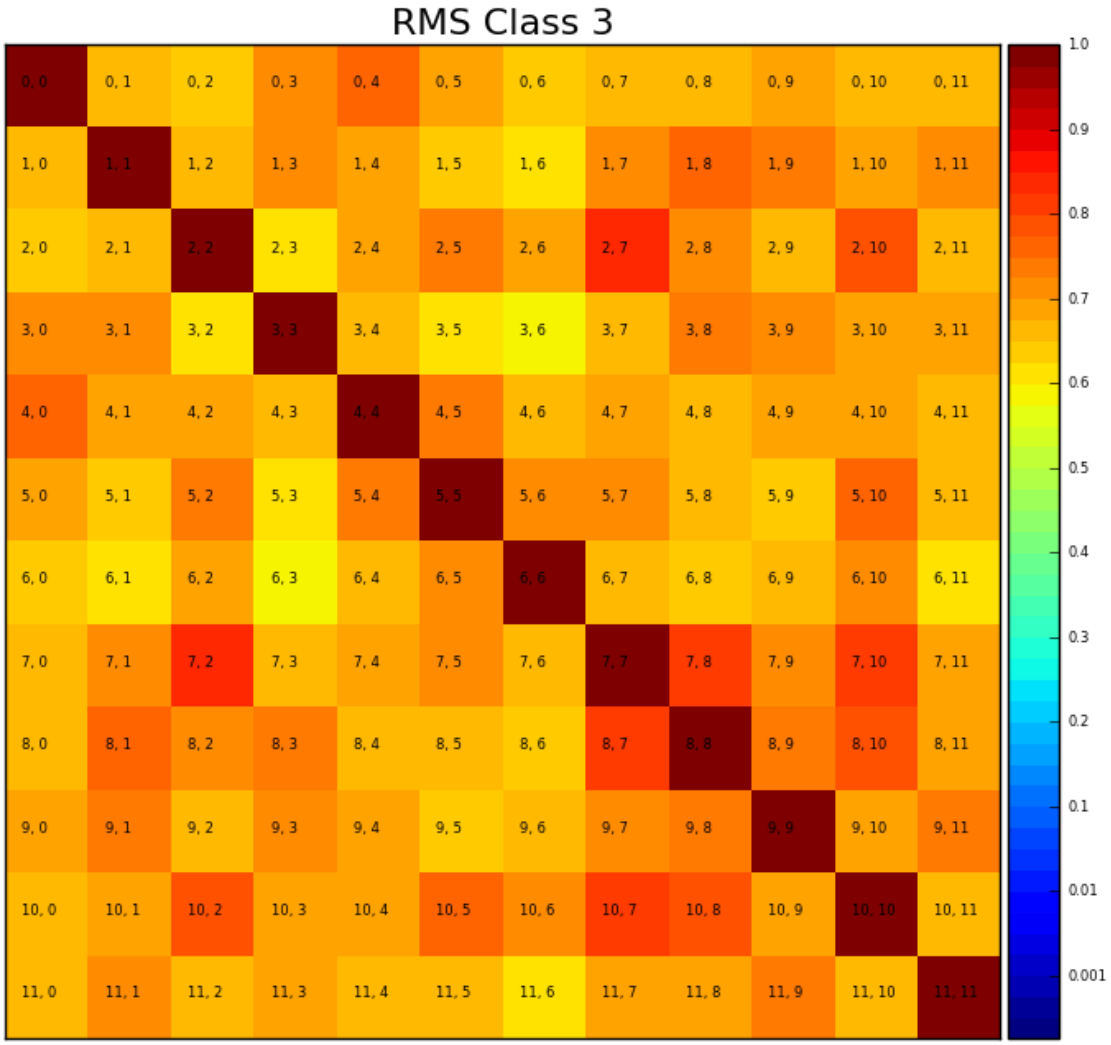

Figure 5.9: RMS similarity matrix for RFFMs of class 3

The DELTA matrices present very high indexes of similarity. Checking some of the RFFM couples with largest indexes, we concluded that C_{DELTA} is not a suitable similarity index for our goal. The reason is that the index is dominated by the differences in areas of small slip values. Since many RFFMs have a high number of subfaults characterized by really small value of slip, these subfaults contribute significantly in decreasing the differences cell by cell, thus improperly increasing the similarity index.

Hence, a new similarity index has been adopted, that is a modified version of C_{DELTA}. The new similarity matrix has been called with the same name, i.e. DELTA matrix and replaces the old one. Since the old one is no longer used, there will be no confusion in

the discussion. The new similarity index was calculated according to the following steps.

- For each RFFM, the slip values (between 0 and 1) have been divided by the sum of all the fault cells, in order to obtain a fault matrix whose elements have a unit sum.
- Once obtained normalized RFFMs, they have been compared by couple. For each couple, the minimum-slip fault has been built by taking the smaller slip value of any cell pairs.
- The similarity index has been calculated as the sum over all the cells of the minimum-slip fault.

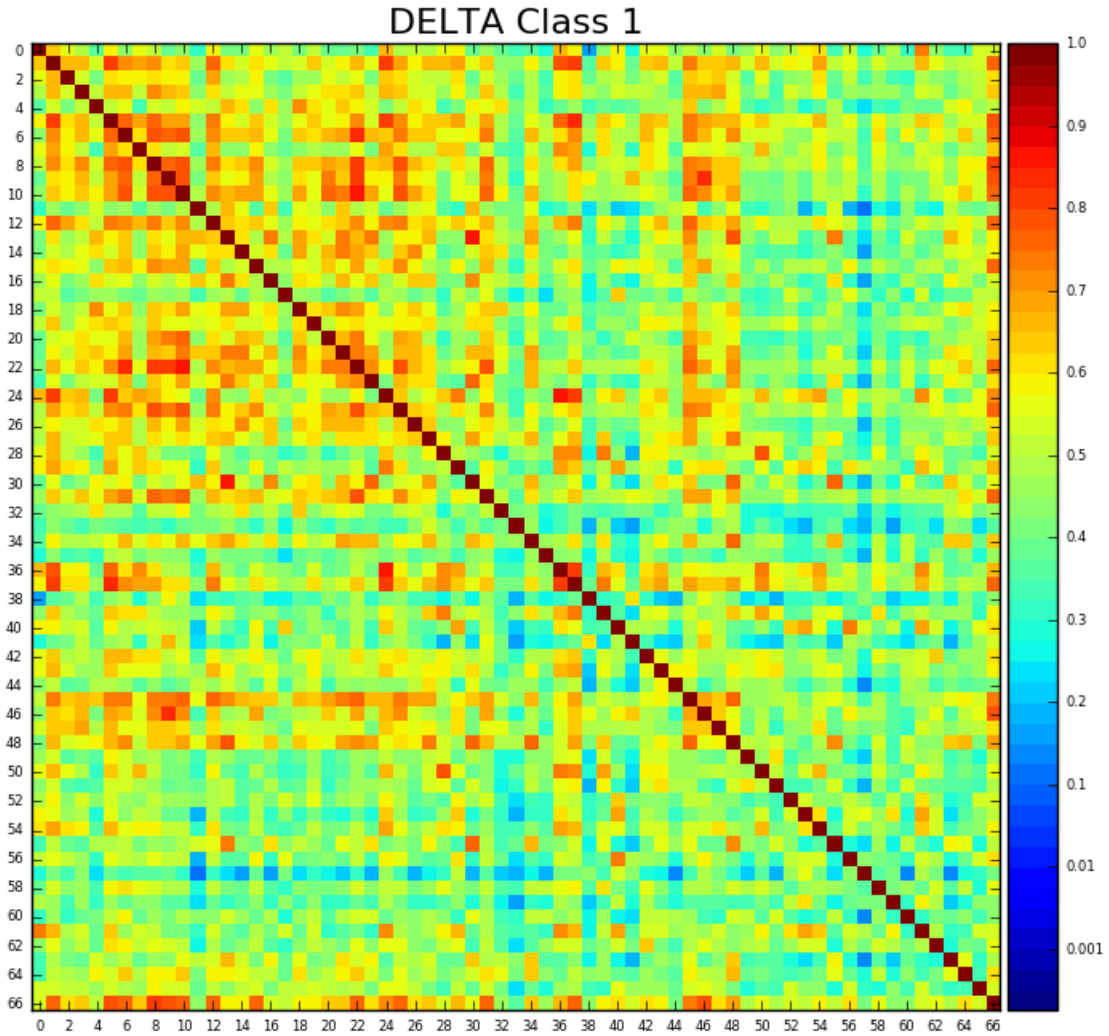

Figure 5.10: New similarity matrix for the RFFMs of class 1

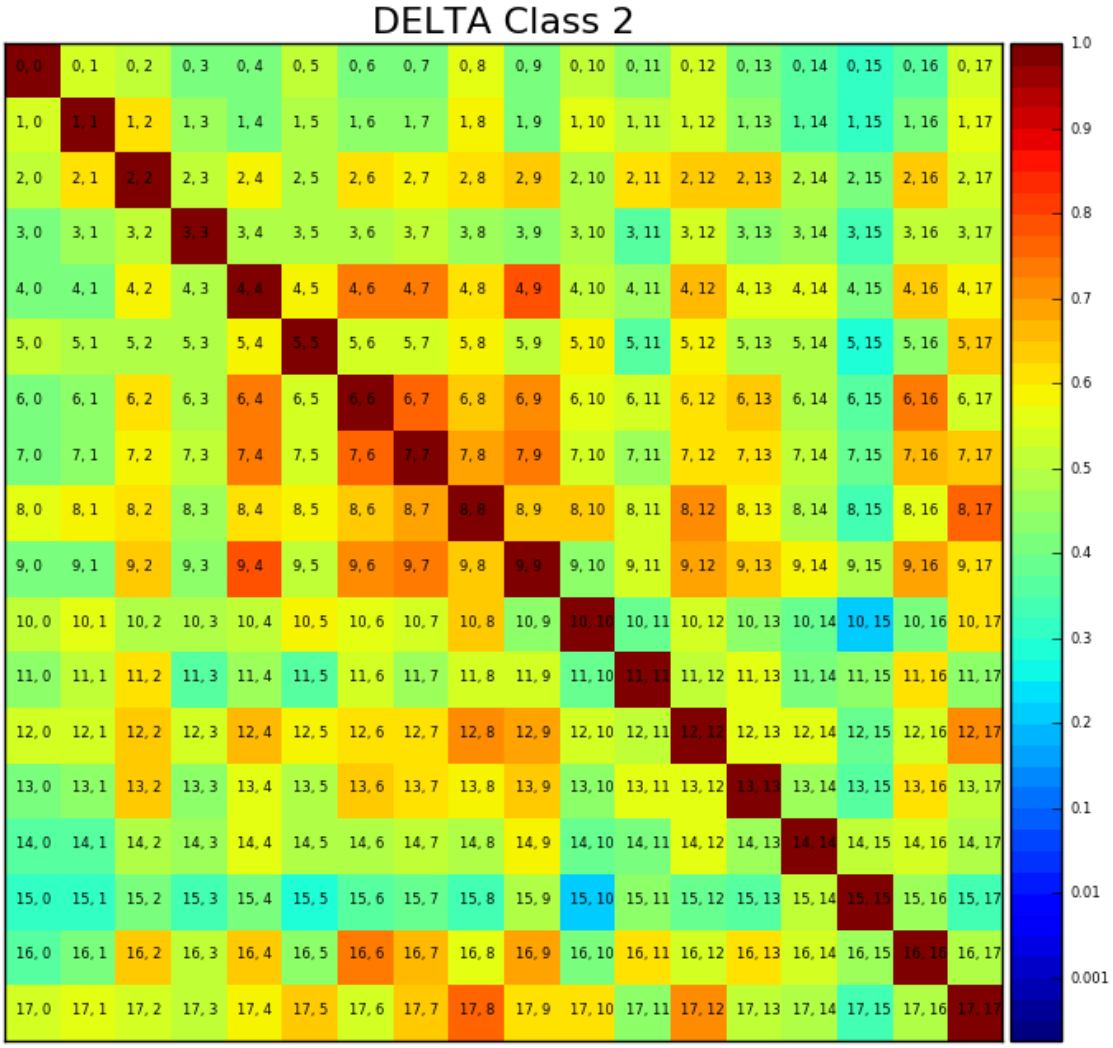

Figure 5.11: New similarity matrix for the RFFMs of class 2

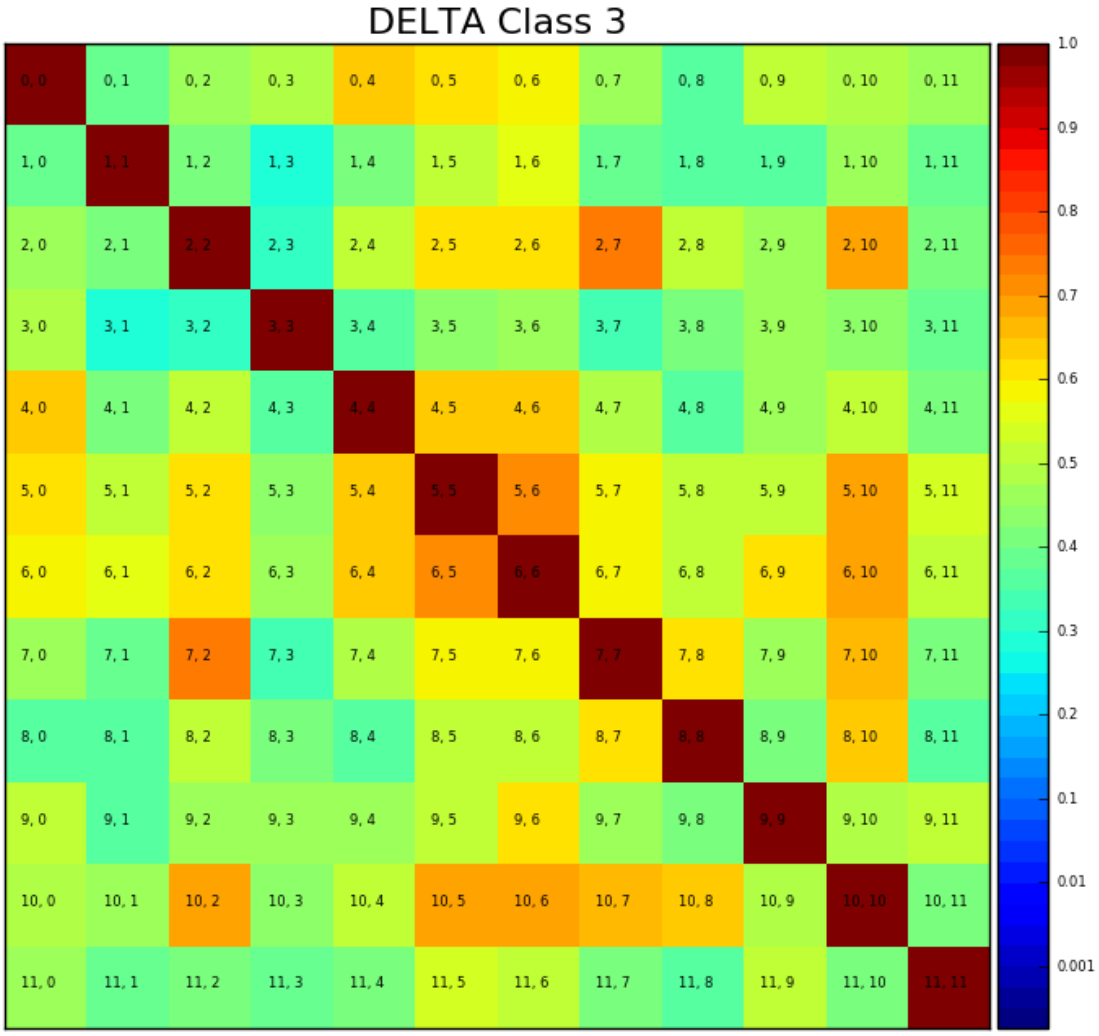

Figure 5.12: New similarity matrix for the RFFMs of class 3

5.5 The two dimensional Gaussian distribution

As we have already mentioned in the previous chapter, many FFMs and consequently RFFMs have only one region of large slip that includes the slip peak. By visual inspection of the set of the RFFM images, as many as 47 models with a single asperity of Class 1 have been selected and their slip distribution has been approximated by a two-dimensional Gaussian distribution. The same approach has been applied to 11 events belonging to Class 2 and to 5 events in Class 3.

The distribution used to approximate the slip over the fault has the expression given below:

$$g(x,y) = Ae^{-[a(x-x_0)^2-2b(x-x_0)(y-y_0)+c(y-y_0)^2]}$$

where A is the value of the slip peak (A=1 in our case), and (x_0, y_0) are the coordinates of the peak position. The coefficients include the information on the angle and on the dispersion:

$$a = \frac{\cos^2\theta}{2\sigma_x^2} + \frac{\sin^2\theta}{2\sigma_y^2}$$
$$b = -\frac{\sin 2\theta}{4\sigma_x^2} + \frac{\sin 2\theta}{4\sigma_y^2}$$
$$c = \frac{\sin^2\theta}{2\sigma_x^2} + \frac{\cos^2\theta}{2\sigma_y^2}$$

where θ is the angle of rotation with respect to the horizontal axis.

For each one-asperity RFFM two Gaussian distributions were found, one based on the least-squares best fitting, i.e. minimizing the square differences with the RFFM cell by cell, the other maximizes the similarity index, above described, with the RFFM.

Each "best distribution" has been selected among 910 different distributions, obtained by the combinations of the three unknown parameters σ_x, σ_y, θ.

5.5.1 The parameters range

The centre of the 2D Gaussian distribution was assumed to be coincident with the position of the slip peak. Once fixed (x_0, y_0), the distribution depends only on the parameters σ_x, σ_y, θ.

The variation range of these parameters has been set up after several attempts. For events belonging to class 1, the parameters σ_x and σ_y have been varied between 0.1 and 0.55 with a step of 0.05, while θ ranged from 0° to 81° in ten, equally spaced, steps of 9°. The choice of varying θ between 0° and 81° (and not between 0 and 180°) is due to the symmetry of the Gaussian function. The same holds for what regards θ = 90°, since it gives the same distribution as θ = 0°, provided that σ_x and σ_y are exchanged.

Though with the above choice each parameter may assume 10 different values, the total number of the different distributions obtained is actually 910, when $\sigma_x = \sigma_y$ the distribution is isotropic and the angle loses significance.

Regarding class 2, σ_x and σ_y were allowed to vary between 0.15 and 0.60 with a step of 0.05. The angle attained the same 10 values used for class 1.

For class 3, instead, σ_x was attributed 20 values between 0.1 and 1.05 with a step of 0.05, σ_y 10 values between 0.1 and 0.55 with a step of 0.05, with angle variable between 0° and 36° with equally spaced steps of 5°.

It is easy to verify that for the Gaussian function, the loci of constant height are represented by ellipses whose centre coincides with the centre (x_0, y_0) of the Gaussian itself. It then makes sense to introduce also the "eccentricity" (ε)

$$\epsilon = \sqrt{1 - \frac{\sigma_y^2}{\sigma_x^2}}$$

as an additional parameter to characterise our distributions.

The tables below (*Table 5.1, Table 5.2, Table 5.3*) summarise the parameters for our best distributions for all events in the three different classes. *Figure 5.13* through *Figure 5.17* show the best r.m.s. and s-index distributions for each class.

Table 5.1: Parameters of rms and s-index ellipses for Class 1. The angle is measured counter-clockwise from the positive horizontal axis.

I.N.	ε (rms)	θ (rms)	σ_x (rms)	σ_y (rms)	rms	ε (s-index)	θ (s-index)	σ_x (s-index)	σ_y (s-index)	s-index
1	0	0	0.2	0.2	0.07	0	0	0.2	0.2	0.86
3	0.75	9	0.3	0.2	0.17	0.87	9	0.4	0.2	0.76
6	0.97	9	0.4	0.1	0.14	0.93	9	0.55	0.2	0.71
9	0.6	27	0.25	0.2	0.09	0.75	36	0.3	0.2	0.85
10	0.66	36	0.2	0.15	0.14	0	0	0.55	0.55	0.81
11	0.92	171	0.25	0.1	0.14	0.95	171	0.5	0.15	0.68
12	0.75	153	0.3	0.2	0.19	0.84	162	0.55	0.3	0.83
13	0.66	0	0.4	0.3	0.1	0.71	0	0.5	0.35	0.91
16	0	0	0.2	0.2	0.1	0.82	135	0.35	0.2	0.73
17	0.87	162	0.4	0.2	0.15	0.92	162	0.5	0.2	0.83
18	0.66	171	0.4	0.3	0.07	0.48	162	0.4	0.35	0.92

25	0.75	0	0.15	0.1	0.11	0.9	99	0.35	0.15	0.62
31	0.83	135	0.45	0.25	0.21	0	0	0.55	0.55	0.81
32	0.66	162	0.4	0.3	0.17	0.42	153	0.55	0.5	0.89
33	0.87	153	0.5	0.25	0.12	0.77	153	0.55	0.35	0.85
35	0.6	18	0.25	0.2	0.06	0.6	18	0.25	0.2	0.9
37	0.96	27	0.35	0.1	0.23	0.42	108	0.55	0.5	0.79
40	0.8	171	0.25	0.15	0.15	0.93	171	0.4	0.15	0.72
41	0.94	18	0.3	0.1	0.17	0.97	18	0.4	0.1	0.66
43	0.66	18	0.2	0.15	0.12	0.87	18	0.3	0.15	0.74
44	0.7	9	0.35	0.25	0.06	0.7	0	0.35	0.25	0.9
51	0.9	9	0.35	0.15	0.13	0.93	9	0.55	0.2	0.8
53	0.6	171	0.25	0.2	0.07	0	0	0.2	0.2	0.87
54	0.75	18	0.3	0.2	0.05	0.75	18	0.3	0.2	0.91
55	0	0	0.15	0.15	0.11	0	0	0.2	0.2	0.73
59	0.8	0	0.25	0.15	0.13	0	0	0.2	0.2	0.75
60	0	0	0.2	0.2	0.14	0	0	0.2	0.2	0.72
61	0.87	171	0.3	0.15	0.07	0.9	171	0.35	0.15	0.86
62	0.75	0	0.15	0.1	0.1	0	0	0.2	0.2	0.67
63	0.66	90	0.2	0.15	0.15	0.82	99	0.35	0.2	0.71
65	0	0	0.15	0.15	0.1	0.66	135	0.2	0.15	0.7
69	0.82	171	0.35	0.2	0.07	0.7	171	0.35	0.25	0.92
71	0.87	18	0.5	0.25	0.12	0.87	18	0.5	0.25	0.9
74	0.75	90	0.15	0.1	0.09	0	0	0.15	0.15	0.65
77	0	0	0.15	0.15	0.08	0.66	27	0.2	0.15	0.75
80	0.87	9	0.2	0.1	0.13	0.92	9	0.25	0.1	0.64
81	0.92	0	0.25	0.1	0.12	0.96	0	0.35	0.1	0.7
82	0	0	0.25	0.25	0.14	0.55	135	0.3	0.25	0.79
84	0.87	162	0.2	0.1	0.13	0.6	117	0.25	0.2	0.67
85	0.87	171	0.2	0.1	0.07	0.87	171	0.2	0.1	0.77
86	0.75	90	0.15	0.1	0.1	0.66	9	0.2	0.15	0.65
88	0	0	0.1	0.1	0.06	0.75	144	0.15	0.1	0.69
90	0	0	0.15	0.15	0.16	0	0	0.2	0.2	0.6
91	0.66	45	0.2	0.15	0.09	0.66	45	0.2	0.15	0.8
92	0.75	18	0.15	0.1	0.12	0.92	27	0.25	0.1	0.57
97	0.92	18	0.25	0.1	0.15	0.82	9	0.35	0.2	0.65
98	0.7	135	0.35	0.25	0.13	0.66	135	0.4	0.3	0.86

Table 5.2: Parameters of rms and s-index ellipses for Class 2. The angle is measured counter-clockwise from the positive horizontal axis.

I.N.	ε (rms)	θ (rms)	σ_x (rms)	σ_y (rms)	rms	ε (s-index)	θ (s-index)	σ_x (s-index)	σ_y (s-index)	s-index
4	0.66	99	0.2	0.15	0.19	0.75	153	0.6	0.4	0.53
7	0.9	126	0.45	0.2	0.14	0.55	153	0.6	0.5	0.66
22	0.78	9	0.4	0.25	0.15	0.81	0	0.6	0.35	0.75
42	0.94	0	0.6	0.2	0.09	0.91	0	0.6	0.25	0.83
45	0.83	9	0.45	0.25	0.12	0.89	18	0.55	0.25	0.79
56	0.87	162	0.6	0.3	0.21	0.87	162	0.6	0.3	0.75
58	0.8	144	0.5	0.3	0.25	0.55	162	0.6	0.5	0.64
68	0.97	0	0.6	0.15	0.25	0.94	0	0.6	0.2	0.58
78	0.87	0	0.3	0.15	0.14	0.94	9	0.45	0.15	0.64
87	0.93	0	0.55	0.2	0.07	0.93	0	0.55	0.2	0.87
95	0.66	144	0.6	0.45	0.14	0.4	153	0.6	0.55	0.84

Table 5.3: Parameters of rms and s-index ellipses for Class 3. The angle is measured counter-clockwise from the positive horizontal axis.

I.N.	ε (rms)	θ (rms)	σ_x (rms)	σ_y (rms)	rms	ε (s-index)	θ (s-index)	σ_x (s-index)	σ_y (s-index)	s-index
15	0.6	0	0.25	0.2	0.1	0.97	0	1.05	0.25	0.46
30	0.77	63	0.55	0.35	0.16	0.68	0	0.75	0.55	0.63
46	0.94	171	1.05	0.35	0.22	0.85	0	1.05	0.55	0.71
67	0.89	171	0.55	0.25	0.09	0.95	0	0.8	0.25	0.76
89	0.97	0	1.05	0.25	0.17	0.96	0	1.05	0.3	0.71

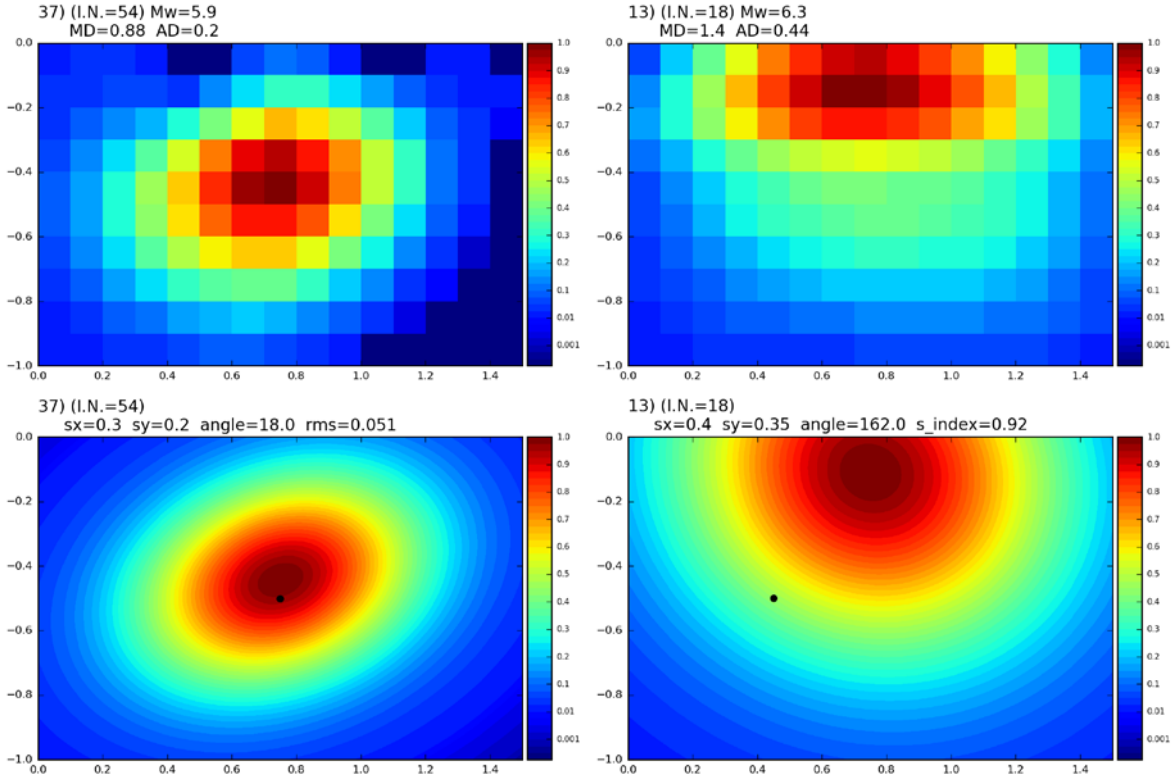

Figure 5.13: Best rms (left) and s-index (right) Gaussian distributions for Class 1. The black dot represents the hypocentre position.

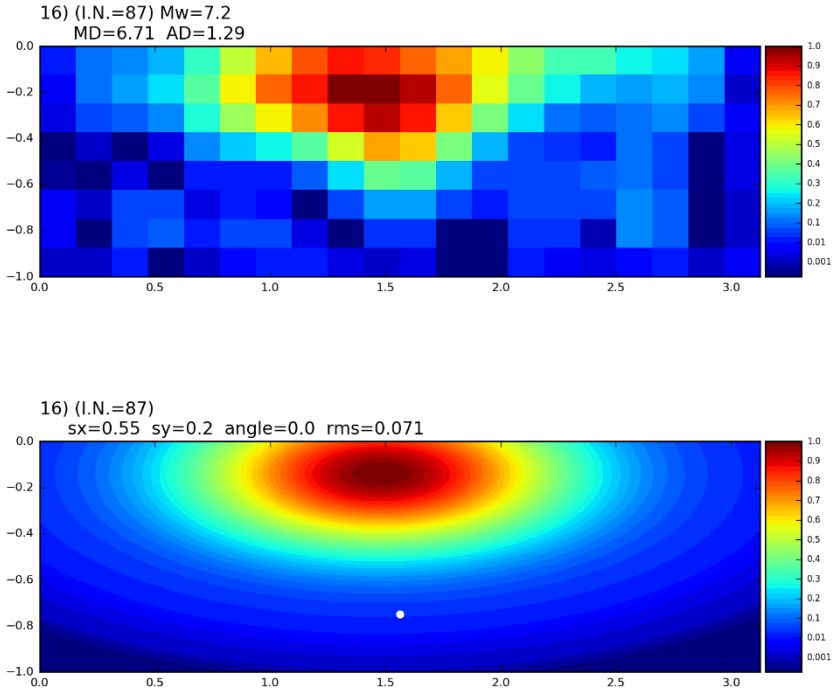

Figure 5.14: Best rms ellipse for Class 2. The white dot represents the hypocentre position.

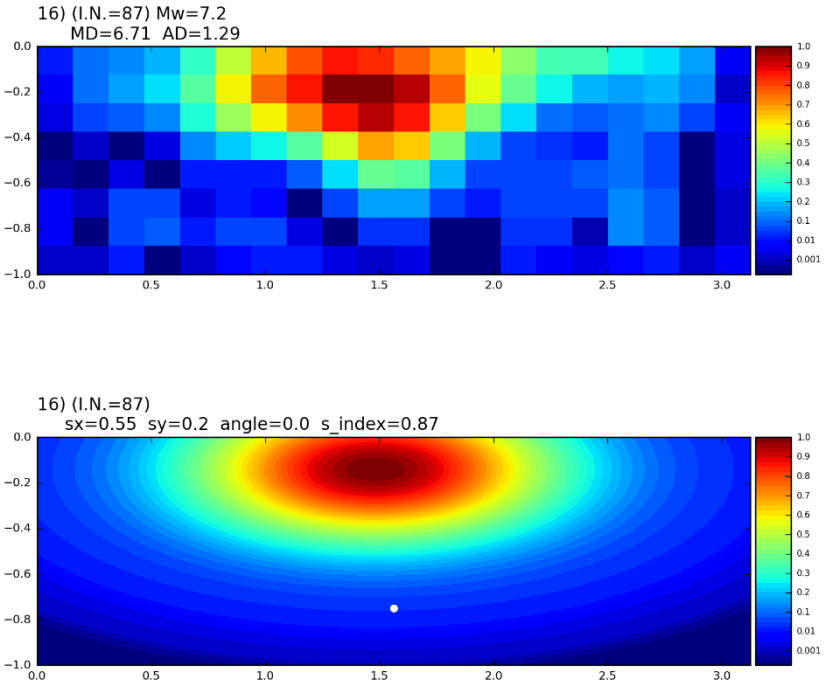

Figure 5.15: Best rms ellipse for Class 2. The white dot represents the hypocentre position.

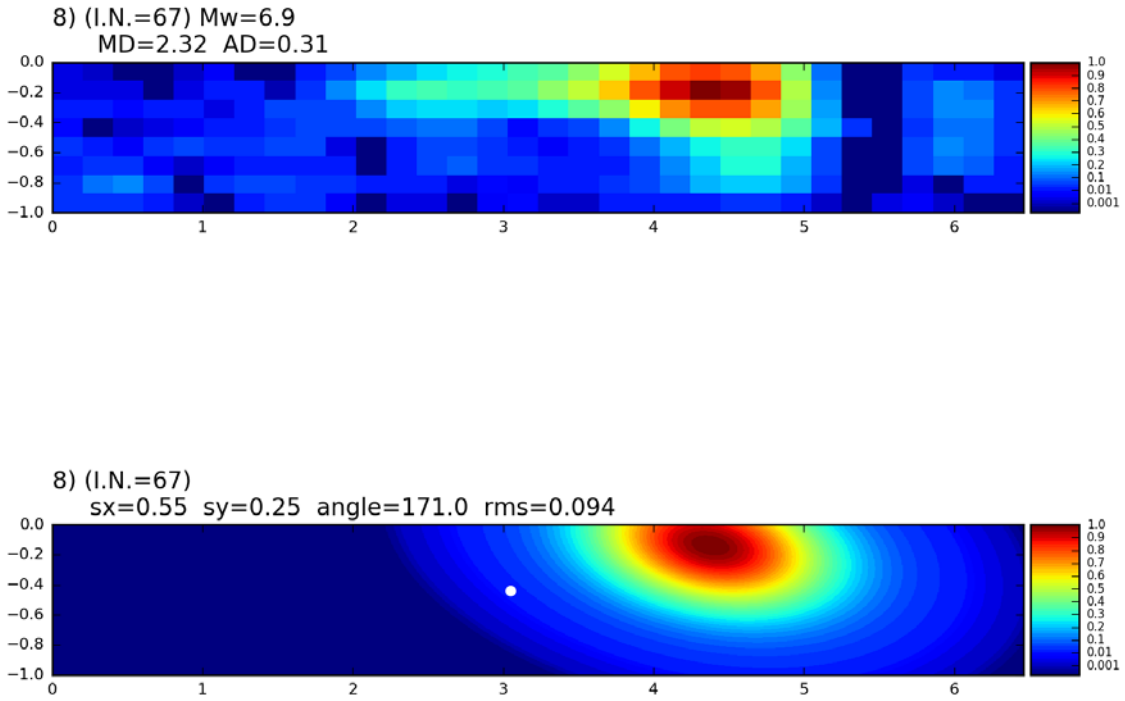

Figure 5.16: Best rms ellipse for Class 3. The white dot represents the hypocentre position.

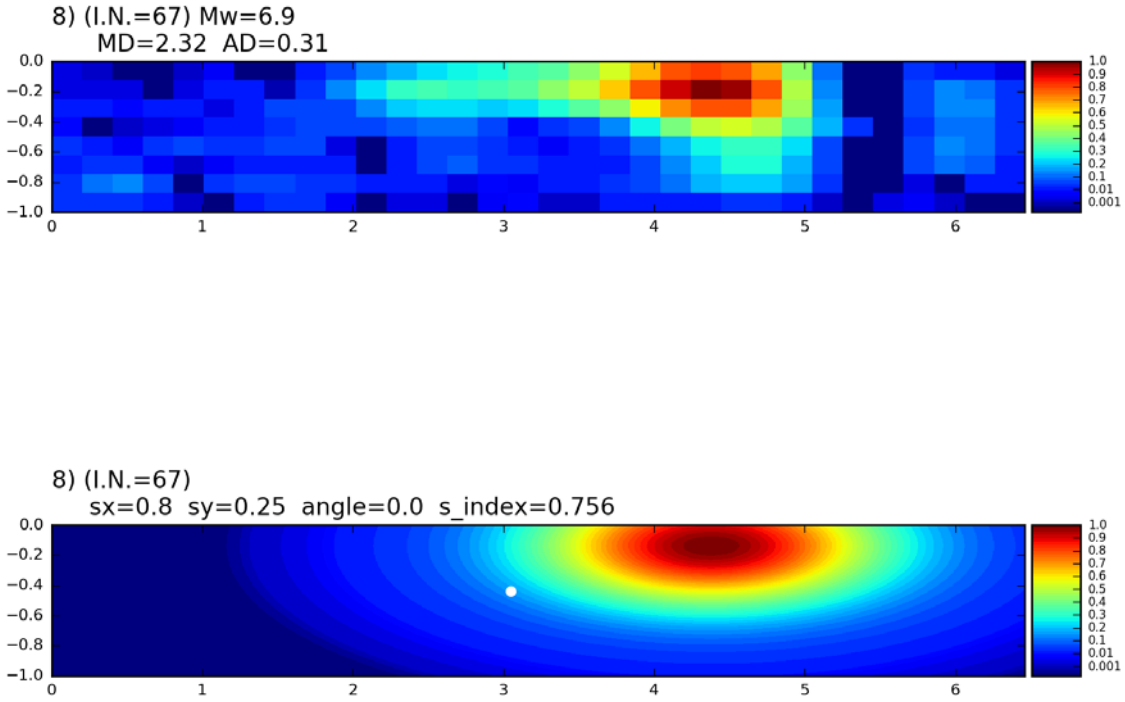

Figure 5.17: Best s-index ellipse for Class 3. The white dot represents the hypocentre position.

The next charts (*Figure 5.18, Figure 5.19, Figure 5.20*) highlight some characteristics of the obtained distributions. For each class, the red bars refer to the r.m.s. ellipses, the light blue bars refer to the s-index ellipses.

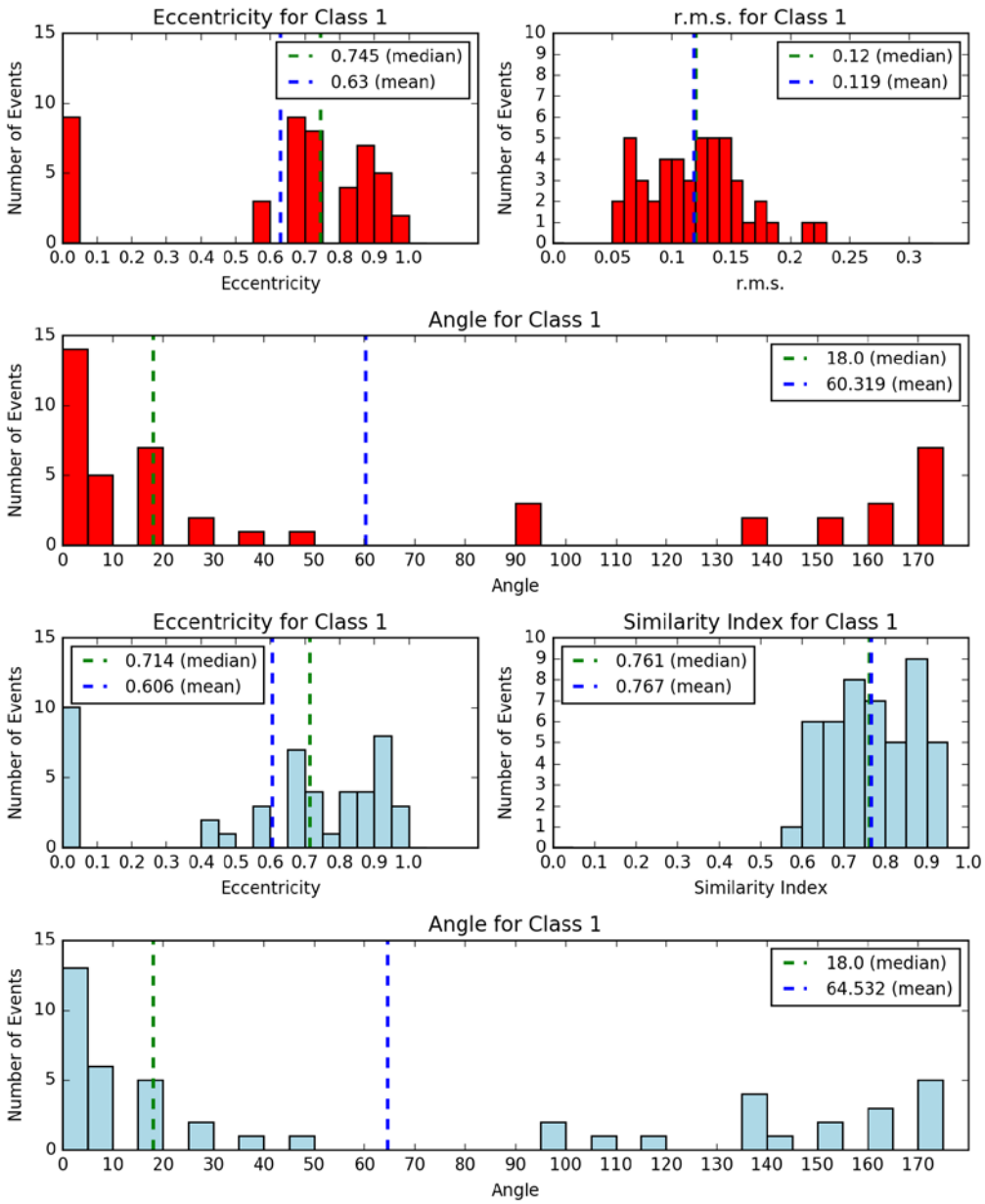

Figure 5.18: Distribution of the parameters of the 2D Gaussian Function for Class 1, red for the r.m.s. distributions, light blue for the s-index distribution.

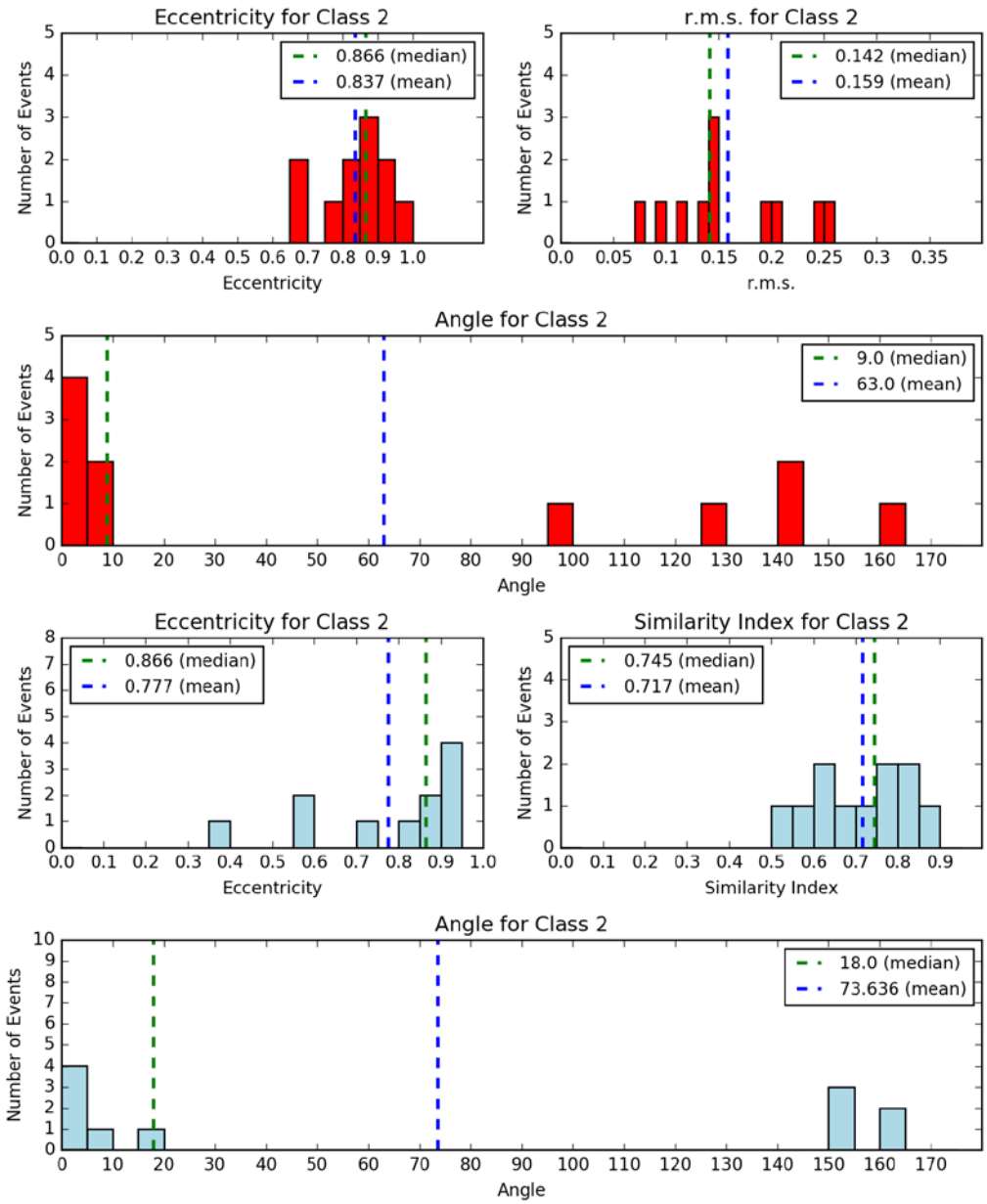

Figure 5.19: Distribution of the parameters of the 2D Gaussian Function for Class 2, red for the r.m.s. distributions, light blue for the s-index distribution.

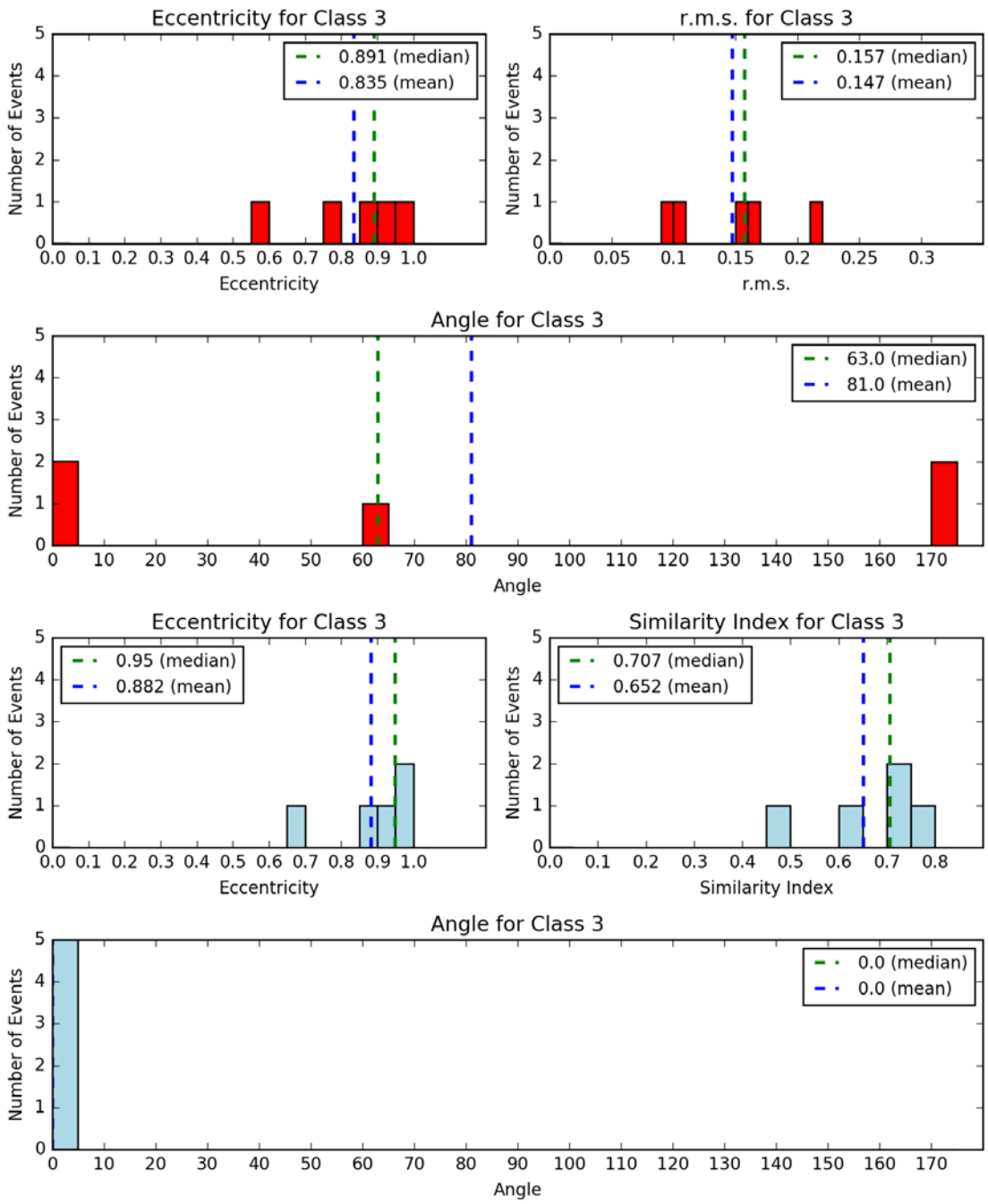

Figure 5.20: Distribution of the parameters of the 2D Gaussian Function for Class 1, red for the r.m.s. distributions, light blue for the s-index distribution.

Looking at the histograms, it is possible to note some interesting facts.

Considering firstly Class 1, the r.m.s. value varies in the range $0.051 \leq \text{r.m.s.} \leq 0.23$, while the similarity index is always larger than 0.5, with the smaller value in 0.55.

The median value for the eccentricity for the r.m.s. ellipses is 0.745, which corresponds to the ratio σ_x / σ_y = 1.5, reflecting the class aspect ratio. One may further note that 9 events for the r.m.s. and 10 events for the s-index have best representations coinciding with circumferences.

The angle is always smaller than 50° or larger than 130°, with the exception of 3 cases over 47. *Figure 5.18* allows to appreciate that, within these ranges, and increasing number of ellipses are oriented with the major axis along the horizontal direction. The three events that present an angle of θ = 90° for the distribution (thus with the slip varying mainly in the vertical direction), are:

- I.N. = 63, L'Aquila, Italy 04/06/2009, Normal earthquake;
- I.N. = 74, Northern Sumatra, 04/06/2010, Reverse earthquake;
- I.N. = 86, Van, Turkey 10/23/2009, Reverse earthquake.

The situation is just slightly different for the s-index ellipses. Four events present an angle between 90° and 130°. These events are:

- I.N. = 25, Bhuj, India 01/26/2001, Reverse earthquake (θ = 99°);
- I.N. = 37, Niigata-Ken Chuetsu, Japan 10/23/2004, Reverse earthquake (θ = 108°);
- I.N. = 63, L'Aquila, Italy 04/06/2009, Normal earthquake (θ = 99°);
- I.N. = 84, Vanuatu, 08/20/2011, Reverse earthquake (θ = 117°).

Note that only event 63 is approximated in both the cases with a distribution whose angle is close to the vertical, demonstrating that in general the two comparison methods can lead to different results.

Looking at the statistics regarding Class 2, it is immediately evident that no event can be approximated by radially symmetric Gaussian distributions ($\sigma_x = \sigma_y$), neither for rms ellipses, nor for s-index ellipses.

The r.m.s. is comprised between 0.07 and 0.26. For the s-index the smaller value is 0.55 and the average value (0.72) is slightly smaller than that of Class 1.

Regarding the angles, for the r.m.s. ellipses just two events present angle close to the down-dip direction. They are:

- I.N. = 4, Hokkaido-nansei-oki, Japan 07/12/1993, Reverse earthquake (θ = 99°);
- I.N. = 7, Kobe, Japan 01/16/1995, Strike-Slip earthquake (θ = 126°).

In this case, thus, there is a strike slip event best represented by a distribution more oriented to the down-dip direction. This distribution presents an eccentricity of 0.9 and r.m.s. = 0.14. The s-index ellipse for the same event, instead, has a greater angle (153°) and a smaller eccentricity (0.31), with s-index = 0.66. For the s-index ellipses, in fact, there are no angles between 25° and 145°.

Class 3 also presents all best distribution characterized by $\sigma_x \neq \sigma_y$.

Among the r.m.s. ellipses, there is one with angle of 63°:

- I.N. = 30, Carlsberg Ridge, 07/15/2003, Strike-Slip earthquake.

This distribution presents an eccentricity of 0.6 and the r.m.s. value equal to 0.157. The s-index ellipse related to the same event is characterized by $\theta = 0°$, eccentricity = 0.46, s-index = 0.63.

For the s-index ellipses the angle is always 0°, and the mean eccentricity is 0.89, corresponding to a ratio $\sigma_x/\sigma_y > 2$.

In the next chapter, the ability of the best Gaussian distributions computed above to reproduce the RFFM will be tested and quantified for each event by comparing the coseismic surface vertical field produced by the two slip distributions.

6 Chapter 5

As already mentioned several times in the previous chapters, the distribution of the slip over the fault plays an important role in the seismic studies. For instance, the propagation pattern and the frequency content of the seismic waves radiating from the source, as well as the permanent deformation field produced by the dislocation in the surrounding medium heavily depend on the slip heterogeneity. Moreover, for earthquakes occurring off-shore or near to the coast and having the potential to be tsunamigenic, the slip heterogeneity on the fault, and consequently the seafloor vertical displacement field pattern, plays a relevant role in determining the tsunami wave propagation features and the run-up distribution along the coasts.

The free surface displacement field induced by a prescribed slip distribution on the fault at depth will be used in the discussion presented herein as a metric to compare different slip patterns, taking the FFMs contained in SRCMOD as reference cases. In other words, we want to measure the “quality” of our ellipses as representations of the slip heterogeneity by making a comparative evaluation of the vertical surface displacement field generated by them and by other commonly used uniform of analytical slip distributions with the solutions obtained starting from the SRCMOD FFMs. We are going to present the results obtained over a subset of the events for which the ellipses have been computed, and we will discuss the results to highlight strengths and weaknesses of our approach.

6.1 The procedure

For any given earthquake, our goal is to compare the co-seismic vertical displacement component corresponding computed starting from the SRCMOD FFM, taken as reference case, with the same displacement component computed from the following alternative slip distributions:

- a homogeneous fault model;
- a heterogeneous fault model, namely the so-called “Smooth Closure Condition” distribution (hereafter SCC), in which the heterogeneity depends only on depth; it was originally introduced by Freund and Barnett (1976) (see e.g. Geist and Dmowska, 1999 for details);
- the rms ellipses;

- the s-index ellipses.

The choice of the first two is dictated by the observation that they have been, and are still widely used in many studies dealing, for example, with the deformation fields induced by earthquakes, with earthquake hazard assessment, with the simulation of earthquake-induced tsunamis, with tsunami hazard assessment and tsunami early warning (see e.g. Geist and Dmowska, 1999; Tinti et al., 2005; Gutscher et al. 2006; Babeyko et al., 2010; Tonini et al., 2011, and many others).

For a given slip distribution, the surface displacement field, and in particular its vertical component, is computed here by means of the widely used analytical formulas by Okada (1992), in which a rectangular fault is buried in a perfectly elastic, homogeneous and isotropic elastic half-space. A heterogeneous slip distribution is obtained by summing up linearly the contributions by several homogeneous-slip faults.

The computations have been carried out over a subset of 57 events, extracted from the 98-event database presented in Chapter 2 based on the following criteria: 1) we chose the events for which we computed ellipses (see Chapter 4 and Appendix A); 2) of these, we kept only those events whose original FFM is composed by only one fault segment.

For each of the 57 events, we started from the SRCMOD FFM reference case (hereafter FFM-REF). We adopted the same Cartesian reference frame and the same subdivision in subfaults of the fault plane as proposed in FFM-REF. More precisely, the basic geometric and focal properties of the fault (total and subfaults' length, total and subfaults' width, average strike, average dip, average rake, position of one reference point for the subfaults) have been taken from FFM-REF and used for all other cases. The only varying parameter is the slip amount on each subfault, computed as follows:

- for FFM-REF, it is simply read from the data attached to FFM-REF itself;
- for the homogeneous slip distribution case, we computed the average slip value over FFM-REF and assigned it identically to all subfaults;
- for the SCC case, we took advantage of the fact that the average slip of the SCC distribution equals 1, so the slip to be assigned to each subfault is simply the product of the FFM-REF average slip times the SCC integral slip function computed on each subfault's centre of mass. The SCC distribution depends on the width of the fault, on its dip and on a so-called "skewness" parameter, which

determines the position of the slip peak along the down-dip direction. In our approach, the skewness parameter is taken to coincide with the depth coordinate of the centre of the FFM-REF subfault showing the highest slip;

- for the Gaussians, we started from the reference normalized geometries of the three aspect-ratio classes described in Chapters 3 and 4. The normalized geometries of each class have been discretized with the same number of rows and columns as in FFM-REF. The equation of the Gaussians, both for the rms and the s-index cases, have been recomputed in the centre of mass of each subfault. If needed, the slip pattern obtained has been mirrored with respect to the central vertical axis of the fault, and then assigned to the final FFM, after rescaling the rms Gaussian to the maximum FFM-REF slip and the s-index Gaussian to the average FFM-REF slip.

The vertical surface displacements were computed over a flat domain corresponding to the quote z = 0. The domain is centred in the mid point of the surface projection of the FFM-REF fault plane. Its extension is twice the total length of the fault in both the East-West and North-South directions. This choice revealed to be not completely appropriate for deep faults having shallow dip angles, as will be commented later on. A future improvement will consist in taking the depth and dip of the fault into account in the definition of the computational domain. The domain has been discretized with a grid of 100 x 100 nodes: as the domain extension varies for the different considered events, the same happens also for the grid steps.

6.2 Results

For each of the comparison mentioned above, the ability of a given slip pattern to mimic the reference SRCMOD case is measured by computing the following Misfit value:

$$msf = \sqrt{\frac{\sum_0^n (U_z^i - u_z^i)^2}{\sum_0^n (U_z^i)^2}}$$

where U_z is the vertical-displacement of the reference field, u_z is the one of the considered field.

The misfit values resulting from the different comparisons are reported in *Table 6.1* and shown in *Figure 6.1*.

Table 6.1: Misfit values between the vertical-displacement fields calculated for the reference FFM events and for each of the slip distributions referred to in columns 2-5.

I.N.	Uniform	rms ellipses	s-index ellipses	SCC
1	0.777	0.38	0.383	0.686
3	0.5	0.414	0.401	0.43
6	0.855	0.6	0.579	0.667
7	0.821	0.375	0.737	0.806
9	0.469	0.207	0.267	0.366
10	0.669	0.612	0.525	0.674
11	0.621	0.477	0.375	0.45
12	0.55	0.554	0.394	0.536
13	0.397	0.17	0.11	0.344
15	0.831	0.786	1.085	0.818
16	0.834	0.504	0.476	0.75
17	0.42	0.304	0.223	0.331
18	0.554	0.112	0.131	0.49
25	0.446	0.685	0.52	0.551
30	0.765	0.441	0.516	0.779
32	0.183	0.169	0.086	0.341
33	0.606	0.229	0.234	0.432
35	0.507	0.211	0.087	0.32
37	0.315	0.581	0.135	0.303
40	0.907	0.552	0.708	0.767
41	0.696	0.511	0.537	0.553
42	0.969	0.375	0.466	0.95
43	0.236	0.468	0.217	0.215
44	0.73	0.162	0.175	0.595
45	0.828	0.366	0.441	0.751
46	0.421	0.395	0.508	0.447
51	0.883	0.444	0.428	0.641
53	0.576	0.132	0.173	0.42
54	0.554	0.152	0.129	0.42
55	0.773	0.343	0.324	0.656
58	0.51	0.6	0.639	0.57
60	0.375	0.206	0.203	0.163
61	0.697	0.181	0.196	0.54
62	0.549	0.4	0.422	0.468
63	0.622	0.433	0.424	0.543
65	0.862	0.355	0.384	0.835
67	0.832	0.376	0.445	0.825
68	0.655	0.512	0.596	0.642

69	0.129	0.23	0.011	0.091
71	0.402	0.163	0.131	0.423
74	0.889	0.541	0.631	0.793
77	0.96	0.382	0.413	0.84
78	0.614	0.516	0.526	0.656
80	0.675	0.297	0.193	0.101
81	0.827	0.398	0.471	0.554
82	0.958	0.459	0.494	0.67
84	0.59	0.462	0.23	0.334
85	0.602	0.239	0.171	0.414
86	0.625	0.405	0.345	0.543
87	0.863	0.217	0.193	0.851
88	0.868	0.329	0.459	0.745
89	0.731	0.688	0.874	0.702
90	0.86	0.764	0.557	0.779
92	0.625	0.462	0.693	0.546
95	0.017	0.235	0.052	0.018
97	0.691	0.526	0.511	0.678
98	0.651	0.35	0.325	0.62

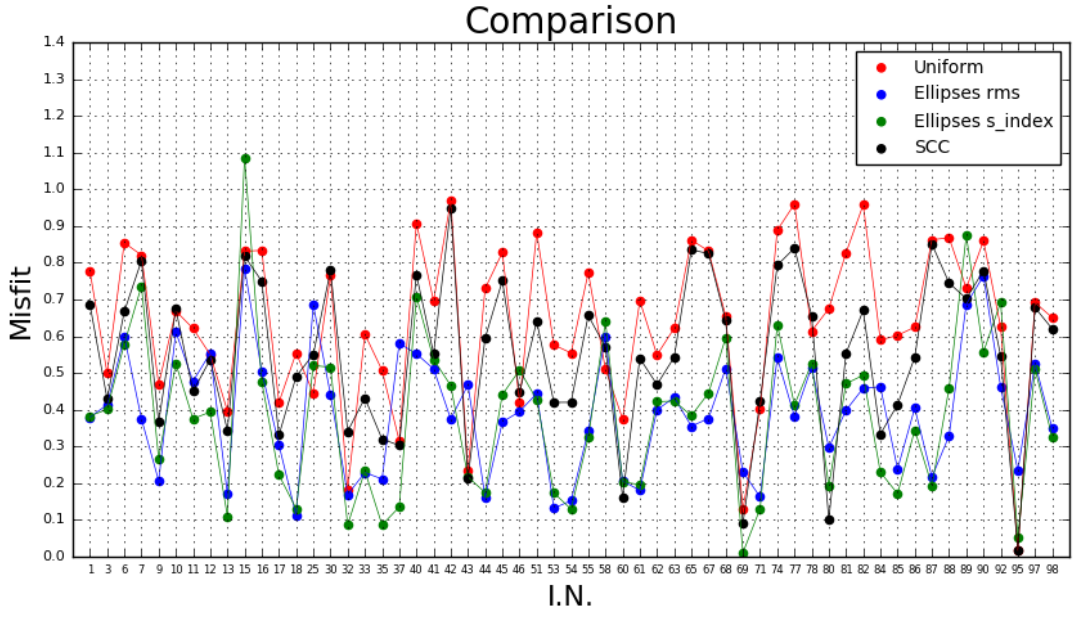

Figure 6.1: Misfit values for the different cases.

From *Figure 6.1* it is evident that the 2D Gaussian distributions, with the exception of some models, give the least misfit field. Therefore, on average they appear to provide a more adequate representation of the on-fault SRCMOD slip heterogeneity with respect

to the purely homogeneous and the analytical SSC models. *Table 6.2* show the average, the minimum and the maximum misfit value for the four slip distributions compared to the reference one.

Table 6.2: Average, minimum and maximum misfit value for each slip distribution.

Slip distribution	Mean Misfit	Min Misfit	Max Misfit
Uniform	0.638	0.017	0.969
Rms ellipses	0.394	0.112	0.786
s-index ellipses	0.385	0.011	1.08
SCC	0.551	0.018	0.950

The limit values are not that interesting, because there are few events with anomalous behaviour (some of them will be discussed later on). The average values of the misfit, instead, confirm the observation made on *Figure 6.1*, i.e. a general greater proximity of our distribution than the uniform one and the SCC to the reference model.

We now move from a general perspective to a per-event analysis. As a general approach, we propose figures showing simultaneously the vertical displacement fields relative to the five considered slip distributions. In order to facilitate the interpretation and comparison of the co-seismic vertical displacement fields, we attached to each case the corresponding FFM-REF setting and slip distributions, taken from the SRCMOD database (*Figure 6.3, Figure 6.5, Figure 6.7, Figure 6.9, Figure 6.11, Figure 6.17, Figure 6.13, Figure 6.15*).

6.2.1 Events with a very good performance of the Gaussian distributions

From *Figure 6.1* it is evident how, for some events, the Gaussian distributions calculated in Chapter 4 are definitely better for describing the co-seismic displacement field with respect to the homogeneous and SCC representations. The events considered as example are:

- I.N. = 44, Kashmir, 10/08/2005, Depth = 10.5 km, Oblique, dip = 29°, *Figure 6.2*;

- I.N. = 87, Sumatra, 01/10/2012, Depth = 18.4 km, Strike-Slip, dip = 75°, *Figure 6.4*.

From *Table 5.1, Table 5.2, Table 5.3* of the previous chapter, event 44 presents the same parameters for the two Gaussian distributions (σ_x *=0.35* σ_y*=0.25*) with the exception of the angle (θ_{rms}*=9°,*$\theta_{s\text{-}index}$*=0°*); the rms is small (0.063) and the similarity index high (0.9).

Event 87 is the event with the "best distributions" (both rms and s-index) for the class 2 and presents exactly the same parameters (σ_x , σ_y and θ coincident) in the rms and in the s-index cases, with rms = 0.071 and s-index = 0.87.

Looking at the original slip distribution, it is possible to note that the two events present a clear and distinguished asperity with a sharp peak at a relatively shallow depth; moreover, the slip pattern is highly varying in both spatial directions, but maintaining a good symmetry with respect to the peak position. The homogeneous and SCC approaches are not suited to such cases, the first trivially because it it totally misses the slip variation, the second because it can not reproduce the along-strike heterogeneity. On the other hand, the Gaussian distributions are able to mimic the on-fault slip pattern to a very satisfactory level.

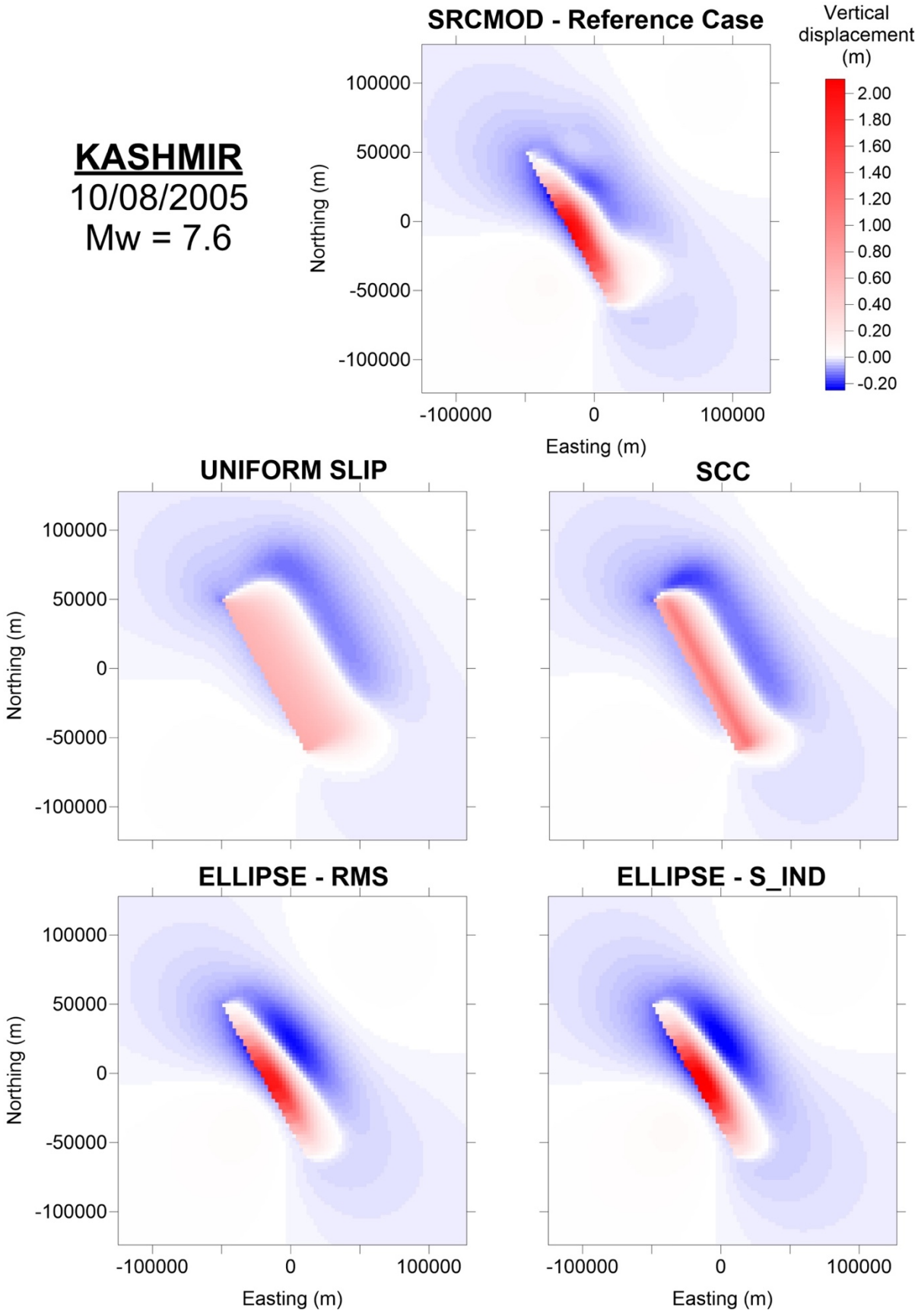

Figure 6.2: Near-source vertical-displacement fields for the event I.N. = 44

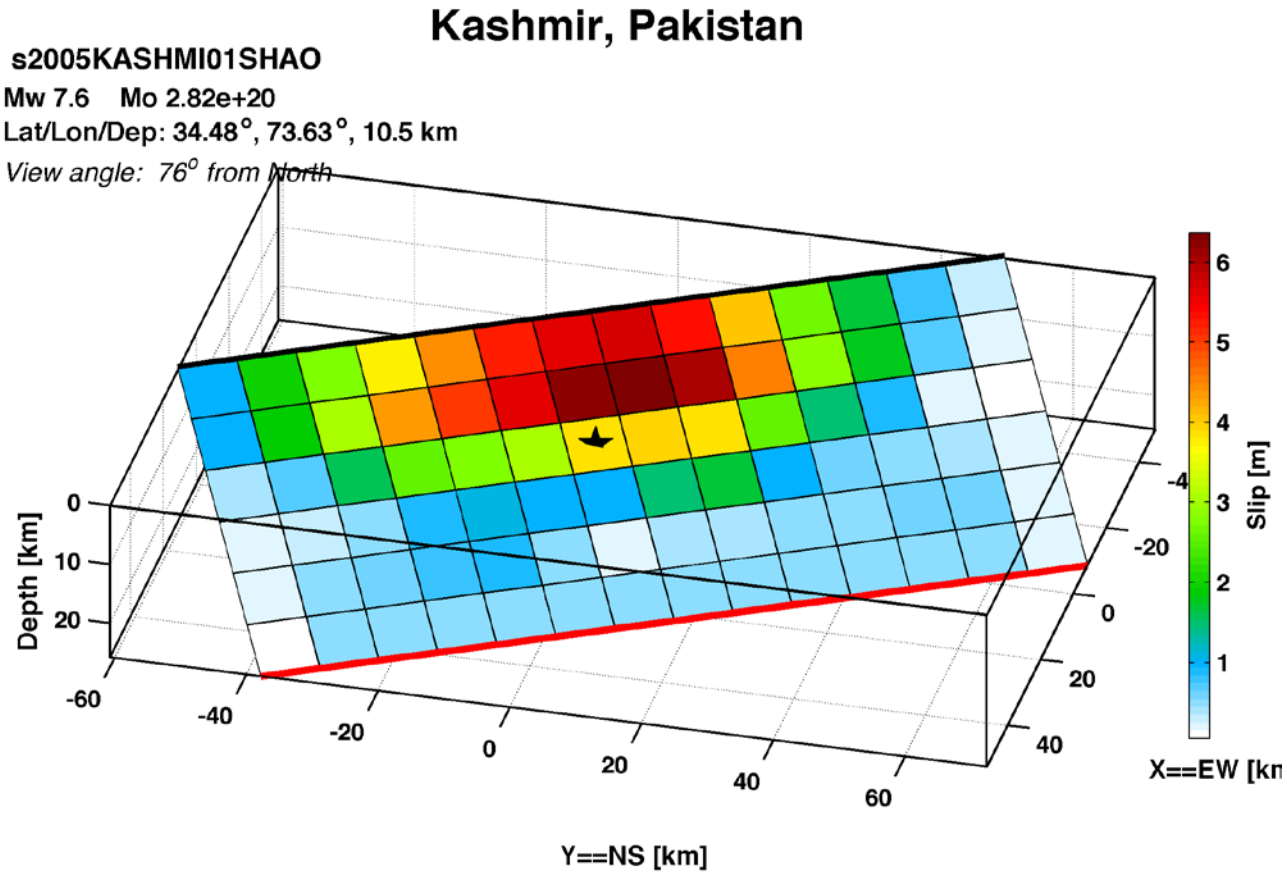

Figure 6.3: FFM representation of event 44, by Shao and Ji (UCSB, Kashmir 2005), taken from the SRCMOD database

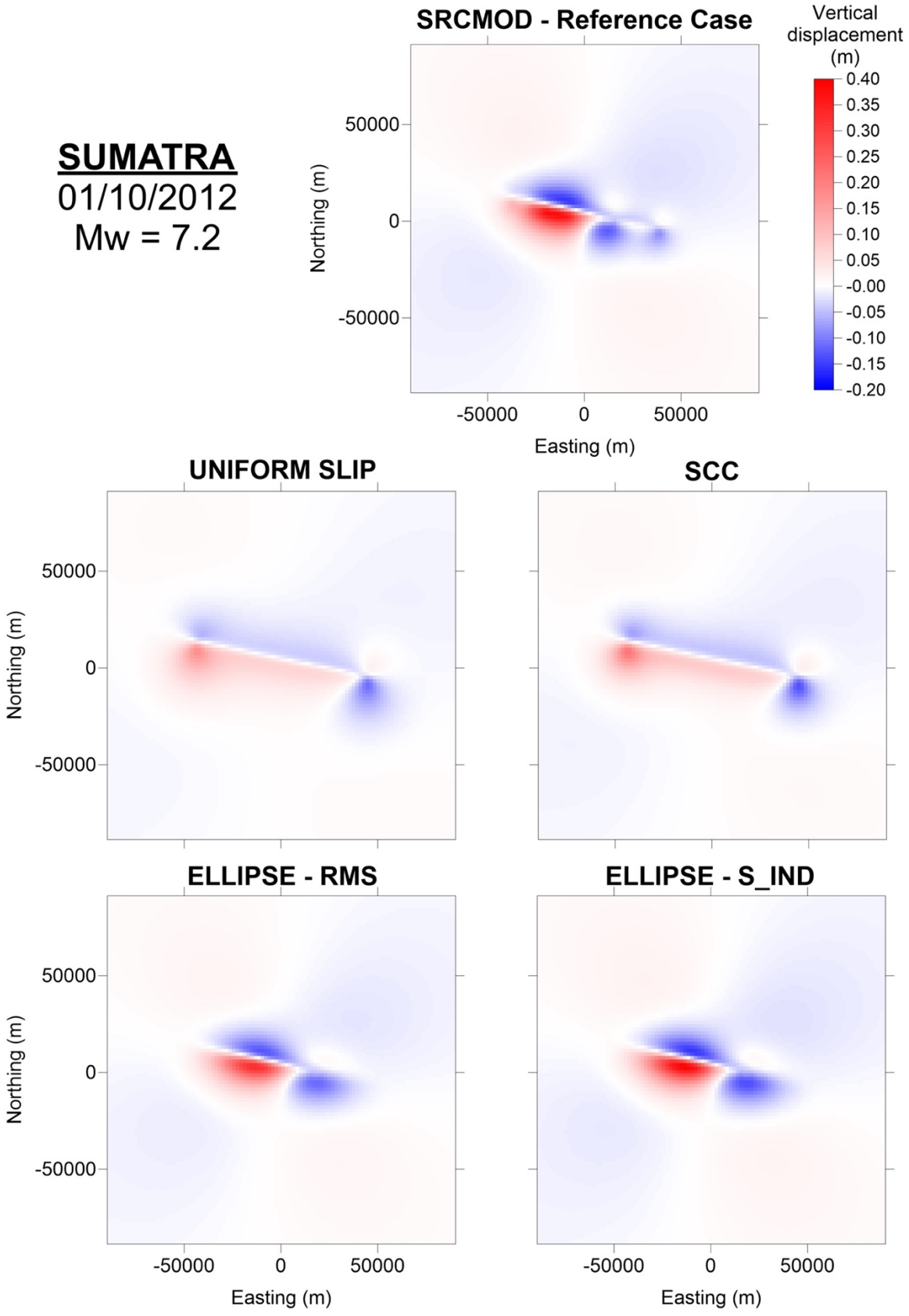

Figure 6.4: Near-source vertical-displacement fields for the event I.N. = 87

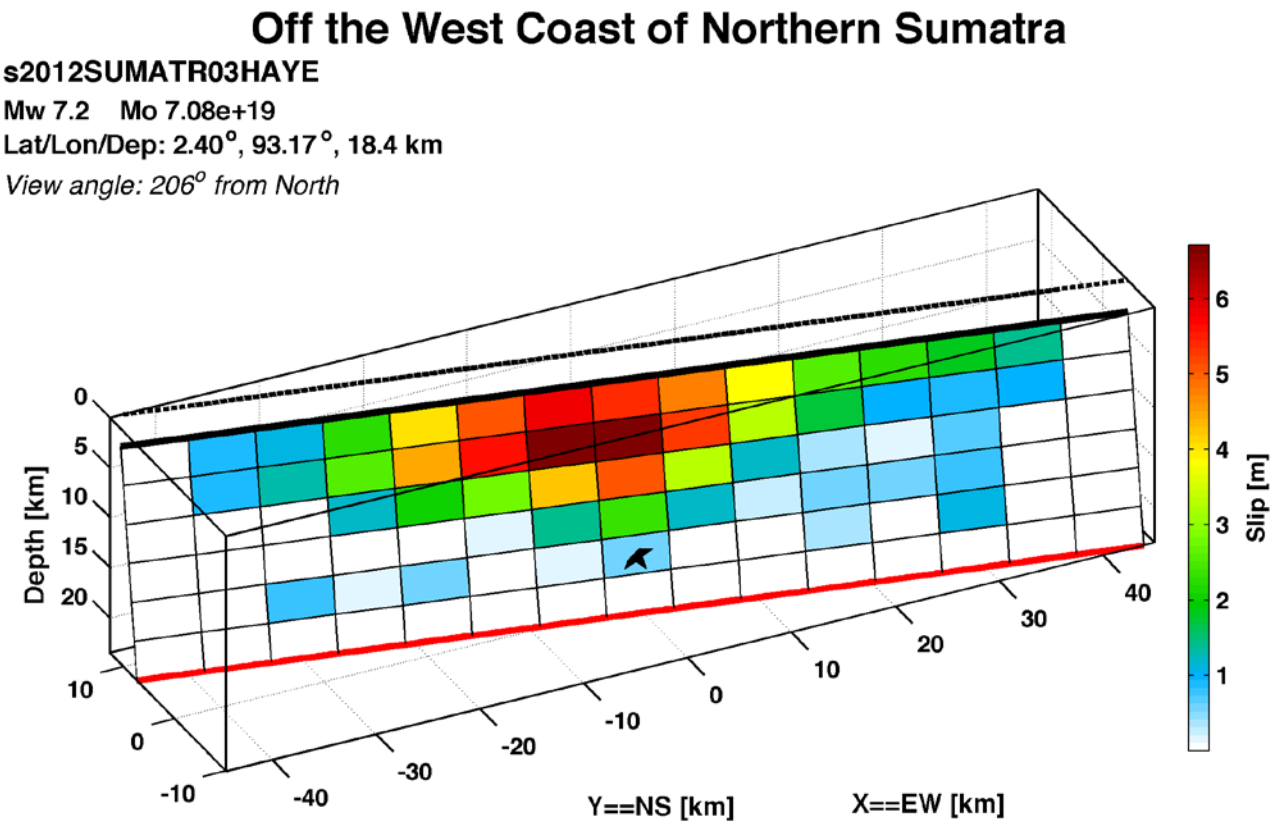

Figure 6.5: FFM representation of event 87, by Hayes(NEIC, Sumatra 2012), taken from the SRCMOD database

6.2.2 Events whose Gaussian distributions show unsatisfactory performance

Looking at *Table 6.1* one may observe that there are some models for which our distributions result worse than the uniform and SCC.

They are:

- I.N. = 15, Antarctica (SS segment), 03/25/1998, Depth = 12 km, Strike-Slip, dip = 88°, *Figure 6.6*;
- I.N. = 89, Sumatra, 04/11/2012, Depth = 22 km, Strike-Slip, dip = 64°, *Figure 6.8*;
- I.N. = 95, Okhotsk Sea, 05/24/2013, Depth = 608 km, Strike-Slip, dip = 95°, *Figure 6.10*:

As regards event 15, looking at the original FFM-REF slip distribution (*Figure 6.7*), one can appreciate that the highest concentration of slip is positioned in only a small portion of the fault surface; two further and spatially well separated asperities are observable in the middle shallow part of the fault, which are expected to contribute significantly to

the surface displacement field. As a result, trying to reproduce such a complicated slip pattern with single-peak Gaussian distributions is not appropriate. This is confirmed by the values of the distributions reported in *Table 5.3*. Event 15 belongs to the third aspect ratio class, and presents rms = 0.103 and s-index = 0.463. Thus both the indexes reveal a bad similarity to the related FFM. Furthermore, the two distribution are completely different between each other: the rms one presents $\sigma_x = 0.25$, $\sigma_y = 0.20$ while the s-index one $\sigma_x = 1.05$, $\sigma_y = 0.25$.

Still regarding event 15 one may also observe that, while the misfit relative to the rms ellipse is comparable to the values from uniform and the SCC cases, the s-index ellipse generates a vertical displacement with a largely different misfit with respect to the other distributions. The s-index ellipse, trying to reproduce the structure, includes in the central concentration of the slip also the separated asperities. The rms ellipse just reproduce the main asperity.

Event 89, again Class 3, instead, have the two distribution almost coincident: but the u_z field produced by the s-index one is worse than the rms one and other two distributions. This must be attributed to two main factors. First, the slip distribution exhibits a large central asperity elongated in along-strike direction with the peak located close to the left border of this area. The choice of using symmetrical distributions centred in the peak of slip , in this particular case, compromised our results. Second, we rescale the two distributions in a different way: for the rms one we multiply for the maximum, while for the s-index one, we used the mean value.

Regarding event 95, the high value of the depth (608 km) prevails over the slip distribution. Practically, the fault is seen as a point-source at the surface, so the slip details on the fault are lost. This tell us that this event should not be part of this analysis, and it will be removed in future.

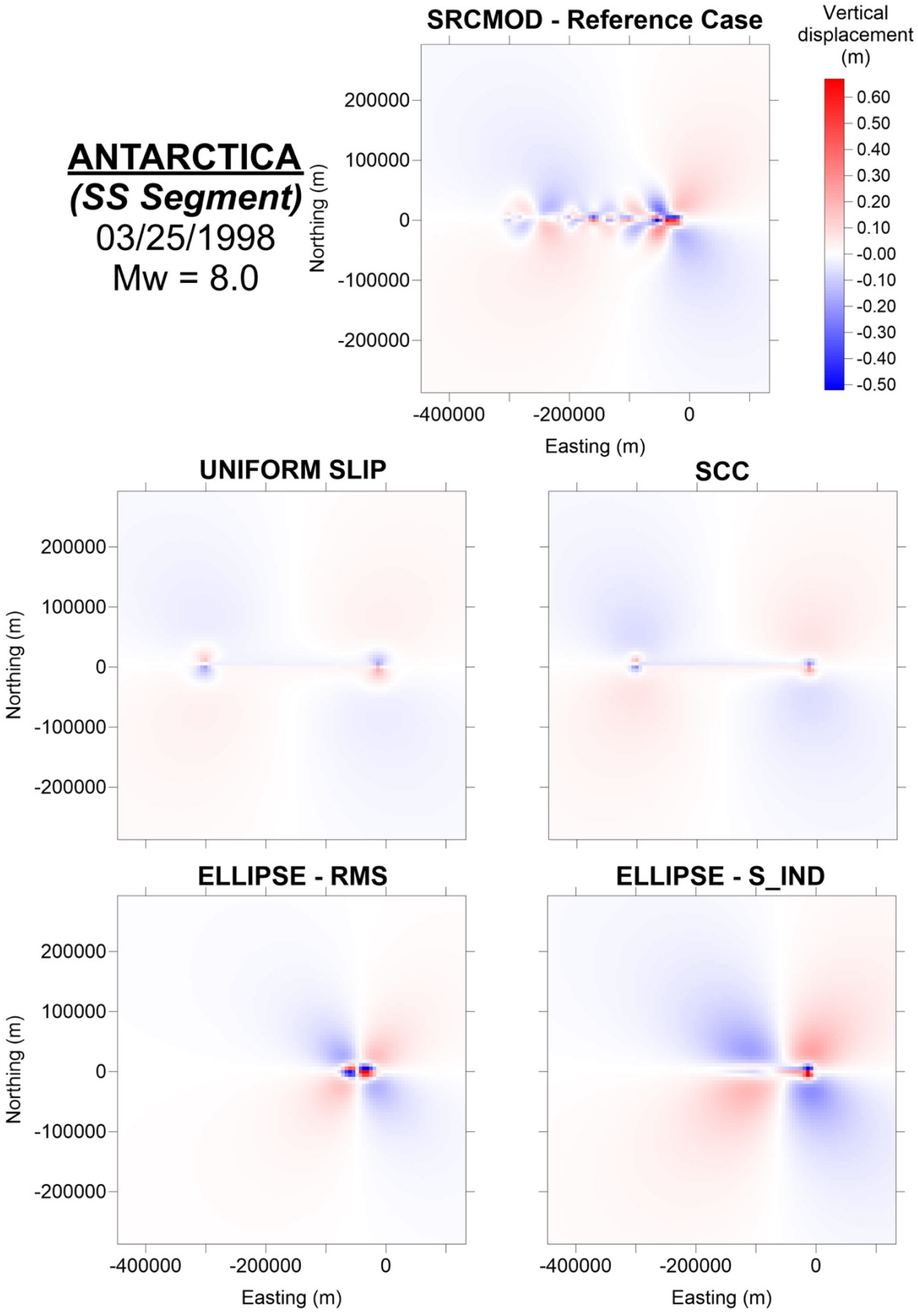

Figure 6.6: Near-source vertical-displacement fields for the event I.N. = 15

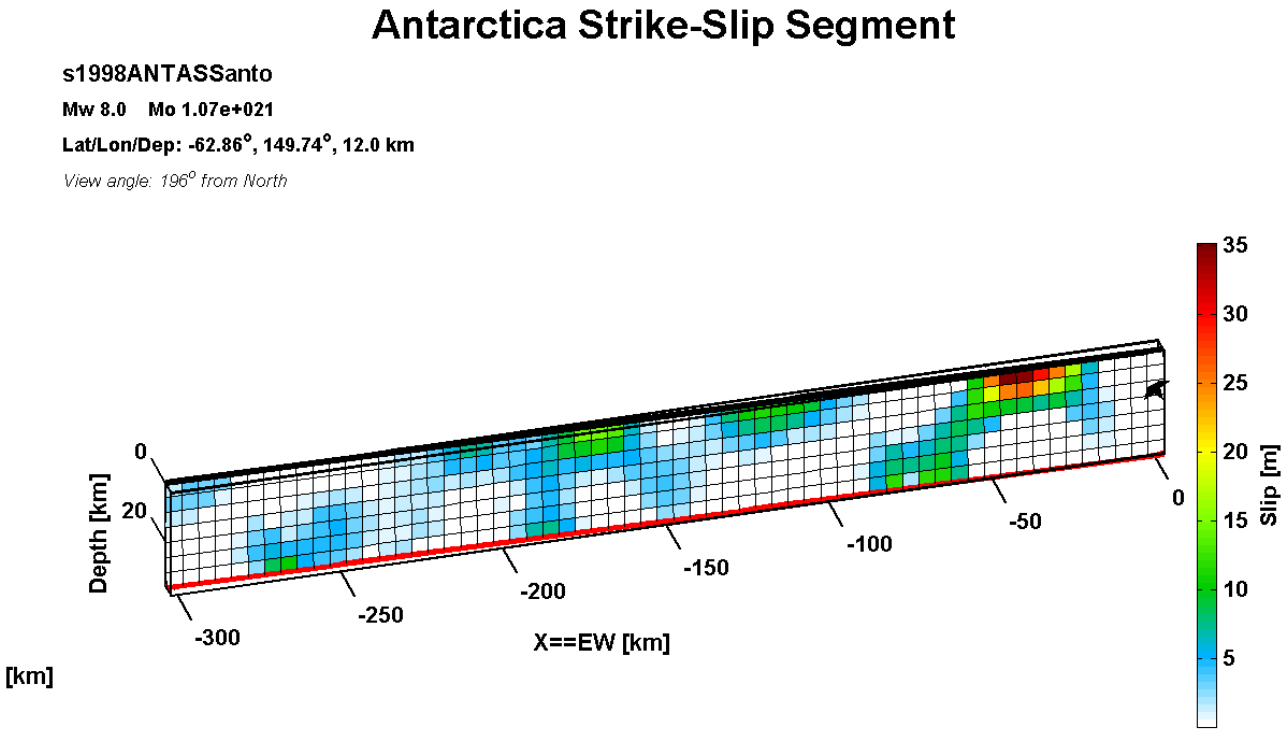

Figure 6.7: FFM representation of event 15, by Antolik at al. (2000), taken from the SRCMOD database

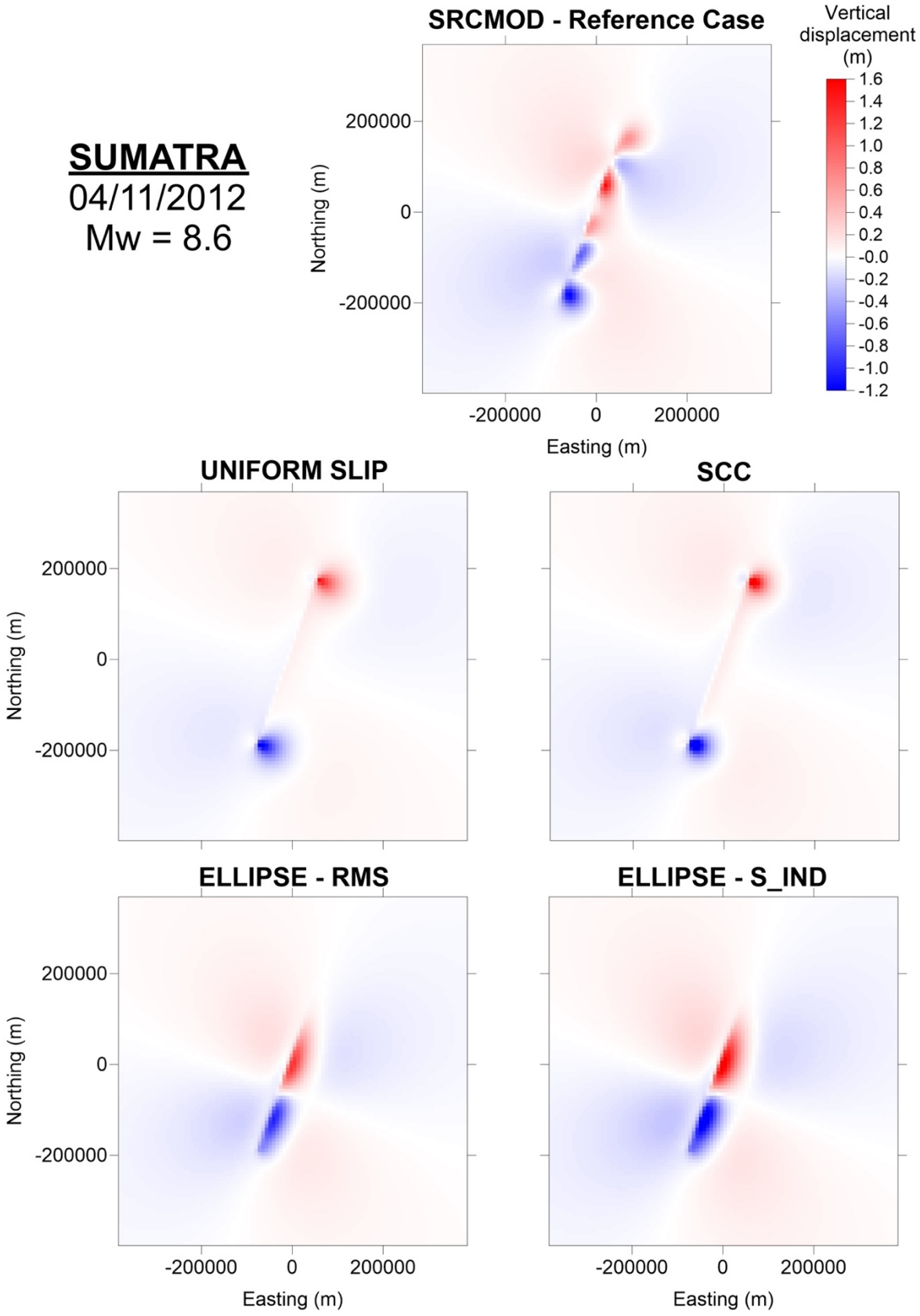

Figure 6.8: Near-source vertical-displacement fields for the event I.N. = 89

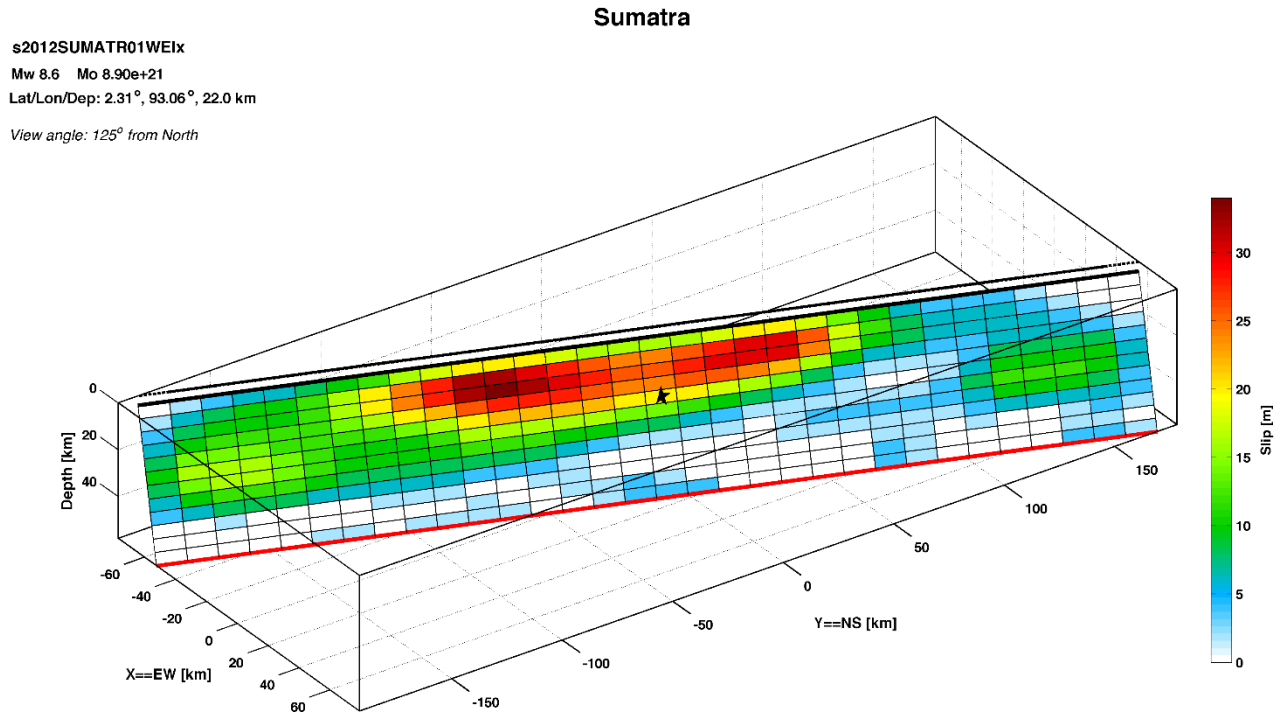

Figure 6.9: FFM representation of event 89, by Wei (Caltech, Sumatra 2012), taken from the SRCMOD database

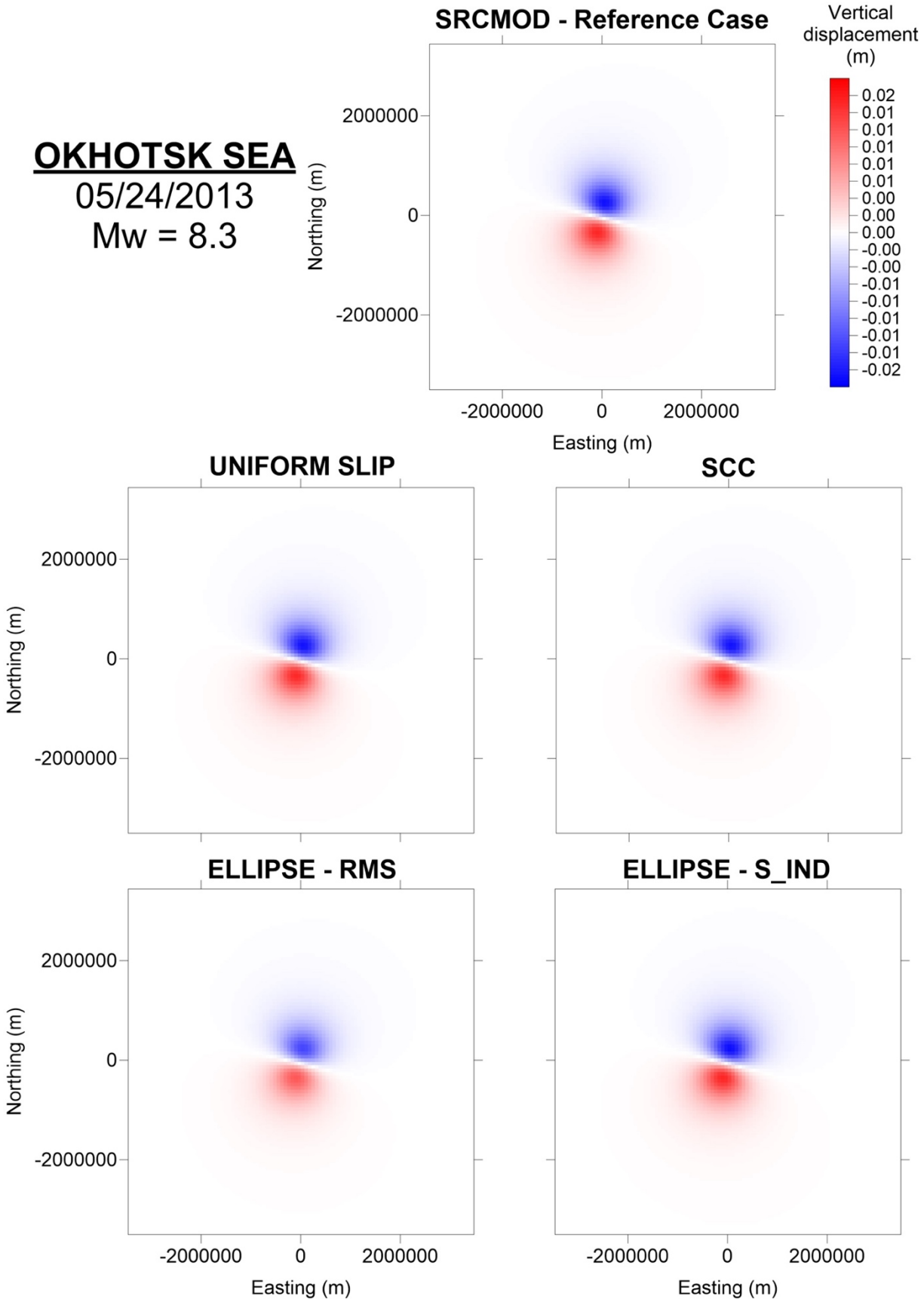

Figure 6.10: Near-source vertical-displacement fields for the event I.N. = 95

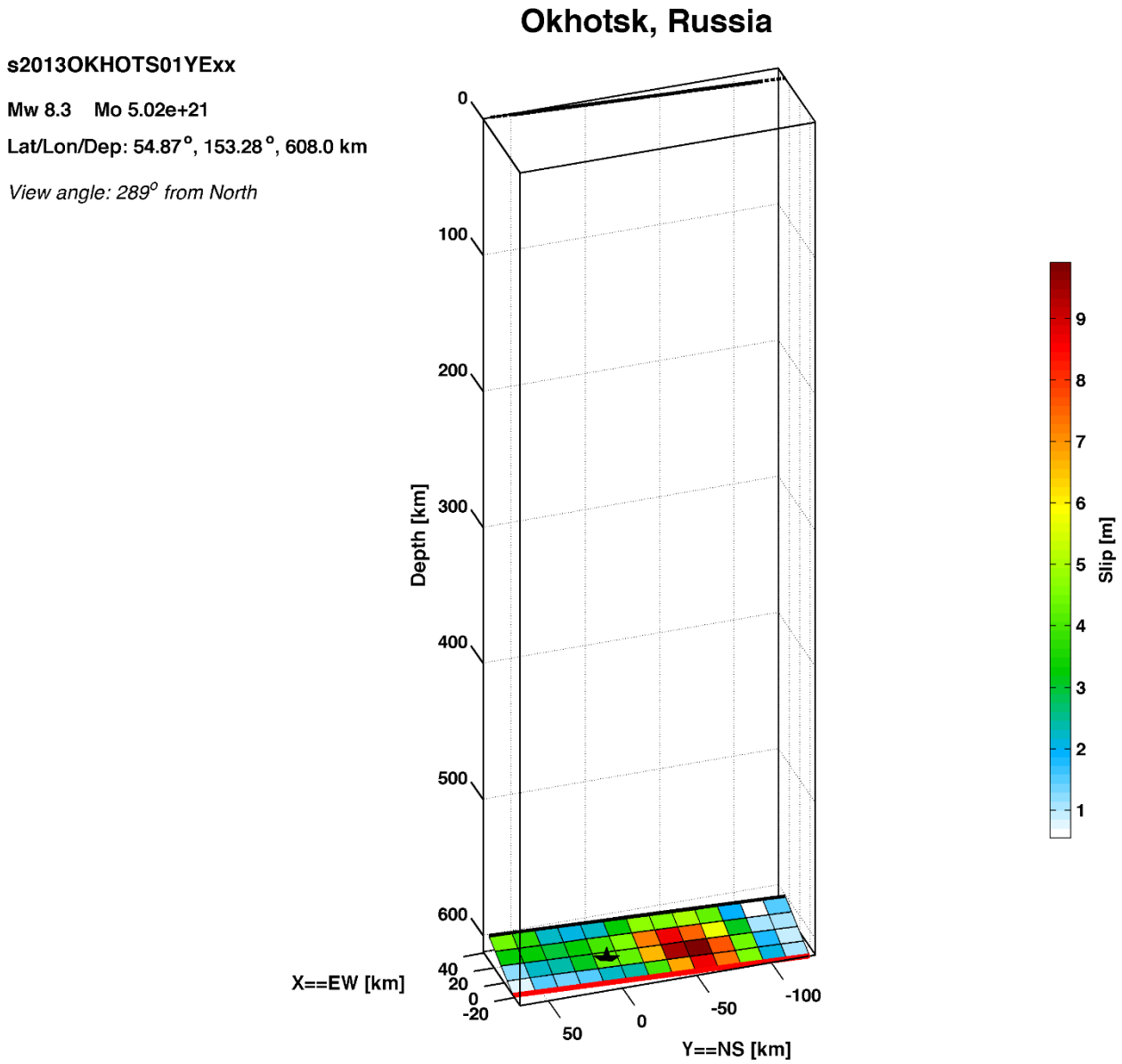

Figure 6.11: FFM representation of event 95, by Ye et al. 2013, taken from the SRCMOD database

6.2.3 Events deserve further investigations

The main problem here is related to the way we choose the surface computational domain. As we specified at the beginning of the chapter, the choice consisted in centring the domain on the faults surface projection mean point and extending for a distance two times the total fault length along the E-W and N-S directions. This revealed to be appropriate for shallow, not too gently dipping fault planes: in these cases, the main features of the co-seismic field are completely contained in the computational grid. Instead, for deep faults with shallow dip angles, the characteristic length to be taken into

account is not the total fault length, but the distance between the surface projection of the lower border of the fault and the surface trace of the fault i.e., the line along which the plane containing the fault intercepts the free surface. In the cases shown below, this distance is significantly larger than the fault length: as a result, the co-seismic field we computed is only a portion of the complete field and the comparisons we made can only have a very partial meaning. This is a problem that we will solve in the future work.

The two events that we show as examples are:

- I.N. = 69, Padang, Indonesia 09/30/2009, Depth = 80 km, Oblique, dip = 58°, *Figure 6.12*;
- I.N. = 80, Pakistan, 01/18/2011, Depth = 66.8 km, Normal, dip = 65°, *Figure 6.14*.

Event 69 presents two good Gaussian distribution (rms = 0.07, s-index = 0.918) and almost identical. However, while the misfit associated to the s-index ellipse is really low and smaller than the uniform and SCC ones, the rms ellipse misfit is significantly larger. Event 80 (rms = 0.132, s-index = 0.636) presents lower misfits (for rms and s-index ellipses) respect with the uniform misfit, but the best value is represented by the SCC misfit.

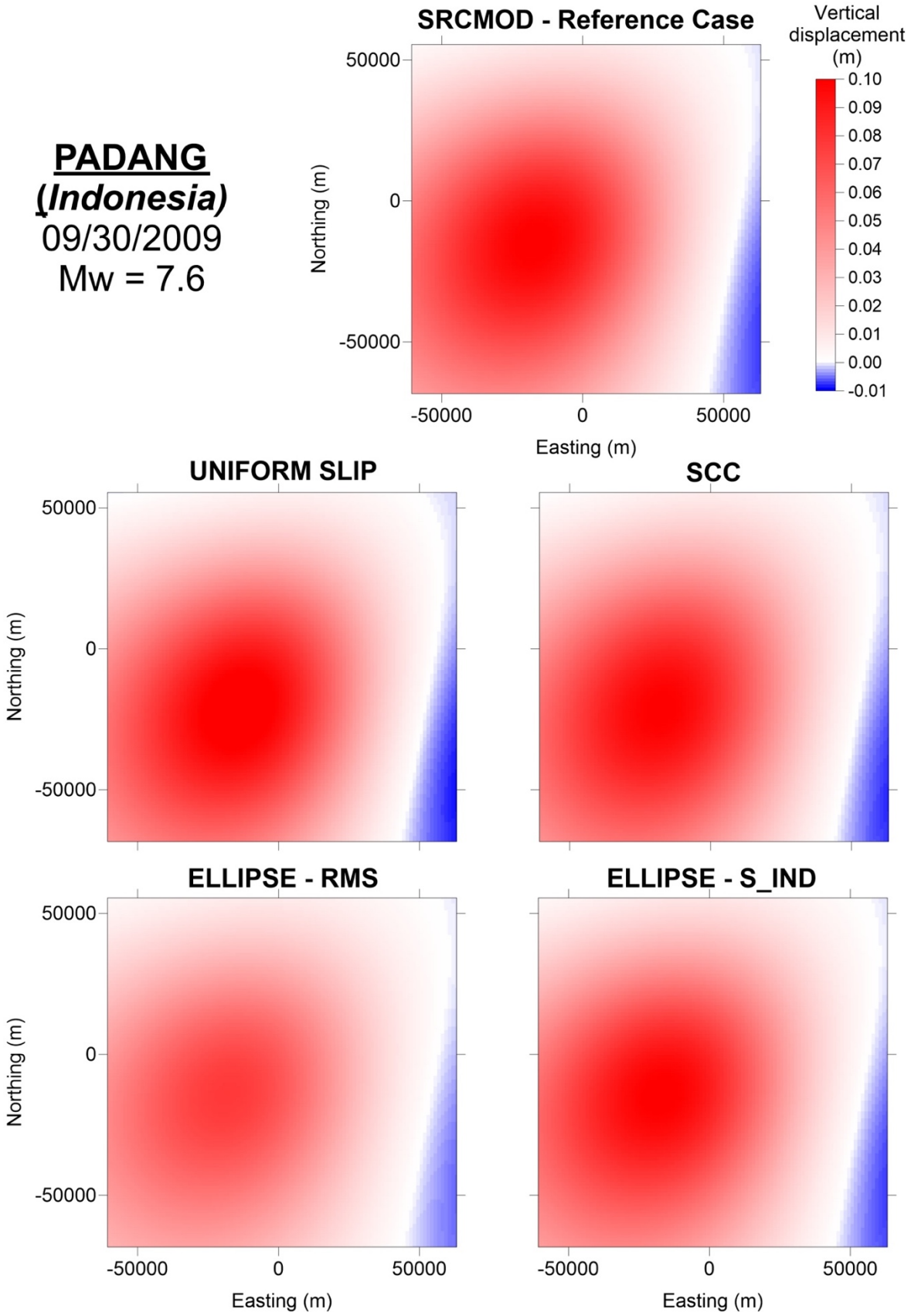

Figure 6.12: Near-source vertical-displacement fields for the event I.N. = 69

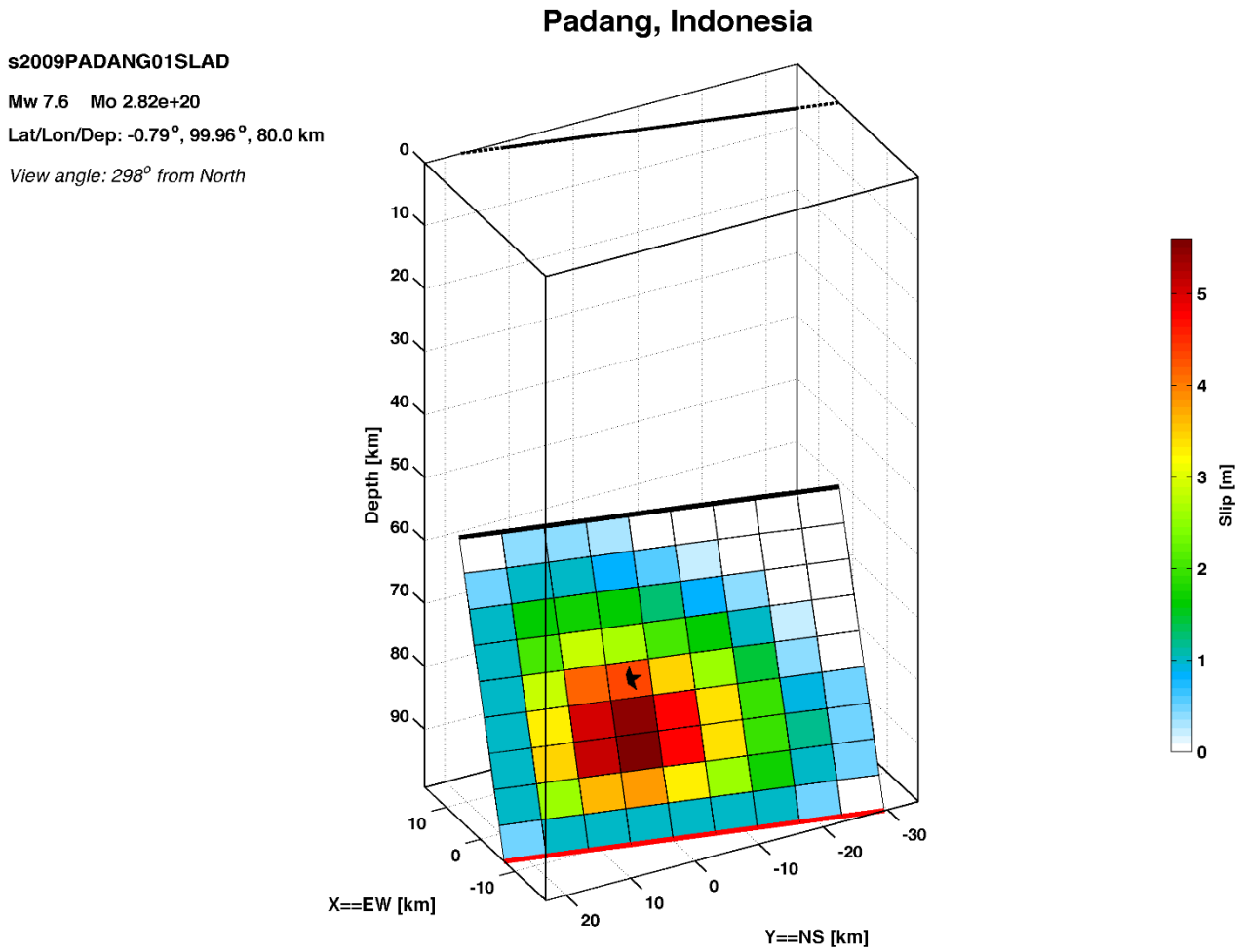

Figure 6.13: FFM representation of event 69, by Sladen (Caltech, Padang 2009), taken from the SRCMOD database

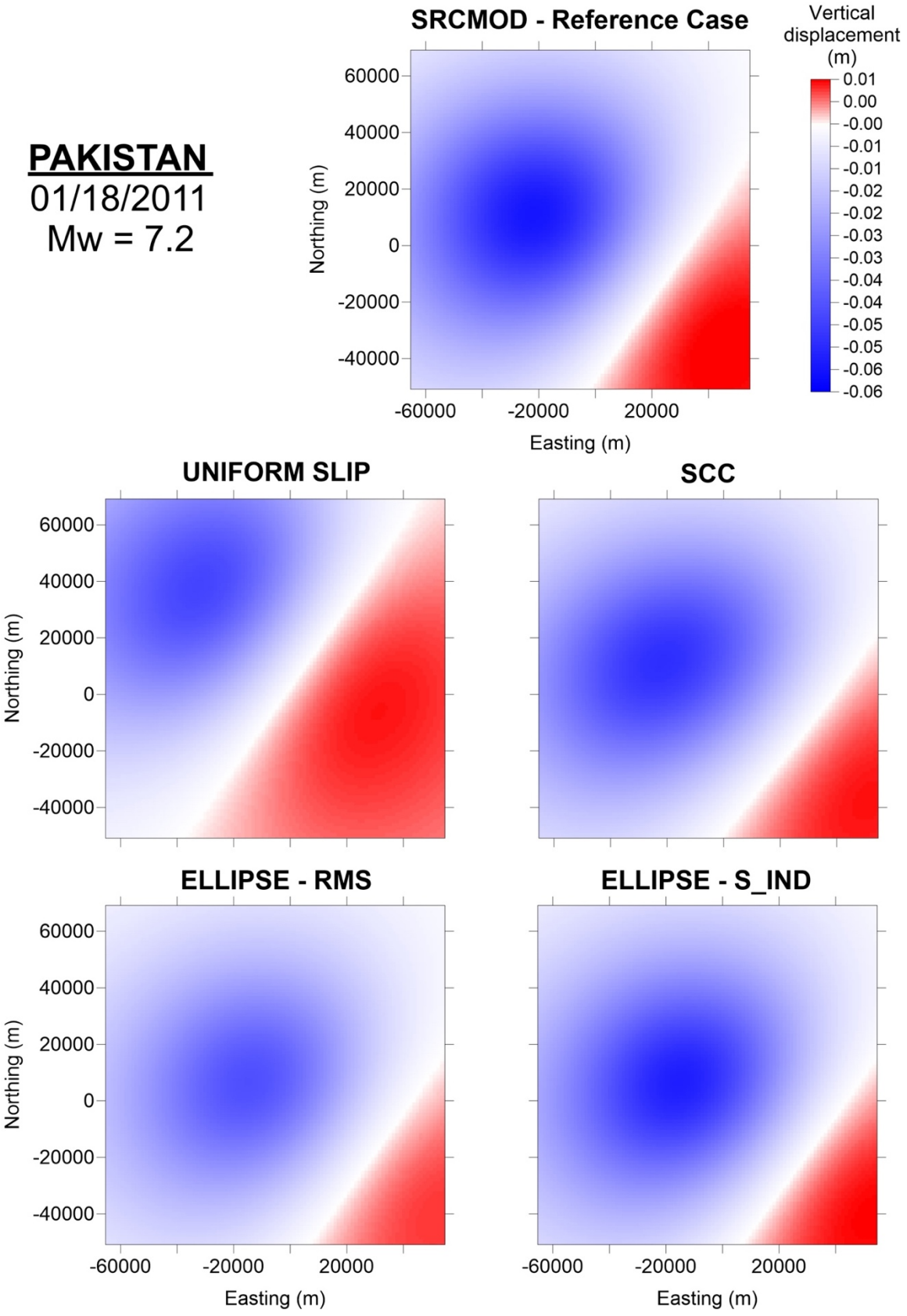

Figure 6.14: Near-source vertical-displacement fields for the event I.N. = 80

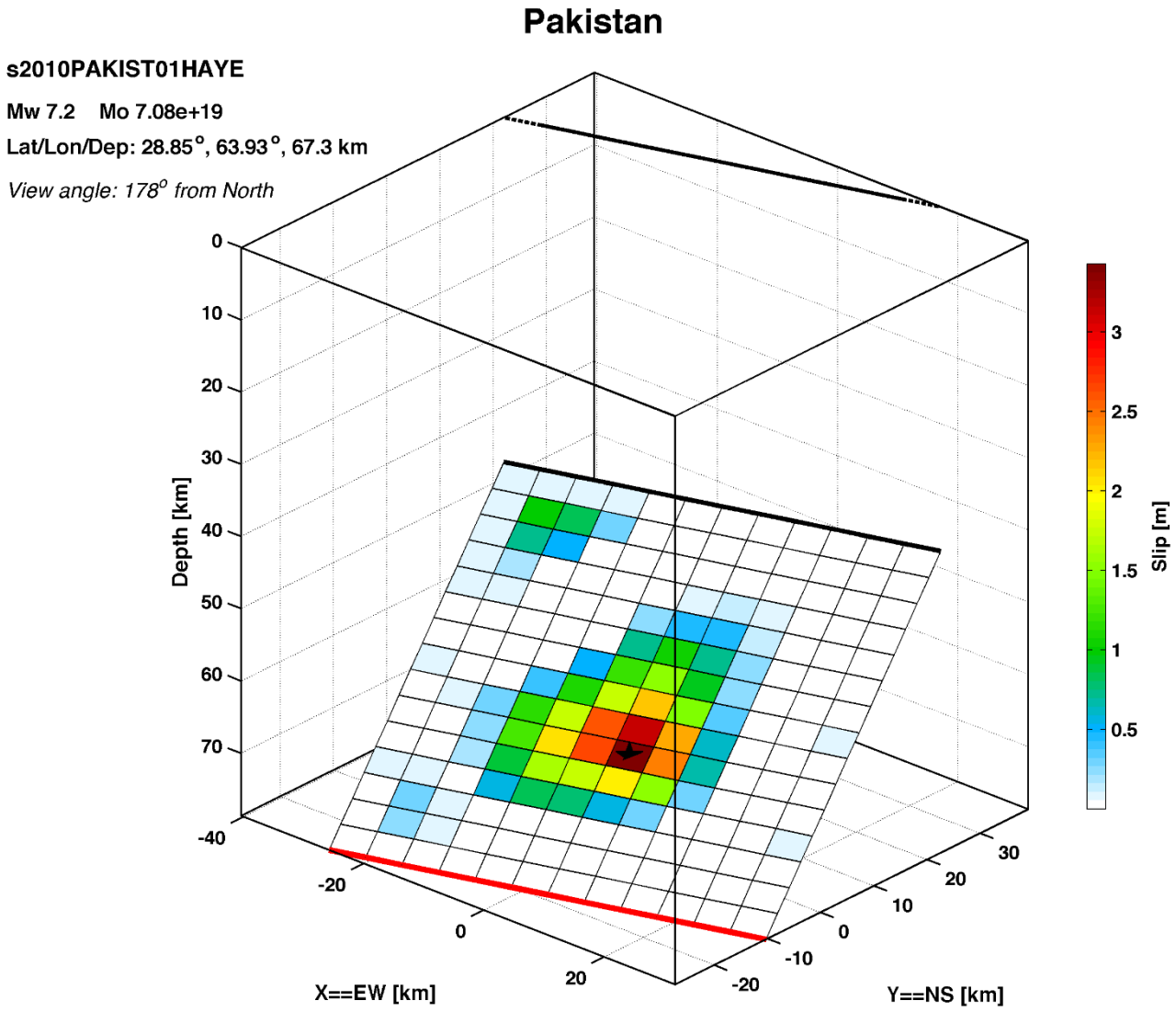

Figure 6.15: FFM representation of event 80, by Hayes (NEIC, Pakistan 2011)a, taken from the SRCMOD database

6.2.4 *Events with contrasting behaviour between the two Gaussian distributions*

- I.N. = 37, Nigata-Ken Cheutsu, Japan, 10/23/2004, Depth = 10.6 km, Reverse, dip = 47°, *Figure 6.16*.

Event 37 presents rms = 0.228 and s-index = 0.792. The s-index ellipse presents really good misfit with respect to the uniform and the SCC ones, while the rms ellipse presents a misfit larger than twice the uniform and SCC ones and more than three times the s-index one. This can be attributed to the fact that the FFM-REF models presents a large region with high slip values completely asymmetric with respect to the peak of slip, which is located close to the lower border of the fault. The high slip region shallower

than the peak position is well covered by the s-index ellipse, which tends to preserve the overall structure. This is not valid for the rms-ellipse, which largely favours the slip peak area.

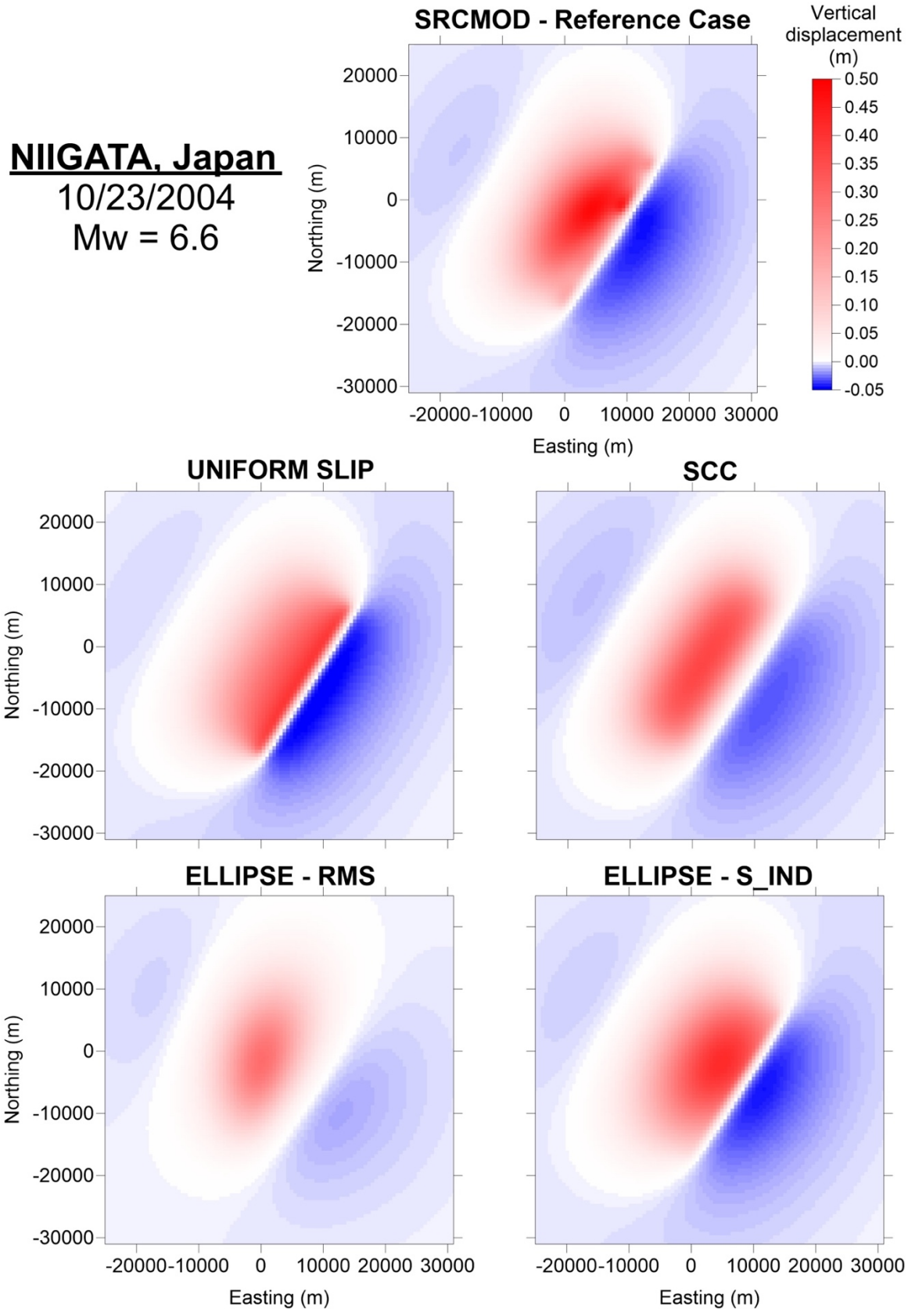

Figure 6.16: Near-source vertical-displacement fields for the event I.N. = 37

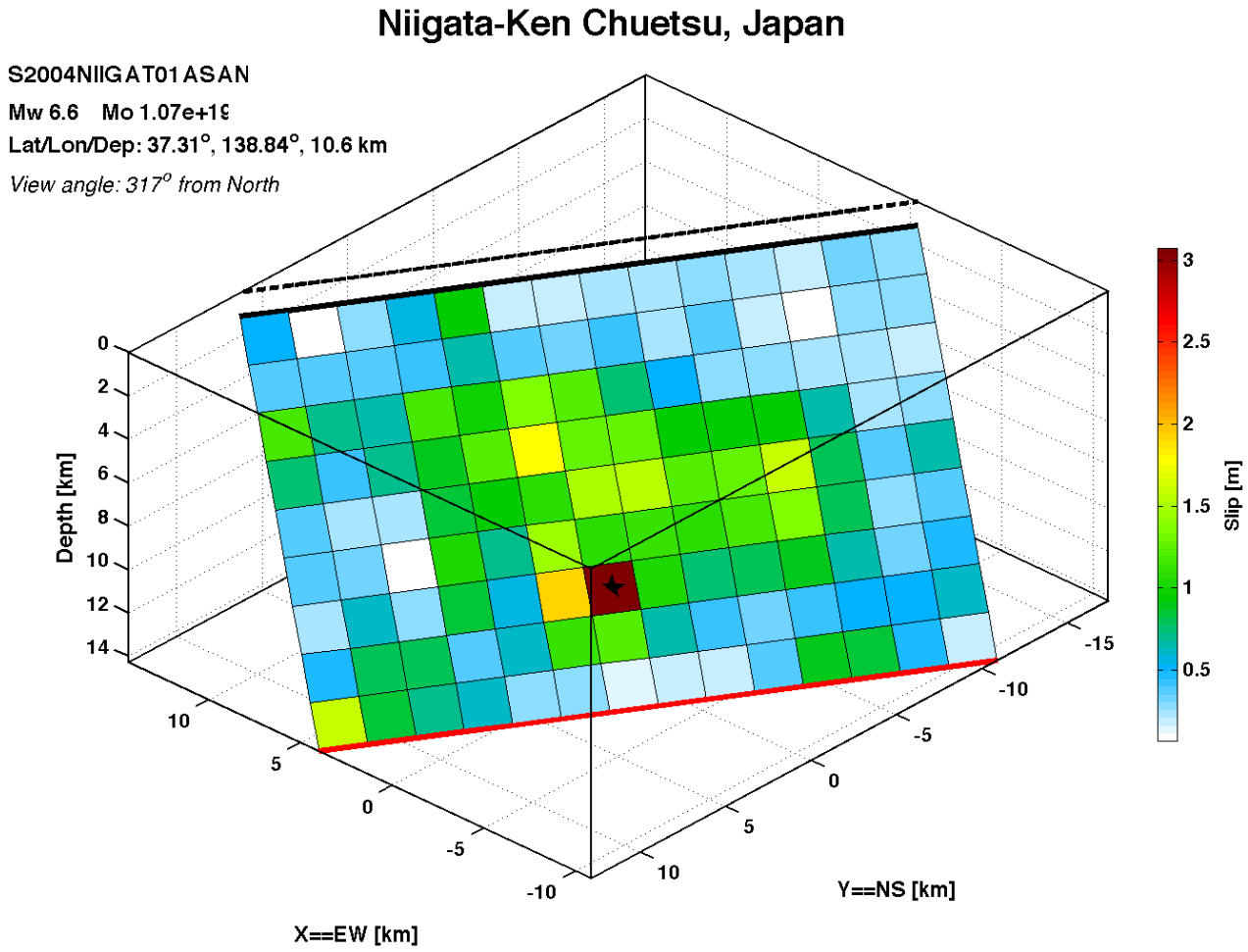

Figure 6.17: FFM representation of event 37, by Asano and Iwata 2009 taken from the SRCMOD database

7 Conclusions

This thesis dealt with the characterization of the slip distribution on the faults responsible for the largest magnitude earthquakes occurred worldwide in the last 25 years.

The dataset of events analysed in this study was extracted from the SRCMOD database (http://equake-rc.info/SRCMOD/), which is a growing repository of finite-fault models (FFMs) published in literature or provided by different authors. The selection regarded 98 events occurred after 1990 and with moment magnitude equal or larger than 6.

A first exercise consisted in the computation of regression laws between the geometrical properties of the fault and the moment magnitude. Several examples of this kind of study exist in the literature, but here the analysis is carried out only for earthquakes for which FFMs are available.

The analysis has been performed both considering the entire dataset and separately for different focal mechanisms.

The studied parameters included the rupture area, length, width and aspect ratio. To the authors knowledge the dependence of the latter on magnitude is analysed here for the first time. Moreover, regression laws for maximum and average slip are given. The best correlation with magnitude is shown by the area and the length of the fault.

The strike-slip events are those showing the best correlations, and the only category for which the aspect ratio shows a satisfactory level of correlation.

The aspect ratio has been given special attention in this thesis. It has been used to divide the earthquakes, or equivalently in this context, the FFMs contained in the dataset in three classes. The original FFMs have been rescaled to the typical dimension of each class and the rescaled FFMs (RFFMs) have been analysed to investigate the position of the hypocentre with respect to the regions of significant slip (and of the maximum) slip. Through a qualitative analysis, the RFFM representation allows to recognise that the hypocentre rarely lies close to the fault centre or to the peak of slip; more often, it is found at the margin of an asperity, that is a region of significantly high slip. Furthermore, the number of asperities tends to increase with increasing aspect ratio. The distance from the fault centre of the slip peak position tends to increase with magnitude: for smaller magnitudes, it is often close to the centre of the fault.

The standardized RFFM representations allowed us to analyse the distribution of the slip and to compare different models by means of proper similarity indexes. Since most FFMs exhibit a single and clear region of high slip (i.e. a single asperity), it sounded reasonable to best-fit the slip model by means of a 2D Gaussian distribution. Two different methods were used (least-square and highest-similarity) and correspondingly two "best-fit" indexes were introduced. As a result, two distinct 2D Gaussian distributions for each FFM were obtained.

To quantify how well these distributions are able to mimic the original slip heterogeneity, in the last chapter we have calculated and compared the vertical displacements at the Earth surface in the near field induced by the FFM slip (assumed to be the real one), by an equivalent uniform-slip model, by a depth-dependent slip model, and by the two "best" Gaussian slip models. The coseismic vertical surface displacement has been chosen as the metric for comparison since the main interest of the line of research started with this thesis is the generation of tsunamis by earthquakes. Results show that, on average, the best results are the ones obtained with 2D Gaussian distributions based on similarity index fitting. Uniform slip sources can produce discrepancies in the surface fields larger than 50% on average, which is slightly reduced with depth-dependent sources. The supremacy of the 2D Gaussian distributions is especially evident for those events whose original FFM is characterised by a single, sharp, roughly symmetric peak. The distance in misfit between the 2D Gaussian representations and the uniform and depth-dependent distributions tend to degrade for those cases in which the peak is single but the slip is not symmetric, or when more than one peak is present.

The study of this thesis sets the basis for a following research project to be carried out by the author in the frame of the UNIBO Doctorate in Geophysics. The aim will be to explore the feasibility of a real-time assessment of the co-seismic slip of large earthquakes having high tsunamigenic potential, based only on those earthquake parameters that are available almost in real time, i.e. magnitude and hypocentre location. Among these, the shallow events with potential consequences in the near field will assume more importance, because the near field is known to be more susceptible to the heterogeneous distribution of the slip. The final goal will be to produce real-time tsunami simulations in the frame of operational tsunami warning systems.

8 References

Babeyko, A. Y., Hoechner A., Sobolev, S.V., 2010. Source modeling and inversion with near real-time GPS: a GITEWS perspective for Indonesia. Nat. Hazards Earth Syst. Sci., 10, 1617-1627.

Beroza, G. C. (1991). Near-source modeling of the Loma Prieta earthquake; evidence for heterogeneous slip and implications for earthquake haz- ard, Bull. Seism. Soc. Am. 81, 1603–1621.

Blaser, L., Krüger, F., Ohrnberger, M., Scherbaum, F. (2010). Scaling Relations of Earthquake Source Parameter Estimates with Special Focus on Subduction Environment. Bull. Seism. Soc. Am., 100, 2914-2926, doi:10.1785/0120100111.

Freund, L. B. and Barnett, D. M., 1976. A two-dimensional analysis of surface deformation due to dip-slip faulting, Bull. Seismol. Soc. Am., 66, 667–675, 1976.

Geist, E. L., Complex earthquake rupture and local tsunamis, Journal of Geophysical Research, 107, doi:10.1029/2000JB000139, 2002.

Geist, E.L., Dmowska, R., 1999. Local tsunamis and distributed slip at the source. Pure Appl. Geophys., 154, 485-512.

Geist, E. L., S. L. Bilek, D. Arcas, and V. V. Titov (2006). Differences in tsunami generation between the 26 December 2004 and 28 March 2005 Sumatra earthquakes, Earth Planets Space 58, 185–193.

Geist, E., Titov, V.V., Arcas, D., Pollitz, F.F. & Bilek, S.L., 2007. Implications of the 26 December 2004 Sumatra–Andaman earthquake on tsunami forecast and assessment models for great subduction-zone earthquakes, Bull. seism. Soc. Am., 97(1A), S249–S270, doi:10.1785/0120050619.

Goda et al.: Sensitivity of tsunami wave profiles and inundation simulations to earthquake slip and fault geometry for the 2011 Tohoku earthquake. Earth, Planets and Space 2014 66:105.

Gutscher, M.-A., Roger, J., Baptista, M.-A., Miranda, J.M., Tinti S., 2006. Source of the 1693 Catania earthquake and tsunami (southern Italy): New evidence form tsunami modeling and locked suduction fault plane. Geophys. Res. Lett., 33, L08309, doi:10.1029/2005GL025442.

Iinuma, T., et al. (2012), Coseismic slip distribution of the 2011 off the Pacific Coast of Tohoku Earthquake (M9.0) refined by means of seafloor geodetic data, J. Geophys. Res., 117, B07409, doi:10.1029/2012JB009186.

Leonard, M. (2010). Earthquake Fault Scaling: Self-Consistent Relating of Rupture Length, Width, Average Displacement, and Moment Release. Bull. Seism. Soc. Am., 100, 1971-1988, doi:10.1785/0120090189.

Leonard, M. (2014). Self-Consistent Earthquake Fault-Scaling Relations: Update and Extension to Stable Continental Strike-Slip Faults. Bull. Seism. Soc. Am., 104, 2953-2965, doi:10.1785/0120140087.

Løvholt, F., G. Pedersen, S. Bazin, D. Kühn, R. E. Bredesen, and C. Harbitz (2012), Stochastic analysis of tsunami runup due to heterogeneous coseismic slip and dispersion, J. Geophys. Res., 117, C03047, doi:10.1029/2011JC007616.

Løvholt et al. (2012). Modeling propagation and inundation of the 11 March 2011 Tohoku tsunami, Natural hazards and earth system sciences 2012, 12(4):1017-1028

Mai PM, Spudich P, Boatwright J. 2005. Hypocenter locations in finite-source rupture models. Bull Seismol Soc Am. 95:965 980.

Mai, P. M., and G. C. Beroza, Source scaling properties from finite-fault rupture models, Bull. Seismol. Soc. Am., 90, 604–615, 2000.

Mai, P. M., and G. C. Beroza, A spatial random field model to characterize complexity in earthquake slip, J. Geophys. Res., 107(B11), 2308, doi:10.1029/2001JB000588, 2002.

Mai, P. M., and Thingbaijam, K. K. S. (2014). SRCMOD: An online database of finite source rupture models, Seismol. Res. Lett., 85, 6, 1348–1357, doi: 10.1785/0220140077.

Manighetti, I., M. Campillo, C. Sammis, P. M. Mai, and G. King (2005). Evidence for self-similar, triangular slip distributions on earthquakes: implications for earthquake and fault mechanics, J. Geophys. Res., doi 10.1029/2004JB003174 (in press).

Milliner, C. W. D. et al. Resolving Fine-Scale Heterogeneity of Co-seismic Slip and the Relation to Fault Structure. Sci. Rep. 6, 27201; doi: 10.1038/srep27201 (2016).

Okada, Y.: Internal deformation due to shear and tensile faults in a half-space, Bull. Seism. Soc. Am., 82, 1018–1040, 1992.

Sobolev, S. V., A. Y. Babeyko, R. Wang, A. Hoechner, R. Galas, M. Rothacher, D. V. Sein, J. Schro¨ter, J. Lauterjung, and C. Subarya (2007), Tsunami early warning using GPS-Shield arrays, J. Geophys. Res., 112, B08415, doi:10.1029/2006JB004640.

Somerville, P. G., K. Irikura, R. Graves, S. Sawada, D. J. Wald, N. Abrahm- son, Y. Iwasaki, T. Kagawa, N. Smith, A. Kowada (1999). Characterizing crustal earthquake slip models for the prediction of strong ground motion, Seism. Res. Lett. 70, 59–80.

S.T.G. Raghukanth & S. Sangeetha (2016) A stochastic model for earthquake slip distribution of large events, Geomatics, Natural Hazards and Risk, 7:2, 493-521, DOI: 10.1080/19475705.2014.941418

Strasser, F. O., Arango, M. C., Bommer, J. J. (2010). Scaling of the Source Dimensions of Interface and Intraslab Subduction-zone Earthquakes with Moment Magnitude. Seismol. Res. Lett., 81, 941-950, doi:10.1785/gssrl.81.6.941

Tinti, S., Armigliato, A., Pagnoni, G., and Zaniboni, F.: Scenarios of giant tsunamis of tectonic origin in the Mediterranean, ISET J. Earthq. Techn., 42, 171–188, 2005.

Tonini, R., Armigliato, A., PAgnoni, G.,Zanibono F., Tinti, S., 2011. Tsunami hazard for the city of Catania, eastern Sicily, Italy, assesse by means of Worst-case Credible Tsunami Scenario Analysis (WCTSA). Nat. Hazards Earth Syst. Sci., 11, 1217–1232.

Wells, D. L., and Coppersmith, K. J. (1994). New empirical relationships among magnitude, rupture length, rupture width, rupture area, and surface displacement. Bull. Seism. Soc. Am., 84, 974-1002.

Zaniboni, F. and Tinti, S. Numerical simulations of the 1963 Vajont landslide, Italy: application of 1-D Lagrangian modelling. Nat Hazards (2014) 70: 567. doi:10.1007/s11069-013-0828-2

http://equake-rc.info/SRCMOD/

http://www.geol.ucsb.edu/faculty/ji/big_earthquakes/home.html

http://www.tectonics.caltech.edu/slip_history/index.html

http://earthquake.usgs.gov/earthquakes/browse/significant.php?year=2007

9 Appendix A

Below, all the slip matrix representation are reported.

They are organized by class. Like the images used in Chapter 3 for the discussion about the hypocentre, each faults presents the number of class membership and, between parenthesis, the Identification Number (I.N.).

The images reproduce the slip matrix after the operation of scaling, re-gridding, re-normalization (between 0 and 1).

The colour scale is the same adopted in the chapters of the thesis, going from blue (0) to red (1).

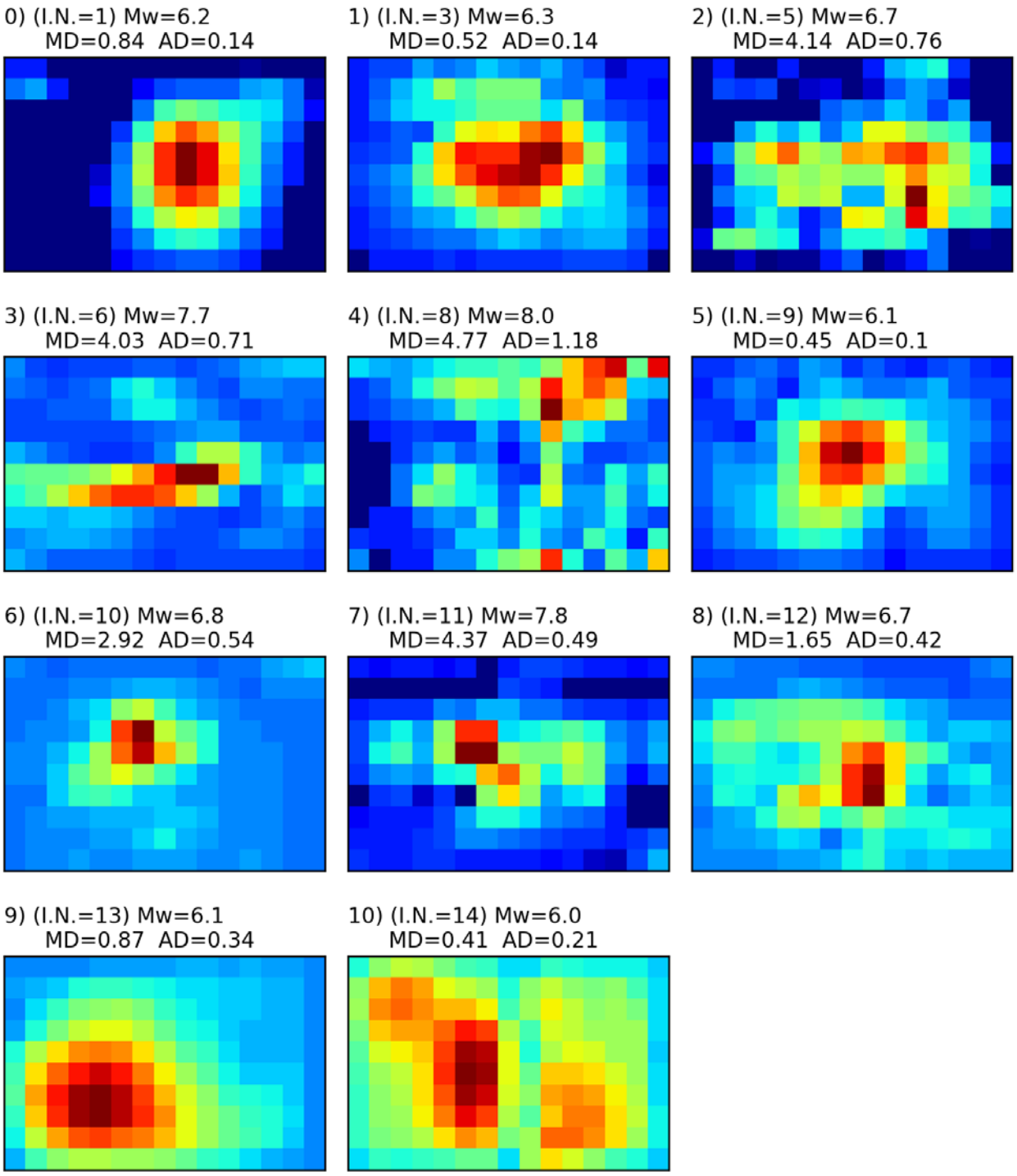

Figure 9.1: First set of images for Class 1

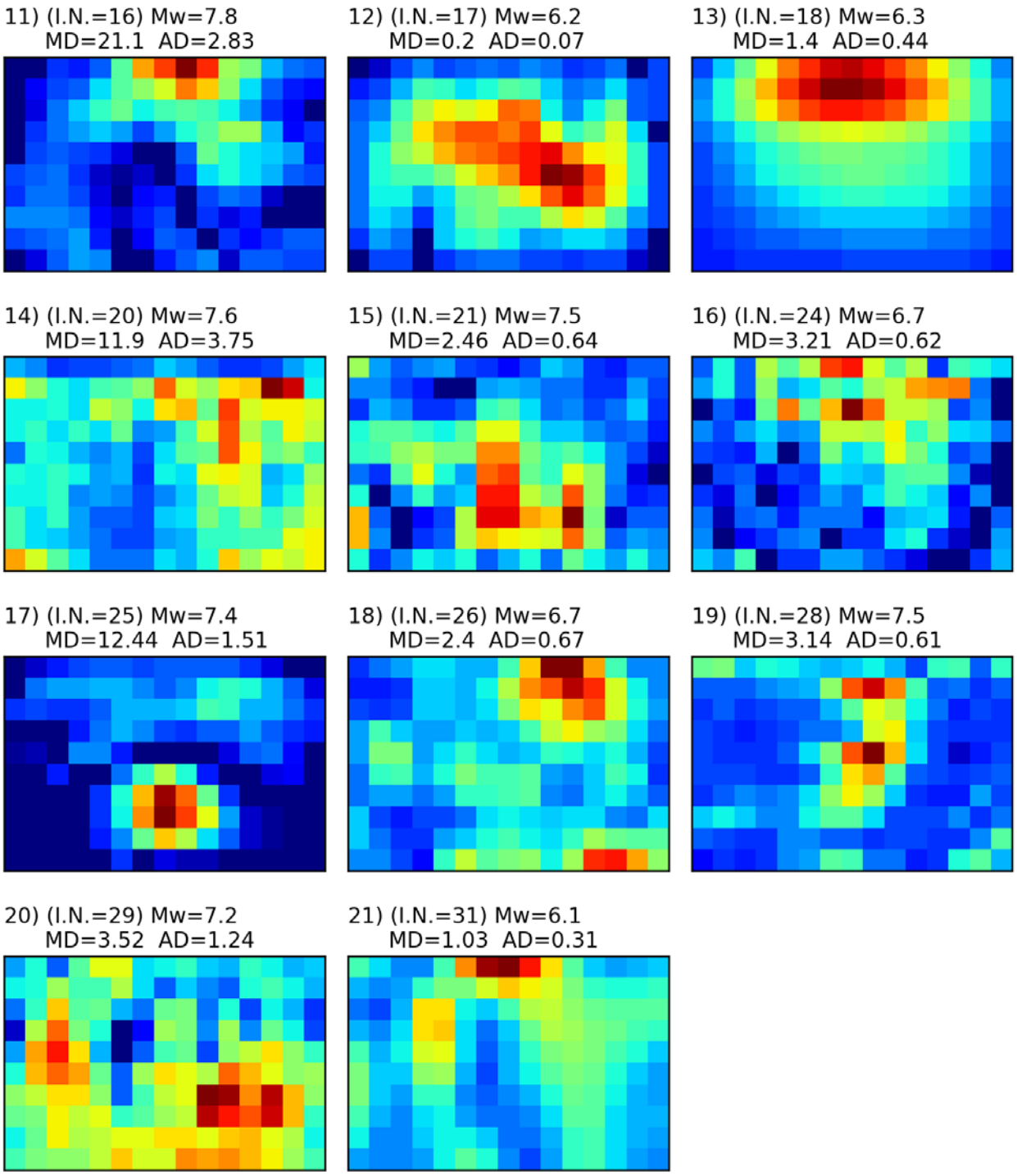

Figure 9.2: : Second set of images for Class 1

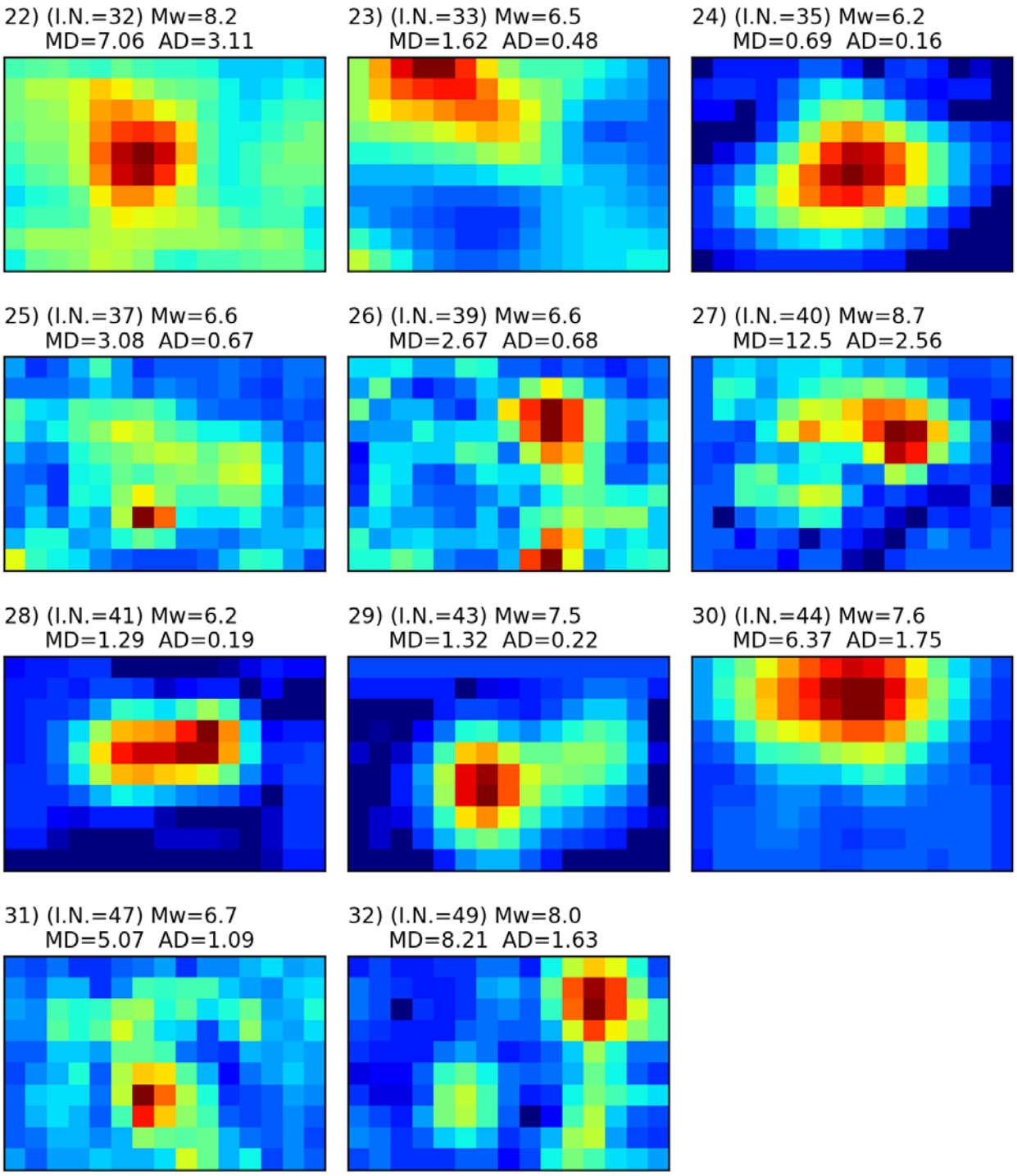

Figure 9.3: Third set of images for Class 1

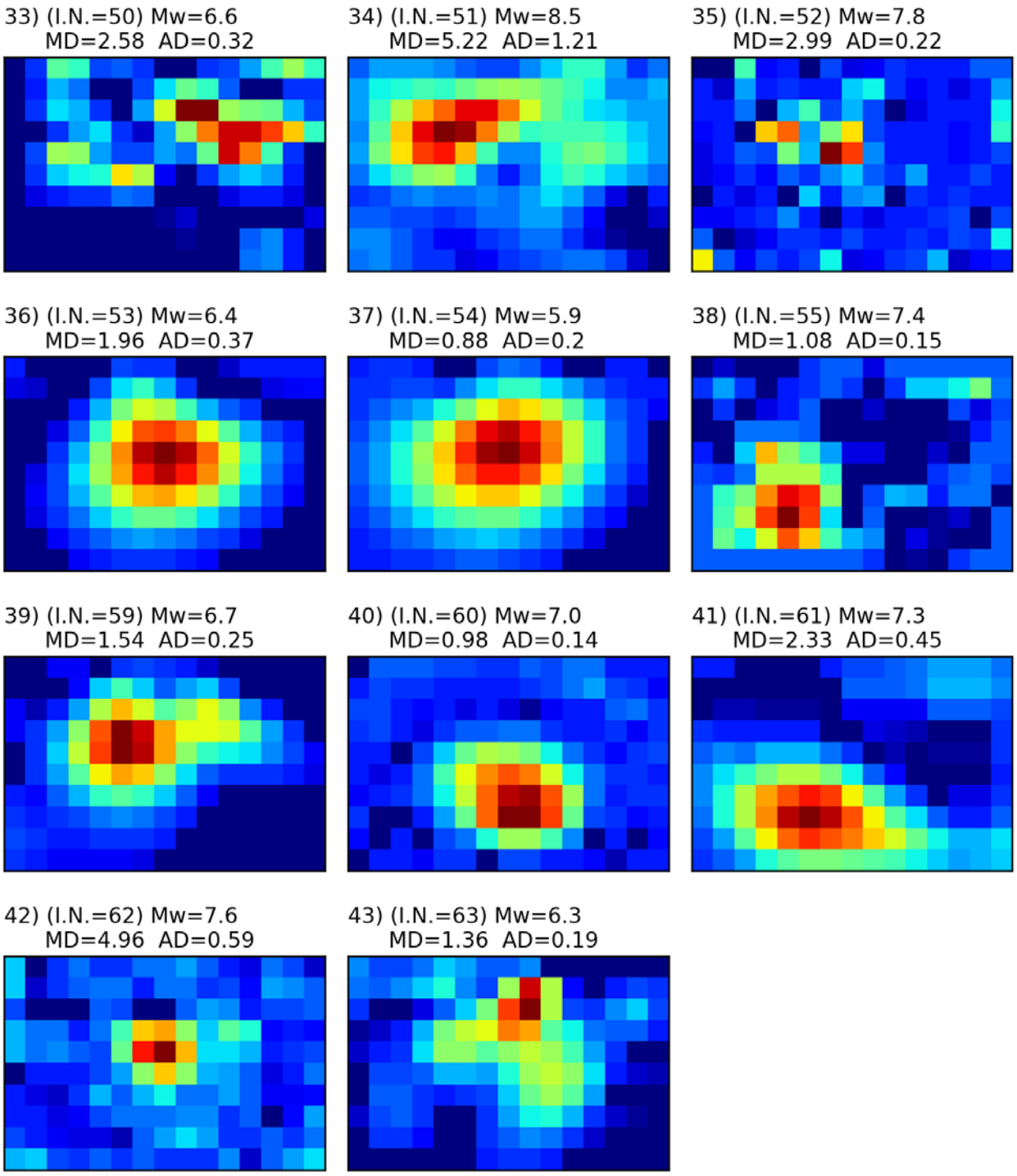

Figure 9.4: Fourth set of images for Class 1

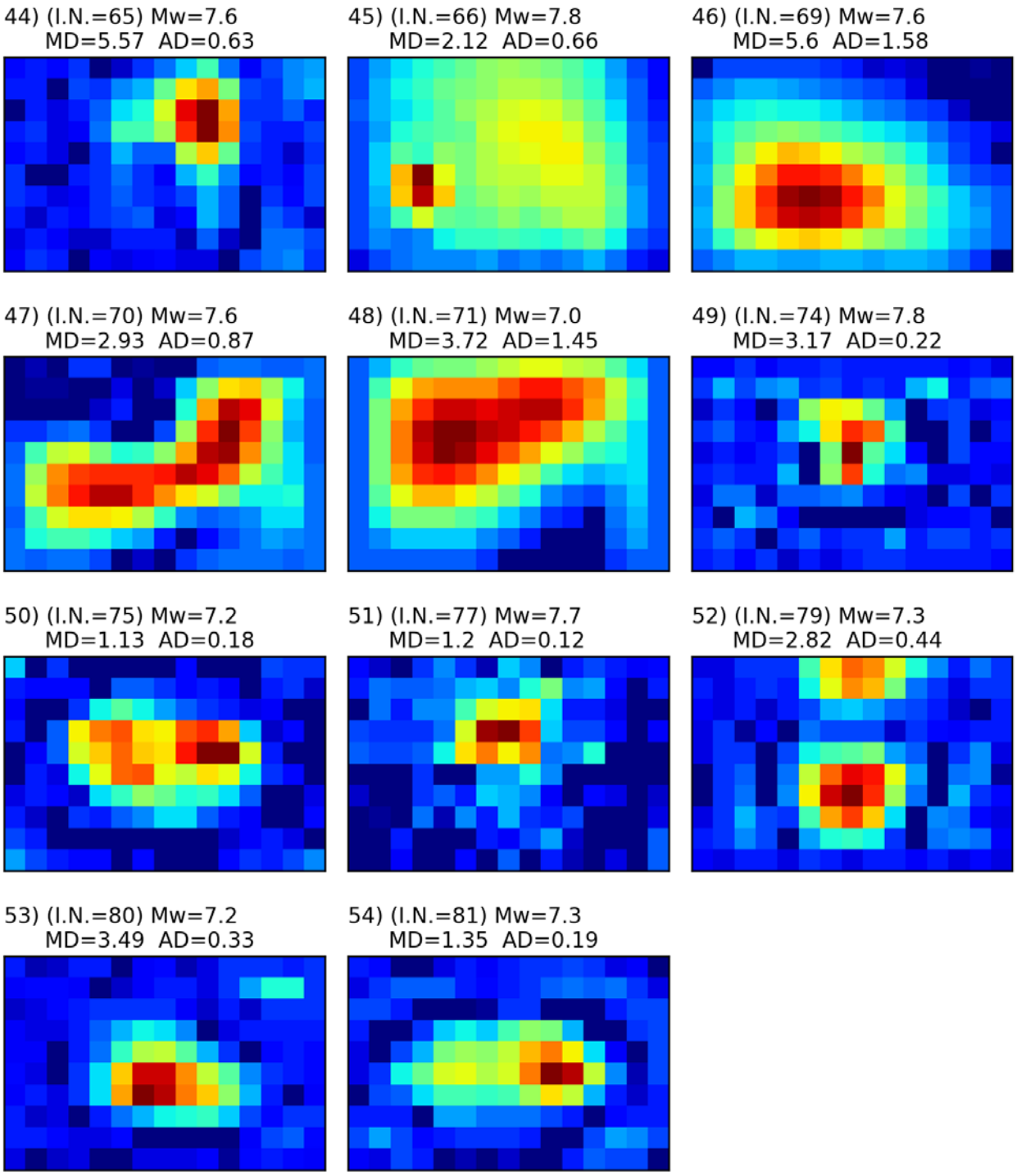

Figure 9.5: Fifth set of images for Class 1

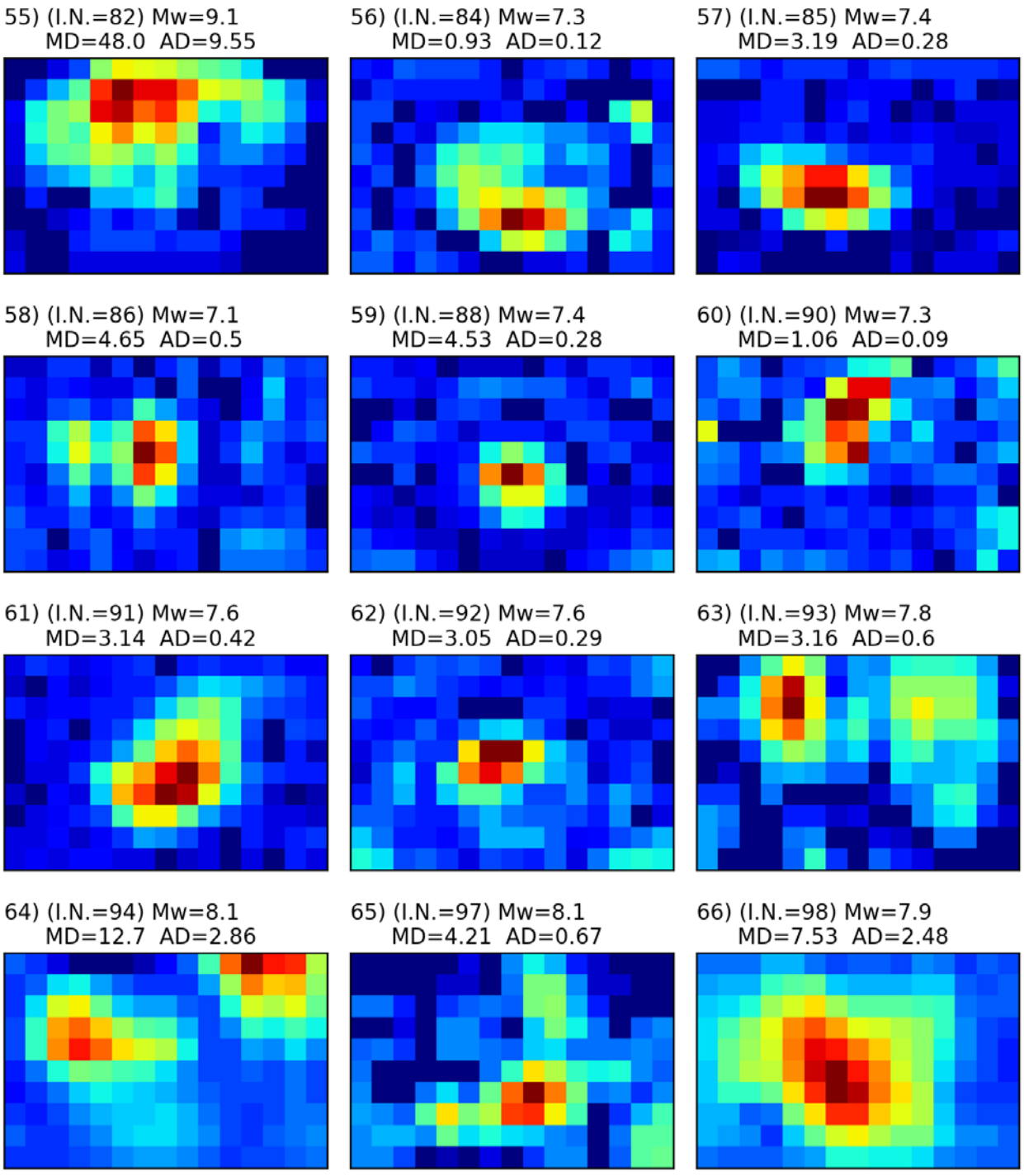

Figure 9.6: Sixth set of images for Class 1

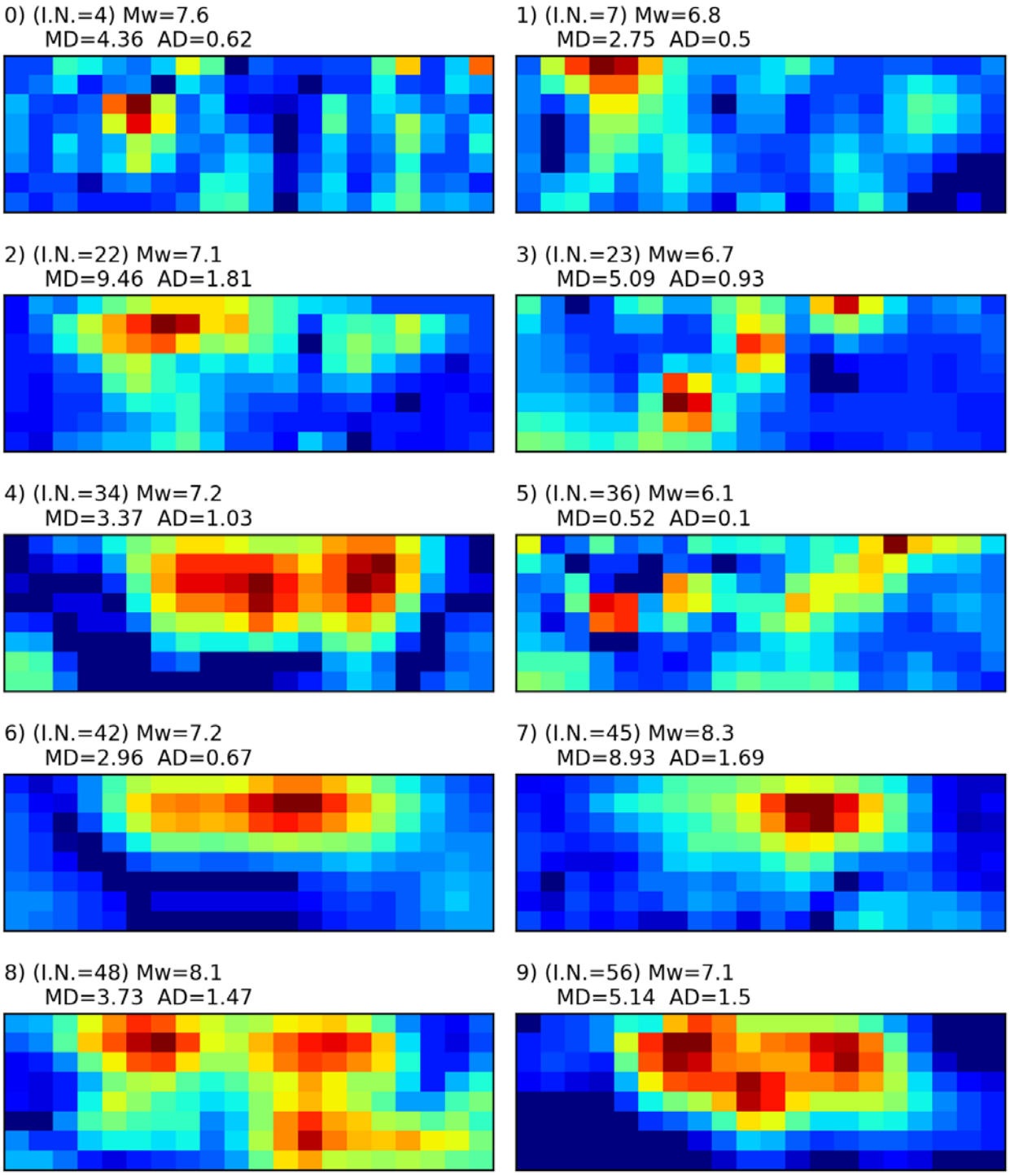

Figure 9.7: First set of images for Class 2

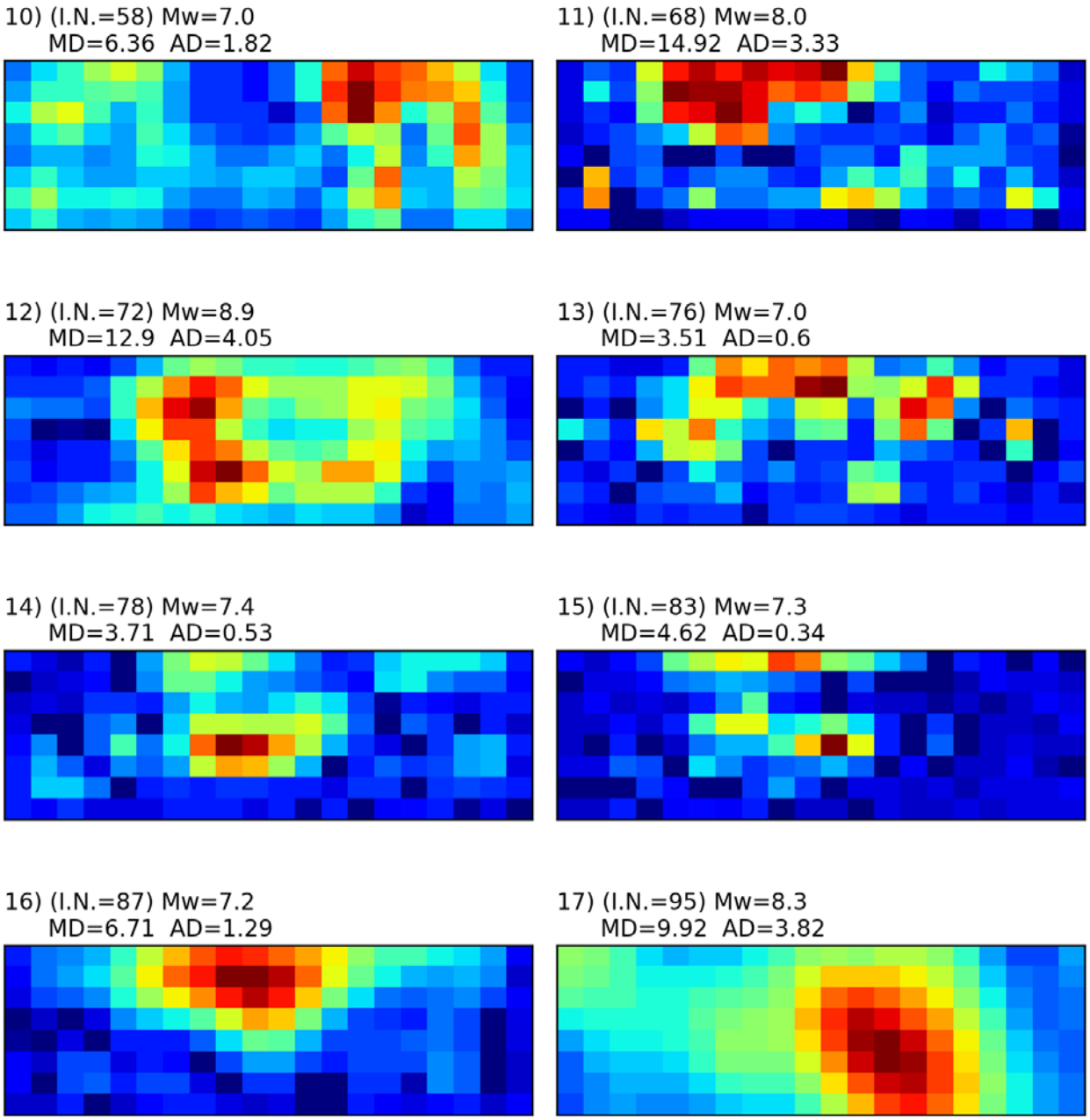

Figure 9.8: Second set of images for Class 2

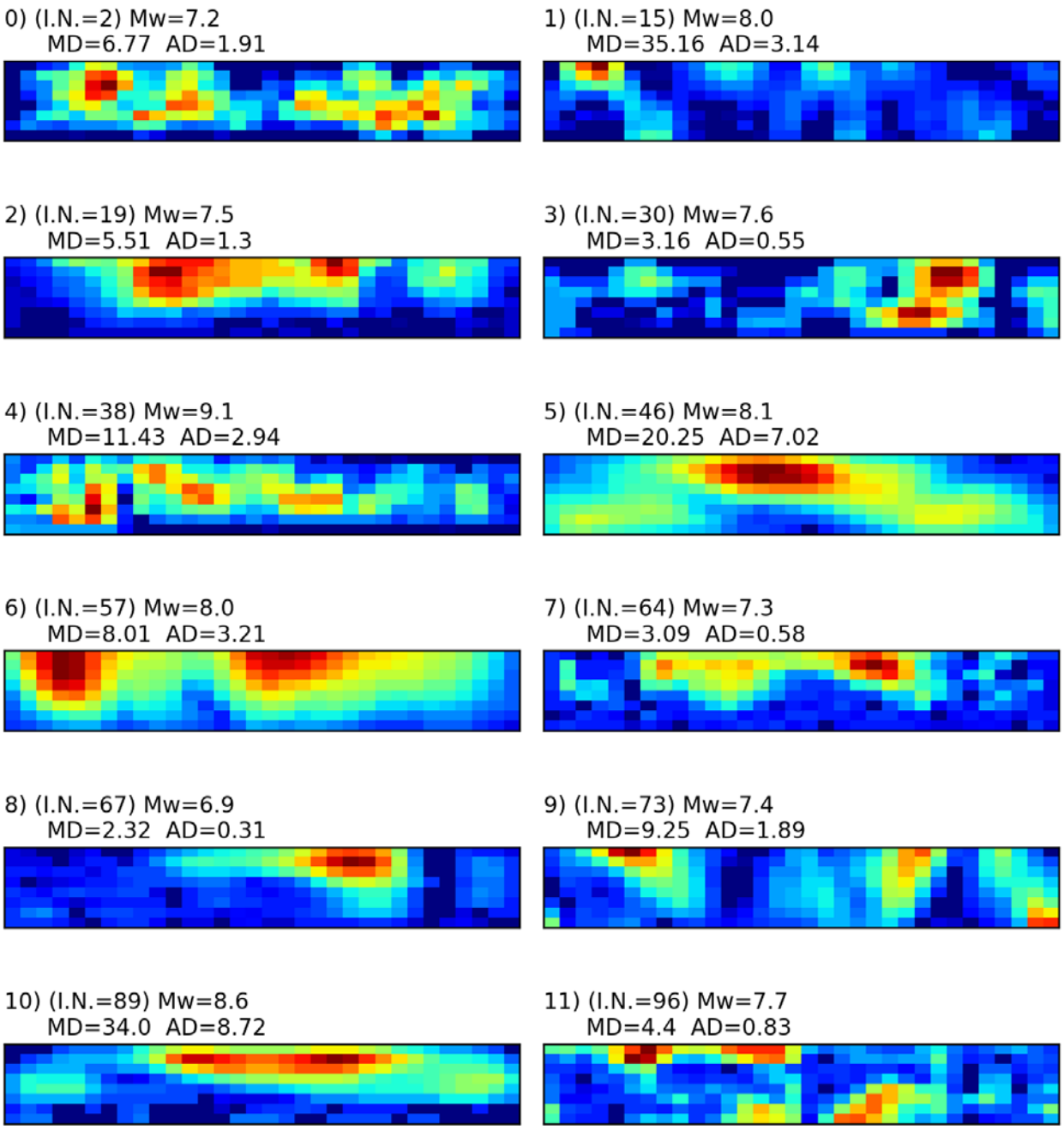

Figure 9.9: Set of images for Class 3